UNIVERSITY OF SOUTHAMPTON

FACULTY OF ENGINEERING, SCIENCE AND MATHEMATICS

School of Ocean and Earth Sciences

Application of Synchronisation Theory to Plankton Patchiness

by

Emma Guirey

Thesis for the degree of Doctor of Philosophy

August 2007

UNIVERSITY OF SOUTHAMPTON

ABSTRACT

FACULTY OF ENGINEERING, SCIENCE AND MATHEMATICS, SCHOOL OF OCEAN AND EARTH SCIENCES

Doctor of Philosophy

APPLICATION OF SYNCHRONISATION THEORY TO PLANKTON PATCHINESS

by Emma Jane Guirey

This study applies a metapopulation dynamics approach to modelling a distribution of plankton by representing a region of ocean as an ensemble of plankton populations interacting through the stirring and mixing effects of the flow. The methods of synchronisation theory are applied within this framework to gain insight into emergent spatial structure in biophysical simulations.

The manifestation of synchronisation, including statistically stable local clustering of populations, frequency-locking or phase-locking of the entire ensemble and fully synchronised dynamics, is found to depend upon: the biological model used; the strength of mixing between populations; the number of populations or, equivalently, spatial resolution of the modelled region; the level of mismatch between and spatial arrangement of population natural frequencies; the strength of stirring of the ensemble at spatial scales larger than the grid-cell. The study therefore highlights a number of biophysical modelling parameters determining the properties of emergent spatial structure in simulations of surface ocean biological dynamics.

This study shows that persistent spatial heterogeneity (patchiness) can result from what intuitively should be a homogenising influence: mixing can increase the level of disorder between the plankton populations. Furthermore, the work shows that synchronisation effects occur generically under a range of simulation scenarios, giving confidence that synchronisation theory can explain some of the spatial structure, or 'patchiness', observed in plankton distributions, and providing one possible answer as to how populations of planktonic organisms maintain coherent spatial structures under the mixing and stirring action of the oceanic flow.

Contents

List of Tables

List of Figures

Acknowledgements

I am grateful for an Environmental Mathematics and Statistics (EMS) programme studentship jointly funded by NERC and EPSRC.

In addition, I am grateful to the following people, without whom I can confidently say this thesis would never have been cajoled into being.

- Thanks to my supervisors Adrian Martin, Meric Srokosz and Martin Bees for their encouragement, optimism, guidance and seemingly endless patience. I really appreciate your help with everything over the last few years and have enjoyed working with you. Adrian, the ease with which you are distracted by mention of any kind of wildlife has been especially helpful during less productive weeks. Meric, thanks for the regular does of caffeine and counselling.

- Thanks to programming genuises Luke West, Jeff Blundall and Steven Alderson for sharing their computing expertise with me. Without you, the code would still be running, and either I or the processor would have given up and gone home by now.

- Thanks to the following lovely people for their continuing support and friendship, occasional provision of food, wine and sofa space, and for generally putting up with me: Doug McNeall, Rachel Hadfield, Squirrel Maxey, Lizzie Jolley, Zoe Roberts, Pete Martin, Ian Bailey, Chris Rowan, Donna Shillington, John Allen, Claire Holeton, Lisa Weber (for your information, it finally sounds like "kerr-THUD"), Ralf Schiebel and Andrew Erskine.

- Love and thanks to my family Alison Guirey, Chas Guirey, Ben Guirey and Betty Dolan, and also to my Grandad, Peter Dolan, who died last year, for

having faith in me and providing all the kinds of support I could possibly ask for.

- Thanks to Stewart Cross and the rest of the genuinely welcoming Platform Tavern inhabitants for gently hindering my progress over the last few years.
- Thanks to Simon Greenstreet, Helen Drewery and the Bear Pit occupants at FRS for being patient with my attempts over the last few months at living a dual work/PhD personality.
- Finally, thanks to Phil Wallhead for everything.

DECLARATION OF AUTHORSHIP

I, Emma Jane Guirey, declare that the thesis entitled Application of Synchronisation Theory to Plankton Patchiness and the work presented in the thesis are both my own, and have been generated by me as the result of my own original research. I confirm that:

- this work was done wholly or mainly while in candidature for a research degree at this University;
- where any part of this thesis have been previously submitted for a degree of any other qualification at this University or any other institution, this has been clearly stated;
- where I have consulted the published work of others, this is always clearly attributed;
- where I have quoted from the work of others, the souce is always given. With the exception of such quotations, this thesis is entirely my own work;
- I have acknowledged all main sources of help;
- where the thesis is based on work done by myself jointly with others, I have made clear exactly what was done by others and what I have contributed myself;
- parts of this work have been published as:

  E. J. Guirey, M. A. Bees, A. P. Martin, M. A. Srokosz and M. J. R. Fasham. Emergent features due to grid-cell biology: synchronisation in biophysical models. *Bulletin of Mathematical Biology*, 69(4):1401-1422, 2007

Signed:

Date:

Chapter 1

Introduction

1.1 Overview

This study applies the methods and results of synchronisation theory (Pikovsky et al., 2001) to the long-standing oceanographic puzzle of plankton patchiness (Bainbridge, 1956; Steele, 1978). We aim to use synchronisation theory to explore the spatiotemporal patterns observed both in real-world plankton distributions and biophysical simulations by viewing a distribution of plankton as an interacting ensemble of individual plankton sub-populations. A similar approach has been successfully employed by terrestrial ecologists in the study of the ubiquitous phenomenon of synchronised population dynamics in a variety of species (e.g. Moran, 1953; Ranta et al., 1995) and has been shown by Hillary and Bees (2004a) to be applicable to the study of oceanic plankton, raising a number of questions about how synchronous effects arise in spatially-extended ecosystem models (as discussed in Section 1.2.6). This study aims to address some of these questions, yielding results about spatial synchrony in marine biophysical models and what synchronisation theory can tell us about the way in which plankton are distributed in the ocean.

This brief overview will be expanded in Section 1.2 before giving the specific aims of the study and an outline of the thesis in Section 1.3.

1.2 Background

Plankton are free-floating aquatic microscopic plants and animals that largely drift with any current (Lalli and Parsons, 1997). They are heterogeneously, or patchily, distributed in the ocean over a wide range of scales. This section aims to show how synchronisation theory, which is concerned with systems of interacting oscillators, is directly applicable to the investigation of plankton patchiness. Sections 1.2.1 and 1.2.2 will describe the patchiness phenomenon, its significance, and some of the factors involved in its initiation and maintainence. The typical approach to biophysical modelling of a plankton distribution will be described in Section 1.2.3. It will be shown that a distribution of plankton may be represented as an ensemble of interacting plankton populations, each represented by an independent plankton ecosystem model, making the methods of synchronisation theory directly relevant. Synchronisation theory and its use in population dynamics in general and plankton dynamics in particular will be discussed in Sections 1.2.4 to 1.2.6.

1.2.1 Plankton patchiness

That the distribution of plankton in the ocean is spatially and temporally heterogeneous on scales of centimetres to several hundred kilometres is a well known phenomenon. It has been observed visually for many years from ships (see Bainbridge (1956) for collated examples from as far back as 1773) as discoloured patches of water and also by microscope in collected biological samples (e.g. Popova et al., 2002). More recently, patchiness in oceanic phytoplankton has been strikingly observed by satellite, even being reported by national newspapers (Connor, 2004).

Patchiness and its consequences are not fully described or understood (Martin, 2003). The main debates include: What generates and maintains patchiness? What are the respective roles of physical and biological drivers of patchiness (e.g. Srokosz et al., 2003; Folt and Burns, 1999)? What sets the observed spatial scales and structure (e.g. Skellam, 1951; Petrovskii, 1999; McLeod et al., 2002)? How is patchiness best described and characterised (e.g. Platt and Denman, 1975; Lovejoy et al., 2001)?

Whilst it is very unlikely that patchiness is caused and maintained by solely biological factors or solely physical ones, and that in reality the situation is probably far more complicated than that with multiple drivers being the norm (Folt and Burns, 1999), it is still useful to try to examine the processes separately and also to examine the extent to which physical structure determines the spatial structure of biological variables. Indeed, studies (Srokosz et al., 2003; Martin, 2000; Popova et al., 2002) suggest that the effects of the physical flow and the biological dynamics can in some cases be separable, with the flow setting the size and shape of patches, and the biology governing the amplitude of biomass within the patches. Other studies show the biology and physical flow to act together to determine patch sizes (e.g. McLeod et al., 2002). It may be difficult to distinguish between direct physical effects on patchiness (e.g. stirring), indirect physical mechanisms which trigger biological effects on patchiness (e.g. upwelling of nutrients), and direct biological effects (e.g. swarming of zooplankton), especially when more than one factor acts at once.

Patchiness occurs on a wide range of scales, and the influence of biological over physical factors varies with the scale of patchiness in question. For example, at scales of 10-100 km patchiness may result from the upwelling and trapping effects of eddies and currents, whilst at scales of 100m to 1 km patchiness may be the result of aggregation for mating by zooplankton (Folt and Burns, 1999). If physical and biological processes are acting at the same scale, such as in the case of mesoscale physical processes and some zooplankton behaviour, then the effects of the two may be difficult to differentiate (Fielding et al., 2001).

1.2.1.1 Biological drivers of patchiness

The patchiness structure is strongly influenced by the physical flow. If plankton were distributed uniformly in the ocean, however, no amount of horizontal movement by the physical flow could create patchiness from this homogeneity. The heterogeneity must be generated by some inbalance in the conditions required for phytoplankton growth and survival. Anything that generates patchiness in the availability of nutrients, other essential vitamins or light has the potential to generate plankton

patchiness, as has patchiness in the distribution of those organisms that graze upon phytoplankton (Barnes and Hughes, 1982).

Phytoplankton patchiness, once established, can be self-sustaining (Smith et al., 1996; Young et al., 2001). For example, division products of a single plankter tend to stay together in the water, so that initial heterogeneities are amplified (Barnes and Hughes, 1982; Young et al., 2001). Nutrient recycling may be another positive feedback; once clusters of organisms form, material is exuded into the water and made available for uptake by other organisms, perhaps of another species. Vertical self-sustained patchiness may be caused by shading of lower layers by dense aggregates of organisms at the surface, preventing sufficient light for growth from reaching phytoplankton at depth (Huppert et al., 2004).

Zooplankton behaviour is more complicated because they are capable of greater movement independently of the flow. Zooplankton prey upon phytoplankton; wherever there is aggregation of the prey, we would expect aggregation of the foraging predator, since some zooplankton are capable of remote food location. Hence phytoplankton patchiness may generate zooplankton patchiness. Conversely, patchy zooplankton grazing upon areas of high phytoplankton biomass may cause patchiness in the latter (Folt and Burns, 1999), i.e. top-down rather than bottom-up control. Equally, higher predators that depend upon zooplankton for food are patchily distributed in the ocean so that zooplankton distribution may become patchy through grazing or predator avoidance. Some higher predators may even force schooling of zooplankton. Examples of this, given by Barnes and Hughes (1982), are forced schooling of euphasiids by some sharks in temperate zones, and encircling of prey in a net of bubbles by whales.

Regions of high or low phytoplankton biomass may be positively or negatively correlated with regions of high or low zooplankton biomass as a result of predator-prey interactions (e.g. Steele and Henderson, 1992; Srokosz et al., 2003; Popova et al., 2002) and the behaviour and physiology of the different organisms (e.g. different buoyancy properties of phytoplankton and zooplankton; Reigada et al., 1998).

Aside from food location, zooplankton may aggregate for other reasons. Zooplankton are usually sparse in open ocean waters, with a few patches a thousand

times more dense than the median; consequently, aggregation into patchiness to mate is a survival mechanism (Folt and Burns, 1999). This swarming behaviour, the mechanisms of which are not understood, is an example of biologically driven and maintained patchiness. After reproduction, the progeny may remain together in the water for some time before dispersal, since they will be less motile than the adult organisms and so have different response times, prolonging the patchiness (Lalli and Parsons, 1997).

Many zooplankton undertake coordinated diurnal vertical migration (DVM): they vary their vertical position in the water column by as much as 1000 m during the diurnal cycle, according to a regular pattern. This is a strong mechanism for generating vertical spatial patchiness, which is probably a result of optimal foraging and predator avoidance (Lalli and Parsons, 1997).

The processes mentioned above are mostly small-scale mechanisms, operating at timescales of a few hours or a day, and at lengthscales of a few hundred metres (see Barnes and Hughes (1982) for a table summarising temporal and spatial scales of patchiness processes). Indeed, it has been suggested that biological processes are generally responsible for the small-scale patchiness observed in the ocean (Popova et al., 2002). Physical mechanisms may also be responsible for small-scale patchiness (e.g. wave action; Langmuir circulation - see below), but in general the physical flow sets the large-scale structures.

1.2.1.2 Physical drivers of patchiness

Any physical mechanism generating patchiness in nutrient and light supply has the potential to generate patchiness in plankton distributions.

High productivity is often associated with frontal regions, where two distinct water masses meet. This high productivity may be due to associated upwelling, which brings fresh nutrients to the surface from depth, or because the nutrient content of the mixed water is more suitable for phytoplankton growth than that of either discrete water mass (Slobodkin, 1999) (for example, if the different water masses contain a different amount of the nutrients required for phytoplankton growth). Additionally, studies have shown that aggregation of certain phytoplankton species

may result from the interaction of their inherent buoyancy properties with the subduction of water masses at fronts (Kemp et al., 2006). Zooplankton may then also respond to the elevated phytoplankton concentration, aggregating along the front (Fielding et al., 2001). Light availability can also vary at fronts if, for example, the water mass containing a particular population of plankton is subducted at the front, generating vertical patchiness.

Upwelling regions are also associated with mesoscale eddies, again bringing nutrients to the surface, stimulating phytoplankton growth. Additionally, since eddies can act as trapping regions, preventing cross-flow between the ambient water and material within the eddy, patchiness at the mesoscale can result or be sustained (Garçon et al., 2001). This patchiness may last for months as the eddies travel across the ocean. This has been seen in rings spun off, for example, from the Gulf Stream (Barnes and Hughes, 1982).

Recently, a hurricane passing across the North Atlantic was observed by satellite to leave high productivity regions in its wake, due to stirring up by the hurricane of the lower, nutrient-rich layers (Connor, 2004). Another "seed heterogeneity" (Martin, 2003) that can generate patchiness in phytoplankton distribution is fertilisation by iron, another requirement for plankton growth, in areas of iron depletion. In the case of Abraham et al. (2000), the iron fertilisation in a patch of water in the Southern Ocean was deliberate for experimental purposes; satellite imagery showed evidence of an area of high productivity caused by the iron fertilisation. Similar effects may arise from dust storms or volcanic eruptions sporadically depositing large amounts of iron into the ocean (Duce and Tindale, 1991).

We can think of the above mechanisms as creating an initial patchy stucture of water with high biomass levels, surrounded by less densely populated waters. An interesting question is how this stucture is modified by, and interacts with, the physical flow. For a thorough review of this matter, focusing on the effects of lateral stirring and mixing, see Martin (2003). What follows is a brief discussion of the main issues.

Some studies suggest thinking of any spatial stucture as comprising many individual patches of varying size, so that we should in theory be able to examine the

dynamics of a single "patch" in isolation (Kierstead and Slobodkin, 1953; Petrovskii, 1999). This approach allows simplification of what is obviously a complex structure.

Initial studies in this area looked at the interaction of the effects of phytoplankton growth and diffusion. Assuming an exponential growth of phytoplankton, Kierstead and Slobodkin (1953); Skellam (1951) found there to be a critical length scale of patch, proportional to $\sqrt{\frac{D}{k}}$ (where D is the diffusive rate and k the growth rate), at which growth just balances diffusion. Below this lengthscale, growth is too slow and the patch is dispersed. Above the critical length, the patch persists. This kind of model came to be known as KiSS, after the authors Kierstead, Slobodkin and Skellam who first used it (Kierstead and Slobodkin, 1953; Slobodkin, 1999; Skellam, 1951). Later studies sought to improve the representation of the biology, by including grazing by zooplankton, and the physics, by considering the scale-dependence of diffusivity (Petrovskii, 1999). These studies confirmed the idea of a critical lengthscale for patch persistence. However, as Martin (2003) points out, the value of that critical lengthscale depends on the biological and physical models used, something demonstrated in a broader context in this thesis.

Diffusion, in the models above, is a dissipative influence: the biology has to fight to retain structure in the face of the smoothing effect of diffusion, which drives the system towards homogeneity. This need not be the case. Turing (1952) proposed a model, now known as the Turing mechanism, whereby steady state spatial heterogeneity may result from the interaction of two chemical (or biological) species with different diffusivities. Suppose one species (say, zooplankton) exerts a control (in this case, grazing pressure) over the other (in this case, phytoplankton), and that the first species diffuses more quickly than the second. If the two are perturbed from equilibrium locally, then the smoothing effect of diffusion will work more quickly on the first species (zooplankton) than the second, relaxing the control and allowing the second species to flourish (a phytoplankton bloom). However, since the first species has already spread out beyond the range of the second, a barrier is formed which restricts the spread of the bloom. In this way, permanent spatial heterogeneities may result. For more detail, see Turing (1952) and Murray (1989).

Whilst diffusive processes have historically been seen as the fundamental pro-

cesses behind plankton patchiness structure, Abraham (1998) argued that patchiness can also be affected by non-diffusive advection, or stirring. The bias towards diffusion-based theories has been partly because, unlike diffusion, it was difficult to adequately incorporate a turbulent flow into a plankton population model (Abraham, 1998).

We see evidence from satellite images of horizontal stirring by the flow as it draws plankton patches out into long tendrils and filaments (e.g. Robinson, 1997; Abraham et al., 2000). As well as influencing the spatial structure, stirring may affect the persistence of a particular patch in time, by increasing the entrainment of nutrients along the patch boundary (Abraham et al., 2000).

Such filaments were shown by Martin (2000), who looked at the combined effects of diffusion, population growth and straining by the flow, to have a minimum width. This minimum width was found to be affected by the parameters of the flow only: effective diffusivity and rate of strain. Diffusion has a widening effect; strain a lengthening and narrowing effect. The biological parameter, the growth rate, determined the amplitude of the population within the filament. Martin (2000), however, assumed unlimited exponential growth of the population; McLeod et al. (2002) used a more realistic growth term that accounted for growth limitation inflicted by zooplankton grazing and nutrient depletion. There, the biological parameters were found to influence the minimum filament width, showing that such studies are sensitive to the biological dynamics at work and the choice of how to model them. This issue will be addressed further in this thesis.

Neufeld and Lopez (1999) and Neufeld et al. (2002) focused on turbulent effects, studying the evolution of an active tracer stirred by chaotic advection. The tracer model used was intended to represent a chemical species, but could equally be taken to represent phytoplankton. Once again, the final structure observed depended upon the balance between the population propagation, in the form of a reaction-diffusion front, and stretching by the chaotic advection. In the case of relatively slow stirring compared with phytoplankton growth, a steady filamental structure was found to persist. When the stirring rate was fast, patchiness was smoothed out into a homogeneous steady state.

An interesting special case is that of Langmuir circulations. These arise when moderate winds blow persistently in one direction across the sea surface. The result is a series of parallel vortices, rotating along horizontal axes aligned with the wind, with adjacent rolls turning in opposite directions. This creates a series of convergent and divergent bands (Barnes and Hughes, 1982). This physical regime interacts with the buoyancy properties and swimming tendencies of phytoplankton and zooplankton. Any downward-swimming or sinking organism will tend to aggregate in upwelling areas; upward-swimming or floating organisms, in downwelling areas. Neutrally buoyant organisms, or those without swimming abilities, become randomly distributed. The net result is a spatially and taxonomically patchy distribution (Lalli and Parsons, 1997; Bees et al., 1998).

The general conclusion to be reached is that whether coherent features in plankton distributions persist is dependent upon the balance between dissipative forces and plankton population propagation. The distribution of an inert tracer under the influence of a physical flow will inevitably be determined by that flow. Active tracers, such as phytoplankton, are capable of retaining independent structure under this influence.

1.2.2 Significance of plankton patchiness

The study of plankton and their spatial and temporal distributions is important for two primary reasons.

First, plankton play a major role in the carbon cycle. The growing awareness of possible anthropogenic forcing of the global carbon cycle has increased interest in its study; this is impossible without a model of the upper ocean ecosystem (Popova, 1995) and an understanding of the biological pump, to which plankton are key (Sarmiento and Gruber, 2006).

Second, phytoplankton are the main primary producers of the marine ecosystem (Lalli and Parsons, 1997) and plankton in general are a vital component of all marine food webs. Hence understanding how plankton are distributed is useful in the study of all other marine life. Of particular interest are those food webs of which humans are a part, i.e. those containing commercial fisheries species.

Patchiness in plankton distributions has been shown to be linked with levels of primary production (e.g. Smith et al., 1996; Martin and Richards, 2002). Additionally, heterogeneity can affect the ecosystem dynamics themselves by impacting upon the stability and persistence of a population (Steele, 1974). For example, in their study of freshwater protists, Holyoak and Lawler (1996) found that a patchy population has a reduced risk of extinction, since migration between interacting patches allows recolonisation of depleted patches.

Since current Global Carbon Cycle Models (GCCM's) are incapable of resolving features of the mesoscale and smaller (Fasham, 2003), which is the scale at which much of the variability in plankton distribution is seen (Steele, 1978), they may be incurring large errors. A better understanding of heterogeneity in real-world and modelled plankton dynamics may therefore improve our ability to model, understand and predict carbon cycle dynamics.

1.2.3 Modelling plankton distributions

In general, the time evolution of an ocean biogeochemical tracer C, such as phytoplankton or nitrogen concentration, may be expressed by continuous reaction-diffusion-advection equations

$$\frac{\partial C}{\partial t} + \underline{\mathbf{u}} \cdot \nabla C - K\nabla^2 C = f(C) \tag{1.1}$$

$$\text{advection} - \text{diffusion} = \text{sources} - \text{sinks} \tag{1.2}$$

where $\underline{\mathbf{u}} = (u, v, w)$ represents the flow and K is the diffusivity such that each each variable evolves according to the physical advection and diffusion terms on the left and chemical and biological reaction terms, represented by the function f, on the right. A typical approach for biogeochemical modelling is to take a simplified version of the equations, discretised in space and time, and integrate each of the equations forward in time (Fasham, 2003).

The biological dynamics in each spatial "grid-cell" is represented by a plankton ecosystem model which attempts to break down the complicated structure of a marine ecosystem into a number of components (the set of tracers) and the interactions between them. Components are assumed to be well-mixed within each

grid-cell so that grid-cell populations are considered rather than individual organisms. The choice and number of components varies between models, reflecting the modelling aims and assumptions of different studies: degree of realism must be balanced against computational and analytical tractability. The model components become the variables of the dynamical system. For example, many studies consider only nutrient, phytoplankton and zooplankton (e.g. Steele and Henderson, 1981), whilst the Fasham et al. (1990) model contains seven components and the ERSEM (European Regional Seas Ecosystem Model Baretta et al., 1995) has a substantially larger number of interacting components.

The flow of matter as a result of interactions between and processes affecting the ecosystem components is parameterised in the model as a function of the biological variables. The usual functional forms and accompanying parameters are based on a combination of mechanistic understanding, field work and laboratory-based studies (see e.g. Sarmiento and Gruber, 2006) and are all subject to a lesser or greater degree of contention and uncertainty. In many cases, modellers may select a biological model "off the shelf" through subjective choice or simply because a model is well-studied; a particular set of biological model parameters will be chosen and the model and parameters applied uniformly across the entire area of study (Fasham, 2003).

The spatial resolution of the simulation is dictated by a variety of factors such as available computing power, the sampling resolution of observations that the study aims to reproduce or, again, subjective choice. Most current GCCM's have a spatial resolution of no better than 1 degree (about 100 km). Any unresolved biological or physical processes must be parameterised in the model.

The coupled biophysical model can then be used to investigate and predict observed features of plankton distribution and production for the global ocean or a particular region (e.g. Levy and Klein, 2004; Abraham, 1998). Although much progress has been made, and studies are aided by the wealth of high resolution data that came with the advances in ocean remote sensing, error still arises from problems such as a lack of a mechanistic basis for many of the equations describing evolution of biological variables, insufficient data to constrain model parameters, variation and inadequecy in the way in which the physical flow is represented, and coarse spatial

resolution due to computational expense.

1.2.4 Synchronisation theory

The earliest recorded interest in the synchronisation phenomenon was by Christiaan Huygens, the Dutch astronomer, mathematician and physicist, who observed in 1673 how two swinging pendulum clocks hanging from a wooden beam may become either frequency-locked with a constant phase-lag of π or fully synchronised as a result of vibrations, caused by the motion, travelling along the beam (Pikovsky et al., 2001). More recently, examples of synchronisation in systems of interacting oscillators have been found in all areas of science including electronics (e.g. Taherion and Lai, 1999; Neff and Carroll, 1993), biology (e.g. Strogatz and Stewart, 1993), epidemiology (e.g. Boccaletti, 2002), lasers (e.g. Barbay et al., 2000) and human behaviour (e.g. Néda et al., 2000).

In essence, the standard type of biophysical model described above consists of an ensemble of interacting grid-cells, in each of which the biology evolves according to the chosen ecosystem model, with the interaction provided by the prescribed physical circulation model. Such a system becomes the concern of the area of mathematics known as synchronisation theory, which studies how the natural rhythms of individually oscillating objects adjust as a result of couplings between them (Pikovsky et al., 2001). This coupling may take the form of direct interaction, where coupled oscillators directly influence one anothers behaviour through explicit coupling, or indirect influence, where coupling is due to an external force, or a combination of the two. The geometry of the coupling, such as interaction between nearest-neighbour (local coupling) or all oscillators (global coupling) will depend upon the particular system under study.

Suppose we have an ensemble of n interacting oscillators s_i. By the term "oscillator" we mean behaviour which is time-varying, including for example periodic, chaotic or noisy oscillation. If the interaction between the oscillators causes their states to become uniform in time, i.e. $s_1(t) = s_2(t) = \ldots = s_n(t)$, then the system is said to be *fully synchronised*. In this case, the coupling is sufficient to unify the system and lock the frequencies, phases and amplitudes.

Full synchronisation is not the only kind of synchronous behaviour observable in theoretical and real-world systems of coupled oscillators. If the coupling overcomes a natural disorder in frequencies, where the natural frequency of each oscillator is the frequency at which it would oscillate in isolation of interaction, causing all oscillators to evolve at a common frequency, then the system is described as *frequency-locked* (e.g. Sherratt et al., 2000). In this case, if there exists a constant phase lag between frequency-locked oscillators then the system is said to be in a state of *lag synchrony* (Taherion and Lai, 1999; Rosenblum et al., 1997). For a zero phase lag, we call the system *phase synchronised* (Blasius and Stone, 2000). In this state of phase-locking, oscillator amplitudes may still differ. Only when frequencies, phases and amplitudes are all locked do we call the system fully synchronised. In addition, instead of synchrony occurring across the whole ensemble, the system may break up into subgroups of (fully/phase/frequency, etc) synchronised oscillators, with no synchrony between subgroups. This is referred to as *cluster synchronisation* (Osipov and Sushchik, 1997; Belykh et al., 2003; Pascual et al., 2002). As the strength of interaction between oscillators is increased from zero, the usual transition is from asynchronous oscillations to clustering to frequency locking to lag synchrony to phase locking to full synchrony. However, Blasius and Montbrió (2003) have shown that the increase in synchrony with increasing coupling may not always be monotonic and that in some cases the onset of coupling can lead to an initial *increase* in disorder in the system. This phenomenon will be seen for a lattice of interacting non-identical plankton populations in Chapter 3 of this thesis.

Many interesting examples of synchrony in coupled oscillators and the manner in which they are coupled may be found in Strogatz (2003). Examples with greater mathematical detail may be found in Pikovsky et al. (2001). For the purposes of the present study, we focus on examples of synchronisation in population dynamics.

1.2.5 Application of synchronisation theory to population dynamics

Synchronised fluctuations across large distances have been documented in the population numbers of a wide variety of species. Examples include spatial synchrony in ro-

dent (Sherratt et al., 2000; Ydenberg, 1987; Haydon et al., 2001), bird (Ranta et al., 1995), fish (Ranta et al., 1995), mammal (Haydon et al., 2001; Grenfall et al., 1998), insect (Benton et al., 2001) and plankton (Strogatz and Stewart, 1993) species.

A well-studied example which serves to illustrate some of the processes at work is the cycle of Canadian hare and lynx numbers (Elton and Nicholson, 1942), which oscillate on a roughly ten-year cycle. Remarkably, the abundances in regions thousands of miles apart are in phase, although amplitudes differ. It has been hypothesised that the main synchronising agents at work on the population numbers are, (i) migration between adjacent populations (Blasius and Stone, 2000) and, (ii) the influence of a common environmental forcing - both continuous seasonal forcing and sporadic stronger forcing events such as storms (Moran, 1953). The *direct coupling* of the dispersal between populations and the *indirect coupling* of a common environment both cause the individually oscillating hare-lynx prey-predator populations to adjust their oscillations to a common frequency.

The ubiquitousness of synchronisation phenomena in population dynamics has led Ranta et al. (1995) to claim that studying spatial synchrony, where previously the focus has been on the temporal fluctuations of individual populations, should help ecologists to get to the core of the workings of population dynamics. To this end, studies have been carried out using a combination of empirical data and ecosystem modelling to try to identify synchronised dynamics in spatially extended populations to elucidate the main synchronising influences, or forms of coupling, at work. There has been a certain amount of debate over whether direct or indirect influences are of most importance in maintaining synchrony (Blasius and Stone, 2000).

Modelling approaches to synchrony in natural populations generally consider a spatial distribution as a metapopulation: the internal dynamics of each population is modelled as an independently oscillating ecosystem and the lattice or chain of populations interacts according to the prescribed coupling (Hanski, 1998). This approach, combined with results on synchronisation theory from the mathematical and physical literature has led to some interesting results on how spatial synchrony might emerge in spatially-extended ecosystems.

Some studies have focused on the indirect coupling effect of a common or corre-

lated environmental forcing, such as correlation between the climates affecting each population. Moran (1953) studied the previously-mentioned synchrony observed between hare-lynx populations in Canada and suggested that, for a population with linear internal dynamics, the correlation between populations should be equal to the environmental correlation. This has latterly been referred to as the *Moran effect* but there is uncertainty over how well the theory extends to nonlinear population dynamics and how to separate the effect from synchronisation caused by dispersal (e.g. Ranta et al., 1995).

One study, by Grenfall et al. (1998), looked at the synchronised fluctuations in the density of feral sheep populations on separate islands of the St Kilda archipelago. In this case, there is no inter-population dispersal, so that observed synchrony arises from a correlated environment. Grenfall et al. (1998) hypothesised that environmental shocks such as March gales or increased temperatures in April are able to influence the phase of oscillation of the sheep populations, either negatively in the case of adverse or positively in the case of favourable weather conditions, to bring the separated populations into synchrony.

Ranta et al. (1995) collated examples of spatial synchrony in different species from all over Finland. They noted the common pattern of decreasing levels of synchrony with increasing distance between populations. They used a metapopulation model to investigate the relative influences of internal dynamics, dispersal and the Moran effect on setting this observed pattern by selecting three different population models and coupling the metapopulation by either dispersal, environmental forcing or both. As expected, Ranta et al. (1995) found that the Moran effect was capable of establishing synchrony but that there was no trend with increasing distance between populations. This effect was seen when coupling the populations by dispersal alone and the level of synchrony was not enhanced by including environmental forcing.

Similarly, the study by Sherratt et al. (2000) on field voles in northern England found that small levels of migration were sufficient to reproduce the observed spatial patterns of synchrony and travelling waves without the need to include environmental forcing. The presence of a travelling wave indicates that as a result of small-scale migration (voles typically migrate over small distances of order 100 m)

between neighbouring populations the metapopulation is able to lock in frequency but not in phase. Sherratt et al. (2000) used several forms of coupling in their modelling study, with voles all either migrating over short distance or with some able to travel further. Their results showed that the form of coupling is important in establishing the precise patterns observed, e.g. the speed of the resulting travelling wave. The vole data and the modelling results of Sherratt et al. (2000) are good examples of frequency synchronisation and clustering in coupled populations.

Haydon et al. (2001) also illustrate the importance of the strength and extent of coupling in establishing synchrony. They looked at fluctuations in mink and muskrat populations across the whole of Canada, which, when converted into a time-series of phases, show patterns of synchrony. They used the phase data to identify whether the phase of oscillation of each population generally draws closer to that of its neighbours with each year, indicating a constant level of direct coupling, or whether the phases drift apart and are sporadically brought sharply together, indicating environmental shocks. They found that the level of coupling varied across the region, resulting in varying level of synchrony. The variation in coupling strength was hypothesised to be related to varying topography from west to east across Canada, e.g. a smaller amount of migration may be possible in the more difficult mountainous terrain of the western part of Canada, disrupting the synchronising influence.

Another important observation by Haydon et al. (2001) was that the two species under consideration, mink and muskrat, although exhibiting similar spatial patterns of synchrony, are time-lagged with respect to one another; mink lag 1 to 2 years behind the muskrat, although both cycle with an 8 to 10 year cycle. Haydon et al. (2001) believe that this reflects the different density-dependent internal dynamics of the two species. This indicates the importance of recognising the two influences of the *internal dynamics* of each population comprising the metapopulation and the *way in which these populations are coupled* in setting the type of emergent spatial structure observed.

Finally, Ydenberg (1987) proposed that some species may become synchronised not by the Moran effect or disperal but because of a nomadic predator. If the predator is able to distribute itself among the prey depending on the prey density,

and if this is able to influence the phase of oscillation of the prey species, then synchrony might result. For example, if the fluctuations in prey populations comprising the metapopulation are all in phase then the predator would distribute itself evenly throughout the region and synchrony would be maintained. If certain populations were in a low or high phase, the predator would move away from or into those areas, respectively, and, if the prey species could somehow alter its phase, then synchrony may be restored. Ydenberg (1987) hypothesised that the change in phase of oscillation of the prey species may result from direct predation or from survival mechanisms in the prey such as changes in foraging or breeding patterns as a result of intense predation. Ydenberg (1987) suggested that this synchronising mechanism might be more applicable than the Moran effect for species where synchronised dynamics have been observed over distances large enough (of order 1000 km) for significant climatic variation.

We see that ecologists have applied synchronisation theory to a variety of terrestrial ecosystems by modelling an area of interest as a spatially-extended metapopulation of discrete populations, interacting directly or indirectly via, for example, migration or a common environmental forcing. Such studies have been successful in yielding results on the causes of the common phenomenon of synchrony in terrestrial population dynamics. To summarise, the occurence and nature of synchrony have been shown to depend upon the internal dynamics of the individual populations, the form (e.g. direct or indirect interaction), strength (e.g. rate and extent of dispersal) and time dependence (e.g. constant or peaking sporadically) of the coupling between populations, and the geometry and extent of the metapopulation (e.g. number of and distance between populations).

1.2.6 Application of synchronisation theory to plankton patchiness

The approach described above may be applied to the study of plankton distributions: by viewing the distribution of plankton in an area of ocean as an interacting ensemble of individual plankton populations, it is apparent that synchronisation theory is directly applicable to plankton patchiness and should have much to tell us

about emergent structure in modelled and real-world plankton distributions. Since synchronisation theory is concerned with oscillators, this assumes that plankton dynamics are oscillatory (which we take here to mean time-varying and not necessarily oscillatory with a regular period) at least some of the time and may be realistically represented as such. We justify this assumption on the basis of modelling work (e.g. Ryabchenko et al., 1997), empirical work (Fussman et al., 2000).

A distribution may be thought of as a metapopulation of plankton populations, interacting via, for example, the physical flow, external forcing and/or dispersal of individuals between populations. This is analogous to the standard biophysical modelling approach outlined in Section 1.2.3. The application of synchronisation theory to plankton population modelling is discussed below.

- **Direct coupling**

  Since plankton are largely incapable of movement independent of ocean currents, the most obvious example of direct coupling between plankton populations might be dispersal caused by mixing and stirring. Another example would be migration by those zooplankton that are more capable of independent movement, perhaps for the purposes of foraging and mating.

  Hillary and Bees (2004a,b) carried out the first studies in this area by considering a lattice of plankton populations, represented by the Nutrient-Phytoplankton-Zooplankton (NPZ) model of Steele and Henderson (1981) with a fixed set of spatially uniform parameter values, coupled via a simple nearest-neighbour flux between patches. By varying the strength of coupling between populations and looking at the stability of the fully synchronised state, they were able to establish a critical strength of coupling required for homogeneous dynamics to persist. Using this general set-up, Hillary and Bees (2004a) were able to explore a number of different factors affecting the ability of the system to synchronise. Their results suggested some dependence of the critical coupling on the number of populations comprising the lattice, a result seen in terrestrial studies (e.g. Ripa, 2000; Ylikarjula et al., 2000).

  As well as considering a lattice of *identically*-represented plankton populations Hillary and Bees (2004a) also looked at the more realistic case of *spatially*

varying dynamics by applying a small mismatch to the zooplankton mortality parameter of each population. For certain values of coupling, phase synchrony was found to result, with populations frequency locked and in-phase but with differing amplitudes. As described in Section 1.2.5, this is a phenomenon commonly observed in non-plankton ecological data (Elton and Nicholson, 1942).

For the same system, Hillary and Bees (2004a) also found that for biological parameters normally resulting in chaos in the uncoupled NPZ dynamics, a smaller critical coupling was required for a smooth relationship, such as that of phase synchrony, to exist between patches. This suggests that chaos aids the formation of stable synchrony in a metapopulation, agreeing with the conclusion of Ripa (2000) that unstable local dynamics are an aid to dispersal as a synchronising mechanism.

The set-up used by Hillary and Bees (2004a) is a simple example of a coupled biophysical model: biological dynamics are represented by an ecosystem model common to all grid-cells and the nearest-neighbour coupling approximates the advective and diffusive processes of the physical flow. The studies of Hillary and Bees (2004a,b) have highlighted a number of the factors affecting the emergent structure in such a model; the number of populations (or grid-cells) in the lattice, the type of coupling, the choice of biological model and the corresponding parameters and whether or not spatial variation in underlying dynamics is considered. All of these effects require further study to establish their relative importance.

- **Indirect coupling**

  Since fluctuations in plankton abundances are driven by such influences as variations in sunlight and wind-induced sea-surface mixing, it is equally conceivable that plankton populations could become spatially synchronised by common environmental influences. As a simple example, Strogatz and Stewart (1993) describe how the glow rhythm of the bioluminescent algae *Gonyaulax* is, under usual conditions, synchronised between individuals, each having a

nearly 24 hour period. If kept in a dim tank in a laboratory, the individuals quickly become desynchronised with a wider range of frequencies of oscillation, indicating that it is not direct coupling between individuals but the indirect coupling of the day-night light cycle that causes the synchrony.

Hillary and Bees (2004a) considered the effect of indirect coupling on the plankton lattice by formulating the dynamics in terms of a drive-response system, where the usual NPZ system is driven by either a Rössler oscillator or a slightly different NPZ system. These two different forcings represent the cases of driving by an abstract external force unrelated to the NPZ dynamics, such as weather, or driving by an independent influence acting on similar time scales, respectively. Again, the strength of the driving force was varied and the critical coupling required for synchrony calculated. Their results indicated that the different time-scales on which the driving force acted influenced the strength of coupling required for homogeneous dynamics, with a driving force with higher frequency able to synchronise the populations for a smaller coupling strength.

Finally, the emergent structure in a plankton metapopulation could be influenced by a nomadic higher predator, as suggested by Ydenberg (1987) for terrestrial species. Malchow et al. (2000) explored this possibility by coupling a plankton biomass model to a rule-based fish dynamics model. Schools of fish were able to alter their position in the simulation based on feeding preferences and rules of movement. Spatially patchy dynamics were found to result with some evidence of clustering.

The work described here has demonstrated the applicability of synchronisation theory to the study of spatial patterns in plankton distributions by viewing a region of ocean in an Eulerian sense as an ensemble of interacting plankton populations. This approach is analogous to the way in which modellers simulate ocean biogeochemistry, so that synchronisation theory has the potential to yield results on the emergent spatial organisation of plankton seen in these simulations and in the ocean. So far, there is some indication of the influence of a number of factors, including the strength and geometry of interaction, the number of populations comprising the ensemble and the dynamic properties of the individual populations, on the ability

of such a simulation to manifest synchronised dynamics. There is also some suggestion that the synchronisation phenomena seen in terrestrial population dynamics (as described in Section 1.2.5), such as phase-synchrony and the breaking down of the ensemble into synchronised clusters, may carry over to oceanic studies, where the complicated interaction between populations caused by the diffusive and advective properties of the physical flow provide a new challenge for the application of synchronisation theory to spatiotemporal population dynamics. Further work is required to determine the relative importance of these factors and their consequences for patterns of patchiness in plankton in the ocean.

1.3 Aims and outline

By applying the methods of synchronisation theory to a region of ocean modelled as an interacting lattice of plankton populations, this study aims to address the following principal questions.

- What determines the ability of a matrix of interacting oscillatory plankton populations to exhibit synchronised population dynamics?
- What are the consequences for biophysical modelling studies of plankton patchiness?
- Ultimately, how useful can the methods of metapopulation dynamics and synchronisation theory be in the study of spatial patterns of plankton patchiness in the ocean?

Chapter 2 begins, for mathematical simplicity, with the case of *identically represented* populations. We carry out a thorough investigation of a number of factors suggested by the work of Hillary and Bees (2004a,b) to impact upon the ability of the plankton population ensemble to exhibit synchronised dynamics. We determine the influence of (i) the number of populations comprising the ensemble, (ii) the biological model used to represent the dynamics of the individual plankton populations and (iii) the biological model parameters. Population are coupled by a

simple nearest-neighbour coupling term representing mixing and stirring between populations at sub-grid-cell scales.

In Chaper 3 we improve the realism of the simulation, allowing spatial variation in the population dynamics by considering a lattice of *non-identical* populations. At the same time, we extend the approach from the 1-dimensional chain considered in Hillary and Bees (2004a,b) to the oceanographically more relevant case of a 2-dimensional lattice of populations. The biological model used for each population is the same but spatial variation is introduced by applying a small mismatch to the accompanying biological parameters. It will be seen that this introduces a rich array of synchronisation effects such as clustering and frequency locking. We investigate the impact of the strength of interaction between populations, the number of populations comprising the ensemble and the spatial resolution of the simulation.

Continuing with non-identical oscillators, Chapter 4 will consider the impact of *advection* of populations on the emergent spatial properties seen in previous studies, investigating in particular the robustness of the results of Chapter 3 to the more realistic representation of the effects of physical flow on the populations. This moves the study firmly away from analogies with terrestrial metapopulation studies, providing an initial look at how the synchronous properties of the plankton metapopulation might be modified by the stirring action of the flow acting at scales larger than the individual populations.

In Chapter 5 we summarise the results on synchronisation in a lattice of plankton populations and discuss the impact of these results on biophysical modelling studies. We draw conclusions about what synchronisation theory can tell us about emergent spatial structure both in simulations and in oceanic plankton distributions and attempt to answer the question of how useful synchronisation theory can be in the study of plankton patchiness, as well as discussing future directions for research motivated by the findings and limitations of this study.

Chapter 2

Identical Oscillators

2.1 Introduction

In this chapter, we carry out an initial investigation into the synchronous properties that may emerge in biophysical modelling of the ocean, and the role of some of the modelling parameters involved. [1]

As described in the previous chapter, a typical biophysical model may be thought of as an ensemble of interacting plankton populations, so that the methods and results of synchronisation theory are directly applicable. The biological dynamics are typically represented by a plankton ecosystem model common to all grid-cells of a spatial simulation. A wide range of models exists, reflecting the variety of ocean regions and modelling aims that have been the concerns of different studies (Totterdell, 1993). It has not generally been considered what impact the choice of grid-cell ecosystem model, from the many developed in the literature, might have upon the results of biophysical modelling. This chapter therefore aims to address the following question: for oceanographic modelling, what impact does the choice of biological representation at grid-cell level, and the number of grid-cells used, have upon the dynamic features of the full coupled biophysical system?

Specifically, we will consider a chain of n grid-cells with a nearest-neighbour coupling (with no-flux boundary conditions) designed to approximate mixing processes between adjacent grid-cells. This mixing is a proxy for the effectively diffusive effects

[1] The results presented in this chapter have been published in Guirey et al. (2007).

of flow at scales smaller than the grid-cell.

The biology within each grid-cell is identically represented by a plankton ecosystem model. We consider three different plankton models, all of which are typical of those used in the literature to represent upper-ocean biological processes. The models, which will be introduced in Section 2.2.1, all represent plankton population dynamics but differ in terms of state variables and functional forms. Within this framework, by varying the strength of the flux between grid-cells we will establish the strength of coupling required for the system to exhibit synchronised (spatially homogeneous) dynamics as a function of the choice of (i) biological model, (ii) biological model parameter values, and (iii) the number of grid-cells forming the ensemble. As the coupling is increased from zero, the strength of interaction at which emergent structure becomes stably synchronised is referred to as the critical coupling.

It is necessary in this initial chapter to consider the simplest possible case; later chapters will build upon its results. Namely, we consider the case of *identical* oscillators: the biology within each grid-cell of the ensemble is represented by the same system of ordinary differential equations and accompanying set of parameter values. Realistically, we would expect spatial and temporal variation in plankton dynamics; for example, phytoplankton growth rates may vary spatially as a result of differences in temperature or species composition. We incorporate such variation in Chapter 3.

Ecosystem models may exhibit different types of dynamical behaviour, from steady state to limit cycles to chaos, depending upon the functional forms used to represent biological processes and the choice of parameter values (e.g. Edwards and Brindley, 1999). This change in dynamical behaviour is also observed in empirical plankton studies (Fussman et al., 2000). Work has shown that a coupled system of identical oscillators, such as that being considered here, will always synchronise stably regardless of coupling strength if the individual oscillators exhibit steady state or limit cycle solutions (Pikovsky et al., 2001); this is a property that vanishes immediately if we consider *nonidentical* oscillators (representing spatial variation), because the mismatch in representation of each oscillator introduces a desynchronising influence that is lacking in the system of identical oscillators. On the other hand, a system of coupled *chaotic* oscillators has an inherent desynchronising mechanism

provided by the exponential divergence of nearby trajectories that is characteristic of a chaotic system (Strogatz, 1994), even when each oscillator is represented identically mathematically. Hence, since identical coupled limit-cycle or steady-state oscillators will always stably synchronise, we only need in this chapter to focus on regions of model parameter space for which the models exhibit chaotic dynamics. In particular, we determine the ability of the coupled system to synchronise for the "most chaotic" (i.e. nearby trajectories separate most rapidly) region of parameter space. Behaviour at this most extreme point will then bound the behaviour for the whole of parameter space, as will be explained in Section 2.2.4. The effects of the noise and spatial variation in parameters that would, in the real-world case, be inherent in the system, are not directly studied in this chapter. However, Chapter 3 will build on these results by considering the more biologically realistic scenario of non-identically represented patches.

2.2 Methods

2.2.1 The biological models

To reduce typical models of the global ocean carbon cycle to the simplest possible case, we consider an ensemble of effectively diffusively-coupled grid-cells. The plankton population dynamics within each grid-cell, which may be thought of as a region of ocean of, as yet, unspecified length-scale, is represented by a plankton ecosystem model typical of those used in the literature. In particular, we have a chain of n coupled grid-cells, with the plankton population within each grid-cell evolving according to

$$\dot{\mathbf{v}}_\mathbf{i} = F(\mathbf{v}_\mathbf{i}) + \varepsilon \mathbf{v} \cdot \mathbf{q}$$

where $\mathbf{v} = (\mathbf{v_{i-1}}, \mathbf{v_i}, \mathbf{v_{i+1}})$ and each population $\mathbf{v_i} = (s_1, s_2, \ldots, s_m)$ consists of m species s_j at position i along the chain. The scalar ε in units of d^{-1} determines the strength of coupling between grid-cells, and the vector

$$\mathbf{q} = \begin{cases} (1, -2, 1) & i \in [2, n-1] \\ (0, -1, 1) & i = 1 \\ (1, -1, 0) & i = n \end{cases}$$

specifies the coupling configuration, i.e. nearest-neighbour coupling with no-flux boundary conditions.

The function F is the system of differential equations representing the biological evolution of each patch in isolation. The basic biological models selected for this study were first formulated by Steele and Henderson (1981) and Hastings and Powell (1991) (hereafter referred to as SH81 and HP91, respectively), and are typical of those used in biophysical modelling studies of the pelagic ocean (Totterdell, 1993). The models were selected as examples that use different sets of state variables (i.e. differing in their choice of which components of the ecosystem to explicitly represent) and different functional forms for the trophic interactions, relecting different assumptions made about the modelled environment. A brief description of the models will be given here, but fuller details may be found in the above references and in Edwards and Brindley (1996) and Edwards (2001) for SH81 and Caswell and Neubert (1998) for HP91.

Both SH81 and HP91 are zero-dimensional models representing, by a system of autonomous ordinary differential equations, the processes occurring in a physically homogeneous upper ocean layer. SH81 (equations 2.1-2.3, with parameters given in Table 1), however, contains an implicit, biologically-inactive ($P = 0$) deeper layer with a fixed nutrient content, which acts by way of vertical mixing as a nutrient source for the upper layer biology.

SH81 models nutrient (N), phytoplankton (P) and zooplankton (Z) concentrations as follows:

$$\begin{aligned} \frac{dN}{dt} &= -\frac{aN}{(e+N)(b+cP)}P + rP + \frac{\zeta\beta P^2}{\mu^2+P^2}Z + \gamma dZ + k(N_0 - N) \qquad (2.1) \\ &= -\text{uptake} + \text{respiration} + Z \text{ excretion} + Z \text{ predators excretion} + \text{mixing}, \end{aligned}$$

$$\begin{aligned} \frac{dP}{dt} &= \frac{aN}{(e+N)(b+cP)}P - rP - \frac{\zeta P^2}{\mu^2+P^2}Z - sP - kP \qquad (2.2) \\ &= \text{uptake} - \text{respiration} - \text{grazing by } Z - \text{sinking} - \text{mixing}, \end{aligned}$$

$$\frac{dZ}{dt} = \frac{\zeta\alpha P^2}{\mu^2+P^2}Z - dZ \qquad (2.3)$$

$=$ growth due to grazing on P − higher predation.

Figure 2.1 shows a schematic of the model, indicating the flow of matter between components of the ecosystem.

The change in the autotrophic phytoplankton concentration is modelled as the sum of their growth, co-limited by nutrients and light (represented as a self-shading term), and losses due to respiration, mixing and sinking out of the upper layer, and grazing by zooplankton. Of the material grazed by zooplankton, a fixed fraction α is assimilated, contributing to zooplankton growth. A parameterisation of predation by higher predators closes the food chain from above. A fixed proportion of the material grazed by zooplankton and higher predators is excreted back to the nutrient pool. The zooplankton are assumed to possess enough mobility to remain within the mixed layer.

To investigate the effect of a simple change of functional form, leaving choice of state variables and general structure intact, a variation on the above model with alternative nutrient uptake term $\frac{a}{b(e+N)}P$ will also be considered and is hereafter referred to as SH81b. Here, we have a scenario where self-shading by the phytoplankton is assumed to be a negligible component of the light limitation.

The model HP91 was not specifically formulated to represent a plankton ecosystem, rather as a generic three-species food chain, but Caswell and Neubert (1998) and Srokosz et al. (2003) applied the model to a plankton ecosystem by taking the three trophic levels to represent phytoplankton, herbivorous zooplankton (H) and carnivorous zooplankton (C) components:

$$\begin{aligned} \frac{dP}{dt} &= RP\left(1-\frac{P}{K}\right)-\frac{a_1PH}{b_1+P} \\ &= \text{logistic growth} - \text{grazing by } H, \end{aligned} \tag{2.4}$$

$$\begin{aligned} \frac{dH}{dt} &= \frac{c_1a_1PH}{b_1+P}-\frac{a_2HC}{b_2+H}-d_1H \\ &= \text{growth due to grazing on } P - \text{grazing by } C - \text{natural mortality}, \end{aligned} \tag{2.5}$$

$$\frac{dC}{dt} = \frac{c_2a_2HC}{b_2+H}-d_2C \tag{2.6}$$

$=$ growth due to grazing on H − higher predation,

with parameter values given in Table 1. The model schematic is shown in Figure 2.2.

In HP91, carnivores are explicitly modelled and nutrient concentrations are not; that is, nutrients are taken to be non-limiting to phytoplankton growth. The model is somewhat simpler than SH81 in that recycling processes are not considered, so that the fundamental flow structure differs. This chain-like structure is crudely representative of a more productive region, so that the absence of a nutrient compartment and the simple structure are consistent. Phytoplankton population increases according to logistic growth, limited by a carrying capacity, and decreases due to grazing by herbivores, which are in turn grazed by carnivores. At each trophic level, a fixed proportion of grazed material is assimilated and the rest lost from the system. Herbivores and carnivores are each subject to a linear natural mortality term.

SH81/SH81b and HP91 represent different interpretations of the planktonic ecosystem: SH81 and SH81b are built on the assumption of bottom-up control; HP91 is built on the assumption of top-down control.

Historically, plankton modellers have settled upon a variety of functional forms to describe the interactions between the components of the ecosystem, and the above models are no exception. In order to make the models as directly comparable as possible, we can relate the parameters from the different functional forms in such a way that a similar range of values for that process can be used:

The model HP91 contains functions for growth, grazing and mortality, of which only the latter is of an equivalent form in SH81. In SH81, autotrophic growth is taken to be co-limited by nutrients, in the Michaelis-Menten form, and light availability. Growth takes maximum value $\frac{a}{b}$ at $P = 0$ in the limit as N tends to infinity. HP91 assumes logistic growth, limited by a carrying capacity. This has maximum value R, again at $P = 0$. Taking $R \equiv \frac{a}{b}$ we therefore set the models to have the same intrinsic maximum growth rate.

Taking nutrients to be non-limiting in the growth rate term of HP91, so that growth is limited by self-shading by the phytoplankton themselves, then the term $R\left(1 - \frac{P}{K}\right)$ may be equated with the self-shading component of the SH81 growth

rate term. Since we have $R \equiv \frac{a}{b}$, this leads us to compare $1 - \frac{P}{K}$ and $\frac{b}{b+cP}$. We may then equate half-saturation constants of these two forms: $\max(1 - \frac{P}{K}) = 1$, half of which is attained at $P = \frac{K}{2}$. Similarly, $\max\left(\frac{b}{b+cP}\right) = 1$, half of which is attained at $P = \frac{b}{c}$. Equating these two, we get $K \equiv \frac{2b}{c}$.

Grazing terms, although different, are formulated in both models in terms of the half-saturation constant (μ and b_i), the maximum grazing rate (μ and $b_i\zeta$ and a_i) and the assimilation coefficient (α and c_i), making each of these parameters directly relatable.

Table 2.1 summarises the above discussion. Reported parameter ranges are as collated by Edwards and Brindley (1996) in their study of SH81.

Temporal dynamics for each model are obtained by integrating the above equations forward in time using a forth-order Runge-Kutta scheme implemented by code written in the C programming language. The working of the code was verified by comparing with (i) integrations carried out using the ODE solvers available in the programming package MATLAB, (ii) results obtained by previous studies on the ecosystem models (see above references) and (iii) integrations carried out using the ODE package DsTool (see http//:www.mathlab.cornell.edu/dyn_sys/dstool/dstool.html).

2.2.2 Single grid-cell dynamics

Both models, under variation of parameter values within the reported ranges (see Table 2.1), are known to exhibit steady state, limit cycle and chaotic dynamics. It is necessary to quantify this behaviour because, as explained below, the behaviour of the individual grid-cell, as described by the biological model, impacts upon the full coupled system. An indication of the behaviour may be obtained by calculating the *Lyapunov characteristic exponent*, which measures the exponential rate of separation of nearby trajectories of the system in phase space. An m-dimensional dynamical system will have m Lyapunov exponents, quantifying the separation rate in all m directions of movement, but it is the largest Lyapunov exponent that indicates the kind of dynamics to be expected. A positive largest Lyapunov exponent indicates that there is at least one direction in which exponential separation rather than convergence of nearby trajectories in phase space can occur, leading to chaos in

a dynamical system (Strogatz, 1994). If the largest Lyapunov exponent is zero or negative then the system will exhibit limit cycles or steady states, respectively. We calculate a finite-time approximation of the largest Lyapunov exponent λ of a dynamical system using the following method.

The system of differential equations representing a single plankton population is integrated until transients have died and we are 'on' the attractor. The trajectory ($\mathbf{u}$) on the attractor will be a 'reference' trajectory. We then use a 'test' trajectory ($\mathbf{w}$), which at time t_0 is set a small distance d_0 from $\mathbf{u}$, to examine the rate at which nearby trajectories diverge.

If S_{i-1} denotes the amount by which the original perturbation has been 'stretched' at iteration step $i-1$, then the exponential rate of divergence λ_i is given by

$$S_{i-1} = e^{\lambda_{i-1} t_{i-1}}.$$

Let dS denote the stretch experienced over the next time step of integration of the ecosystem model. Then

$$S_i = e^{\lambda_i t_i} = e^{\lambda_{i-1} t_{i-1}} dS,$$

and, taking logs of both sides and dividing by t_i, we obtain

$$\lambda_i = \frac{\lambda_{i-1} t_{i-1} + \log dS}{t_i}$$

as a finite-time estimate of the Lyapunov exponent λ, so that λ can be calculated iteratively.

In the case of chaotic behaviour, the distance between the two trajectories quickly becomes too large for the definition of λ (as the growth of the distance between two initially *close* trajectories) to be valid. To avoid this problem, we rescale the distance to $\mathbf{u}$ at each time-step, preserving the direction of the vector but restoring the distance between $\mathbf{u}$ and $\mathbf{w}$ to d_0,

$$\mathbf{w}_{\text{new}} = \mathbf{u} + \frac{\mathbf{w} - \mathbf{u}}{dS}.$$

The process of iteration and rescaling is repeated until λ has converged. λ may be calculated for a range for values of a specified biological model parameter, allowing the occurrence of chaos or limit cycles to be tracked within a biologically acceptable range of values.

The above Lyapunov exponent calculations are carried out using code written in C. The method and its implementation were checked by comparing with known systems in the literature, in particular the Lorenz attractor, the Lyapunov exponents of which are given in Strogatz (1994) and also the previous work on SH81 by Hillary and Bees (2004a). The Lyapunov exponents calculations reported by Hillary and Bees (2004a) were found to contain some errors, which were subsequently shown to result from a minor typing error in the computer code used to make these calculations. Unfortunately, attempts to reconcile their calculations with the Lyapunov exponent calculations made for the current project, before the error and its source were identified, set this project behind by about six months.

The dynamics of the full coupled system of a chain of n plankton populations are obtained by integrating in time using a forth-order Runge-Kutta scheme.

2.2.3 Ensemble dynamics

The coupled system is *synchronised* if the dynamics resides on the region of phase space contained within the *synchronisation manifold*

$$\mathcal{M}_s = \{v_1, v_2, \ldots, v_n | v_1(t) = v_2(t) = \ldots = v_n(t)\}.$$

On perturbation from synchrony, the evolution of the coupled ensemble of grid-cells may return to synchrony (become spatially homogeneous) or remain unsynchronised (spatially patchy), depending on the dynamics of the individual grid-cells and the strength of coupling between them.

By analogy to the real world, where a plankton "patch" is a region of sea of homogeneous plankton biomass, we may consider a model plankton "patch" to be a synchronised subset of grid-cells C_k with $1 \leq k \leq n$. The system considered here - that of an ensemble of identically represented oscillators - is capable of exhibiting only two system-level stable states as the coupling strength is increased: complete asynchrony ($k = 1$) or complete synchrony ($k = n$). If the coupling strength is sufficient for synchrony then as soon as two adjacent oscillators become synchronised they are, since they are identically represented, locked into that state and thereafter act as one oscillator, leading eventually to synchrony of all oscillators. Alternative

set-ups, such as ensembles of non-identical oscillators (as explored in Chapter 3), allow stable dynamics with $1 < k < n$, a phenomenon referred to as *clustering* (Belykh et al., 2003), but for the system considered in this chapter we are only concerned with the fully synchronised state.

The stability of this fully synchronised state is established by calculating the largest *normal (or transverse) Lyapunov exponent* Λ; that is, the rate of growth of perturbations away from synchrony in the direction transverse to the synchronisation manifold.

We have a chain of n coupled plankton grid-cells $\mathbf{v_1}, \mathbf{v_2}, \ldots, \mathbf{v_n}$ and wish to determine the rate of expansion of a perturbation away from the synchronous state $\mathbf{v_1} = \mathbf{v_2} = \cdots = \mathbf{v_n}$, which resides on $\mathcal{M}_s$. To enable the separation of dynamics *on* and *normal* to $\mathcal{M}_s$, a change of variables from the set $\mathbf{v_1}, \mathbf{v_2}, \ldots, \mathbf{v_n}$ of grid-cells to an orthogonal set $\pi_1, \pi_2, \ldots, \pi_n$ is applied such that $\pi_2 = \pi_3 = \cdots = \pi_n = 0$ when the populations are synchronised, and π_1 represents the dynamics on the synchronous attractor; for example, as follows,

$$\begin{pmatrix} \pi_1 \\ \pi_2 \\ \vdots \\ \vdots \\ \pi_n \end{pmatrix} = \frac{1}{n} \begin{pmatrix} 1 & \cdots & \cdots & \cdots & 1 \\ 1 & \cdots & \cdots & 1 & -(n-1) \\ 1 & \cdots & 1 & -(n-2) & 0 \\ \vdots & & & & \vdots \\ 1 & -1 & \cdots & \cdots & 0 \end{pmatrix} \begin{pmatrix} \mathbf{v_1} \\ \mathbf{v_2} \\ \vdots \\ \vdots \\ \mathbf{v_n} \end{pmatrix}.$$

As with the calculation of Lyapunov exponents described above, a single uncoupled oscillator is initially integrated until transient behaviour dies and dynamics lie on the synchronisation manifold, with values π_0. For a reference trajectory $\mathbf{u} \epsilon \mathcal{M}_s$, we set

$$\mathbf{u} = (\pi_0, 0, \cdots, 0).$$

Since $\mathcal{M}_s$ is invariant, the reference trajectory $\mathbf{u}$ remains within $\mathcal{M}_s$ for all time. A test trajectory $\mathbf{w}$ is initiated by adding a small initial perturbation away from synchrony of magnitude d_0 ($\mathcal{O}(10^{-5})$) to trajectory $\mathbf{u}$ so that

$$\mathbf{w} = \mathbf{u} + (0, \frac{d_0}{\sqrt{n-1}}, \ldots, \frac{d_0}{\sqrt{n-1}}),$$

i.e. a perturbation normal to $\mathcal{M}_s$.

Both trajectories are integrated forward for a few time-steps and the extension $dS_\perp$ from synchrony normal to the synchronisation manifold relative to the original perturbation d_0 is given by

$$dS_\perp = \frac{\sqrt{\sum_{j=2}^{n}(\mathbf{w_j} - \mathbf{u_j})^2}}{d_0},$$

where $\mathbf{u_j}$ and $\mathbf{v_j}$ are the j^{th} components of the reference and test trajectories at time t, respectively. The finite-time transverse Lyapunov exponent at iteration step i is then

$$\Lambda_i = \frac{\Lambda_{i-1}t_{i-1} + \log(dS_\perp)}{t_i},$$

measuring the stretch *in the direction transverse to synchrony* of the initial perturbation with time.

The process is repeated until convergence of Λ is achieved. However, as with the calculation of λ described above, in the case of chaotic orbits the separation quickly becomes too large for us to be considering *nearby* trajectories. Again, a rescaling must be applied to avoid this problem.

If $\Lambda < 0$ then the synchronous state is stable since perturbations from synchrony will decay. This is a threshold phenomenon; it depends upon the magnitude of coupling and there exists a critical strength of coupling above which synchrony will re-establish itself after perturbation. In other words, there exists critical coupling $\varepsilon = \varepsilon_c$ such that $\Lambda(\varepsilon_c) = 0$.

2.2.4 Bounding the critical coupling in parameter space

The critical coupling strength ε_c required for stable synchrony of a system of generic nearest-neighbour coupled identical oscillators was shown by Fujisaka and Yamada (1983) to be directly proportional to the largest Lyapunov exponent λ of the dynamics of an individual isolated oscillator. Applying this to the plankton ecosystem models considered here, therefore, in order to place an upper bound on ε_c for each model, it is required to find where λ attains its maximum within the reported range of biological parameters. Since $\lambda = 0$ in non-chaotic regions of parameter space, $\varepsilon_c = 0$, and therefore a coupled system of non-chaotic identical oscillators will always stably synchronise. We therefore only need consider *chaotic* regions of

parameter space, identified by $\lambda > 0$, and look for the "most chaotic" point, i.e. where λ attains its maximum.

An iterative method is used to approximate of the maximum value of λ as a function of the biological model parameters. Each biological model has a set $\Omega = \{a_1, a_2, \ldots, a_l\}$ of l parameters. Since $\lambda = 0$ for steady-state and limit cycle dynamics, we need only consider chaotic regions. We initiate the algorithm at a point $\mathbf{a}(0) = (a_1(0), a_2(0), \ldots, a_l(0)) \in \Omega$ for which the model exhibits chaos. Such a point is known to exist for SH81 from the work of Edwards and Brindley (1999). For HP91 chaotic regions are clearly demonstrated in the original paper.

For each parameter a_j, we have a biologically-plausible range $[a_{j_{min}}, a_{j_{\max}}]$ (see Table 1), giving an l-dimensional hypercube bounded by the $a_{j_{min}}$ and $a_{j_{\max}}$, for $j = 1, \ldots, l$, containing the initial point $\mathbf{a}(0)$. For each step i of the iteration, and for each parameter a_j of the set in turn, λ is calculated with parameters $a_k(i)$, $k < j$, and $a_k(i-1)$, $k > j$, fixed and parameter a_j varied across the range $[a_{j_{min}}, a_{j_{\max}}]$. The value of $a_j(i)$ is then set as the value within $[a_{j_{min}}, a_{j_{\max}}]$ giving maximum λ. This is repeated for all parameters a_j, giving a new parameter set $\mathbf{a}(i)$. If inspection of these "slices" across parameter space indicates that

$$\begin{array}{rl} & \max_{a_1 \epsilon \left[a_{1_{min}}, a_{1_{\max}}\right]} \lambda\left(a_1, a_2(i), a_3(i), \ldots, a_l(i)\right) \\ \approx & \max_{a_2 \epsilon \left[a_{2_{min}}, a_{2_{\max}}\right]} \lambda\left(a_1(i), a_2, a_3(i), \ldots, a_l(i)\right) \\ \vdots & \\ \approx & \max_{a_l \epsilon \left[a_{l_{min}}, a_{l_{\max}}\right]} \lambda\left(a_1(i), a_2(i), a_3(i), \ldots, a_l\right) \end{array},$$

to within a specified level of accuracy then the parameter values giving the approximate maximum λ are judged to have been found (see Figure 2.3 and Table 1). Otherwise, the process is repeated for step $i + 1$.

It is possible that the approximate method detailed here may miss the chaotic apex of a model. For example, a disconnected region of chaotic parameter space may exist that does not intersect with the parameter "slices" through the initial chaotic point. No such isolated chaotic regions were found during investigation of the models using the dynamical systems package AUTO. An exhaustive search of the l-dimensional parameter space of the models considered here would be extremely computationally expensive. The method is therefore considered a good necessary

approximation for the most chaotic point within biologically acceptable bounds. Of course, the global apex for the model may lie outside these bounds.

2.3 Results

2.3.1 Single grid-cell

The iterative method described above was used to find the region of parameter space giving the maximum largest Lyapunov exponent λ for each model. As an example, Figure 2.3 shows how λ varies as a function of herbivorous zooplankton growth efficiency across 'slices' of parameter space for all three models; all other parameters are kept constant at the established λ apex. Because $\lambda > 0$ only where dynamics are chaotic, Figure 2.3 shows calculations only across the chaotic regions of parameter space. However, since this a necessarily finite-time calculated approximation of an quantity defined for infinite-time, the exponent does not quite go to 0 in the limit-cycle and steady-state regions. Chaotic ranges established in this way for all other model parameters are included in Table 2.1. The global chaotic apex for the model HP91 lies outside but close to the suggested parameter ranges. For this reason, we consider two apices for this model: the points in parameter space giving maximum λ *inside* and *outside* suggested ranges respectively.

$\lambda_{\max}$ (denoted by dotted lines in Figure 2.3) is approximately 0.0063 d^{-1} and 0.01 d^{-1} for models SH81 and SH81b respectively. Constrained to suggested parameter ranges, HP91 has apex 0.011 d^{-1}; $\lambda_{\max}$ reaches 0.013 d^{-1} if parameters are allowed to vary beyond these ranges. Model dynamics at these points in parameter space, both as a time series and in phase space, are shown in Figure 2.4 and the corresponding parameter values are given in Table 2.2. Figure 2.4 shows the ecosystem components to oscillate with a roughly 50 day period The particular period of oscillation is not important in the context of this investigation, for which we have not attempted to model the seasonal cycle or tune the model to a particular ocean region. Although it may impact quantitatively upon the results, the qualitative results relating to the ability of a system of plankton populations to stably synchronise are unchanged.

2.3.2 Two-patch stability

Figure 2.5 shows the calculated transverse Lyapunov exponent, Λ, for a two grid-cell coupled system as a function of varying strength of coupling ε for each model. The coupling strength at which $\Lambda(\epsilon)$ changes from positive (perturbations from synchrony grow) to negative (such perturbations decay) is the critical coupling strength ε_c required for stable synchrony. ε_c is seen to equal 0.0031 d^{-1}, 0.0051 d^{-1}, 0.0061 d^{-1} and 0.0056 d^{-1} for models SH81, SH81b, HP91 (outside) and HP91 (inside), respectively. Since theory (Fujisaka and Yamada, 1983) shows that ε_c is directly proportional to λ for this type of coupling, and we have established $\lambda_{\max}$ within biologically-acceptable parameter space, $\varepsilon_c(\lambda_{\max})$ gives an upper bound on ε_c for each model: a coupling strength of $\varepsilon > \varepsilon_c(\lambda_{\max})$ is sufficient to stably synchronise the two-grid-cell coupled system for any set of biological parameter values.

As an example, using the model SH81, Figure 2.6 shows how system dynamics differ below and above this 'blowout bifurcation' (as the parameter ε moves below the critical point, the stability of the synchronous state is 'blown out'). We initiate the integration with the two coupled patches out of synchrony with one another, so that $|\mathbf{v_1} - \mathbf{v_2}| = \delta > 0$ where δ is a small perturbation from synchrony. In Figure 2.6, the evolution of this perturbation, for the phytoplankton components P_1 and P_2 of the two patches, is plotted with time for a coupling strength of $\varepsilon < \varepsilon_c$ (top) and $\varepsilon > \varepsilon_c$ (bottom). It is seen that a coupling strength of 0.0025 d^{-1}, which is below ε_c, is insufficient to restore synchrony, so that the system starts to display heterogeneous dynamics. A coupling of 0.0035 d^{-1} is strong enough to draw the oscillators back into synchrony. These two illustrative values of $\varepsilon = 0.0025$ and $\varepsilon = 0.0035$ have been chosen sufficiently distant from the critical coupling of $\varepsilon_c = 0.0031$ to give clear examples; for ε just less than ε_c, dynamics may remain near to synchrony for long periods of time although the state is unstable and, conversely, dynamics may take a very long time to reach synchrony or may intermittently burst away for ε just greater than ε_c.

The results in Figure 2.5 fit well with the predictions of Fujisaka and Yamada (1983). For a two-grid-cell system, the theory states that $\varepsilon_c = \frac{\lambda}{2}$. Using calculated λ, this gives predicted critical coupling strengths of 0.0032 d^{-1}, 0.0048 d^{-1}, 0.0065 d^{-1}

and 0.0055 d^{-1} for models SH81, SH81b, HP91 (outside) and HP91 (inside) respectively. For comparison, the directly calculated results are 0.0031 d^{-1}, 0.0051 d^{-1}, 0.0061 d^{-1} and 0.0056 d^{-1}, respectively. Figure 2.7 gives an example of how well the empirical and theoretical results match for a cross section through parameter space; for model SH81, model-calculated ε_c is plotted along with $\frac{\lambda}{2}$ for the phytoplankton growth rate parameter a varied across the chaotic window of parameter space, keeping all other parameters at λ apex values. This clearly illustrates the dependence of the critical coupling strength upon the parameter values, and therefore dynamics, of the isolated model in an individual grid-cell.

2.3.3 n-patch stability

Next considered was a chain of n coupled grid-cells, for $n = 2, \ldots, 10$, with nearest-neighbour coupling and the biology in each patch represented by the SH81 model. ε_c was established as a function of n: first, by direct computation of $\Lambda(\varepsilon)$ and, second, by using the calculated values of $\lambda_{\max}$ to apply the theory of Fujisaka and Yamada (1983).

Figure 2.9 shows the results of directly computing Λ as a function of ε for example cases of $n = 5$ and $n = 10$. The results of computed and theoretically estimated $\varepsilon_c(n)$ are plotted in Figure 2.8. It is seen that the critical coupling strength increases with the length of the chain, so that a greater strength of mixing between patches is needed to synchronise a chain with more patches. Additionally, we see that the theory of Fujisaka and Yamada (1983), which states that the critical coupling strength is related to chain length and largest Lyapunov exponent λ of the single-patch biological model as

$$\varepsilon_c = \frac{\lambda}{\min_{k=1,\ldots,n-1}\left(4\sin^2\left(\frac{k\pi}{2n}\right)\right)} \tag{2.7}$$

agrees well with the computed values. The slight discrepancies between the two sets of results result from the numerical error involved in calculating a finite-time approximation of both Lyapunov exponents and normal Lyapunov exponents.

It is evident that a prediction of ε_c for a system of this type with any number of grid-cells may be inferred from knowledge of the Lyapunov exponent of the isolated

biological model in any one grid-cell.

Although n-patch results have been presented here for a chain of patches each represented by the SH81 model, similar results are obtained with the other biological models considered.

2.4 Discussion

To address the question of how grid-cell biology and the number of grid-cells impact upon the behaviour of coupled biophysical simulations, we applied the methods of synchronisation theory to an ensemble of identically-represented interacting plankton populations. Using several different typical plankton ecosystem models to represent the evolution of each patch, and varying the number of patches comprising the ensemble, we calculated the critical strength of patch-to-patch coupling required for stably synchronous dynamics to occur. The study focused on chaotic regions of parameter space since identical steady-state and limit cycle oscillators always stably synchronise.

2.4.1 Critical coupling strength for synchrony

For a chain of n coupled plankton grid-cells, each represented by the same biological model, the strength of coupling ε_c required for stably homogeneous (synchronised) dynamics to occur is found to vary as a function of biological model, model parameters and n, the latter bearing out the theory of Fujisaka and Yamada (1983) as expressed in Equation 2.7.

We see that the critical coupling strength varies linearly with λ, implying that the use of "more chaotic" biological dynamics at grid-cell level reduces the ability of the chain to exhibit homogeneous dynamics. More significantly, ε_c increases with n. In other words, a stronger mixing between grid-cells is required to synchronise a longer chain.

The relationship between ε_c and n can be simplified as follows. As n becomes large, $\frac{\pi}{2n}$ becomes small and, therefore,

$$\varepsilon_c \approx \frac{\lambda n^2}{\pi^2} \tag{2.8}$$

(because $\sin(x) \approx x$ for small x) so that the critical coupling increases as n^2.

This has implications for modelling studies. Suppose we wish to model the dynamics of a particular transect of ocean of length L, perhaps to compare the results with observed data. For the purposes of simulation, the transect is divided into a number of grid-cells, depending on various factors such as available computing power and the spatial resolution of the observed data. A plankton ecosystem model is chosen to describe the biology in each grid-cell. To simulate the physical flow, we impose a fixed, effectively diffusive, coupling of strength ε between grid-cells. Since $\varepsilon_c \propto \frac{\lambda n^2}{\pi^2}$, we know that, for a fixed ε and fixed biological model, there exists a corresponding critical number of grid-cells n_c such that the use of a number of grid-cells $n > n_c$ to divide up the transect L will lead to unsynchronised dynamics. Therefore, the spatial resolution chosen for the simulation of a particular region of ocean could drastically alter the results in a discontinuous manner, as it sets the number of grid-cells used.

As explained, this threshold phenomenon occurs only when the individual grid-cell dynamics are *chaotic*. That an ensemble of identical chaotic oscillators may have emergent characteristics that bifurcate in this manner is a case against using chaotic plankton ecosystem models in a system like this to study plankton patchiness. Chaotic ecosystem models should be used with caution to guard against spurious or misleading emergent features. Since the extent of chaotic regions of parameter space has not been determined for plankton models, this is an important result which is worrying in the light of recent findings by Gross et al. (2006) that chaotic parameter ranges exist generically in food chain models of greater than three components. For SH81, the parameter space appears to contain only relatively small chaotic regions, so that that the effect may be of minor concern, whereas HP91 is an example of a model containing interspersed windows of chaotic and periodic behaviour throughout its parameter space (as illustrated by Caswell and Neubert (1998) and see also Figure 2.3), which in the context of the results of this study might make it unsuitable for use in a coupled biophysical model.

More generally, the results illustrate that the choice of biological model at grid-cell level can have a significant impact at system level. It is noteworthy that SH81b,

although differing from SH81 only by a small change of functional form and having similar parameter values and almost identical structure, exhibits chaos over smaller sized regions of parameter space yet attains a larger "degree of chaos", as measured by a greater $\lambda_{\max}$ (Figure 2.3), which in turn reduces the ability of coupled SH81b oscillators to synchronise (Figure 2.5). Why the small change in functional form should make a large difference and whether this is of biological significance is not known and would, since the models represent distinct biological scenarios, be a valid line of future enquiry. HP91, despite differing greatly in structure from SH81, has a similar $\lambda_{\max}$ and therefore synchronising ability. For all three models, λ, and therefore ε_c, varies greatly across parameter space. We conclude from this that choice of biological model and parameter set strongly affects the system-level dynamics.

2.4.2 Critical spatial scale for plankton patchiness

In their study of synchronisation in ensembles of plankton populations, Hillary and Bees (2004a) used the empirical relationship between spatial scale l and effective diffusivity $D(l)$ (Okubo, 1971) to relate the critical coupling strength ε_c to an emergent critical length-scale for patchiness in plankton. The observations of Okubo show that for $D(l)$ in $cm^2\ s^{-1}$ and l in cm

$$D(l) \approx 0.01 l^{1.15}.$$

Hillary and Bees (2004a) consider a chain of length L consisting of n coupled grid-cells, giving a grid-cell length-scale $\Delta = \frac{L}{n}$. They then equate the diffusive coupling ε with diffusive processes between grid-cells, so that $\varepsilon(l) \approx \frac{D(l)}{\Delta^2}$ where $\frac{1}{\Delta^2}$ approximates the second order spatial derivative. Using the relationship of Okubo, and taking l as the patch length-scale this gives

$$\varepsilon \approx 0.01 \left(\frac{\Delta}{100 \times 1000} \right)^{-0.85} \times 24 \times 60 \times 60$$

for ε in d^{-1}.

For their eight-grid-cell system, Hillary and Bees (2004a) found a critical coupling strength of 0.0075 d^{-1}. Using the relationship above, they equated this with a grid-cell length-scale of order 10 km, resulting in a critical domain length-scale L_c of

around 100 km at which synchronisation persists. Since with increasing length-scale the diffusivity according to the Okubo relationship increases and the appropriate coupling strength decreases, an eight-grid-cell system of length $L > L_c$ will have a diffusivity-related coupling strength $\varepsilon < \varepsilon_c$ and unsynchronised dynamics will result. L_c therefore represents a upper bound on the scale at which we expect to see synchronised patches for a fixed number of grid-cells.

However, we have seen in this study that $\varepsilon_c \propto n^2$ and from the above we know $\varepsilon \propto L^{-0.85} n^{0.85}$, so we have a relationship between the number of grid-cells and the critical length-scale:

$$L_c{}^{-0.85} \propto n^{1.15}.$$

Hence, as Hillary and Bees (2004a) in fact predict, the critical length-scale found using this method is a function of the number of grid-cells, and therefore resolution, of the simulation. As discussed above, the model resolution may be dependent upon such arbitrary factors as available computing power. Although we can establish a critical length-scale for a given number of grid-cells to stably synchronise, in many cases this relationship can therefore tell us little about the scale at which plankton patches should synchronise, because only the number of grid-cells into which a study region is partitioned, and not the true length-scale, has an effect on whether synchronisation will occur.

The above discussion depends upon assumptions about the length-scale taken in the approximation of the effective diffusivity. Since, in the work by Okubo (1971), the length-scale is arbitrarily set to a value such that a circle of that radius would contain 95% of the dye material, our patch length-scale Δ as used here is a natural choice. However, we expect in the case of synchronisation for information to diffuse over the full system, so that some may argue for the system length-scale to be L or an intermediate value. If we set $l = L$, we obtain

$$\varepsilon \approx 0.01 n^2 L^{-0.85}$$

so that, upon application of Equation 2.8, the n^2 terms cancel to give a constant L_c.

Additionally, care must be taken with our treatment of Equation 2.7, where we have taken n to be large. For a fixed system length-scale L, increasing n leads to

decreasing Δ. The Okubo (1971) paper deals with a closed range of spatial scales from 30 m to 100 km of spatial scales, so that we may reach a value of Δ for which this relationship is not valid.

2.4.3 Impact on biophysical modelling

To illustrate the impact of these results on physical quantities that may be derived from biophysical models, we examined the effect of synchrony on total primary production (TPP), a quantity frequently estimated from such models. For the example case of a ten-grid-cell chain of SH81 oscillators with parameter values set at the chaotic apex, we calculated TPP(t) as the sum of the phytoplankton growth rates for (i) a coupling strength of $\varepsilon = 0$ (representing, for non-identical initial conditions, the "most asynchronous" state achievable) and (ii) $\varepsilon > \varepsilon_c$.

TPP(t) for (i) and (ii) is shown in Figure 2.10. As a function of time, it was found that synchrony increased and decreased the values of TPP attained at maxima and minima, respectively - an effect caused by the additive effect of the concurrent nature of these events in the synchronous case: maximum and minimum TPP were for (i) 0.84 gC m^{-3} d^{-1} and 1.03 gC m^{-3} d^{-1} and for (ii) 0.67 gC m^{-3} d^{-1} and 1.29 gC m^{-3} d^{-1} (to 2 d.p.). The mean TPP, however, was equal to 0.92 gC m^{-3} d^{-1} for both (i) and (ii).

The results, whilst only qualitative in nature as we are not modelling the seasonal cycle, indicate the need for directing major effort into the understanding of biophysical models. Otherwise, our confidence in the bulk properties derived from them will be diminished.

Figure 2.1: Schematic of the Nutrient-Phytoplankton-Zooplankton model of Steele and Henderson (1981) with arrows indicating flow of material between ecosystem components.

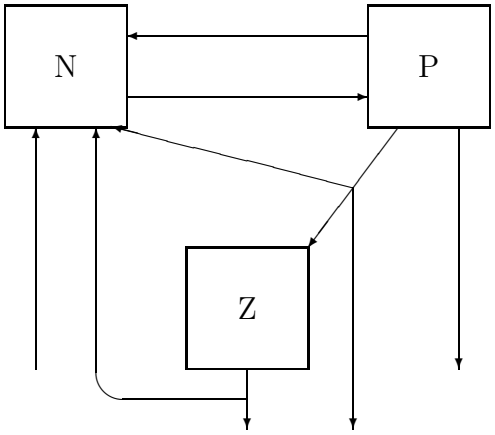

Figure 2.2: Schematic of the Phytoplankton-Herbivore-Carnivore model of Hastings and Powell (1991) with arrows indicating flow of material between ecosystem components.

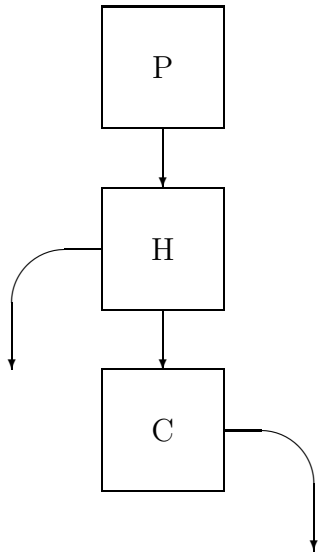

Figure 2.3: **Parameter space.** Largest Lyapunov exponent λ in d^{-1} calculated across the chaotic windows for herbivorous zooplankton growth efficiency parameters α (*SH81 in black; SH81b in red*) and c_1 (HP91). All other parameters are held at those giving maximum largest Lyapunov exponent λ. *Dotted* lines indicate the parameter values giving $\lambda_{\max}$. The calculations are shown only across the chaotic regions of parameter space, since $\lambda = 0$ for equilibrium and limit cycle regions.

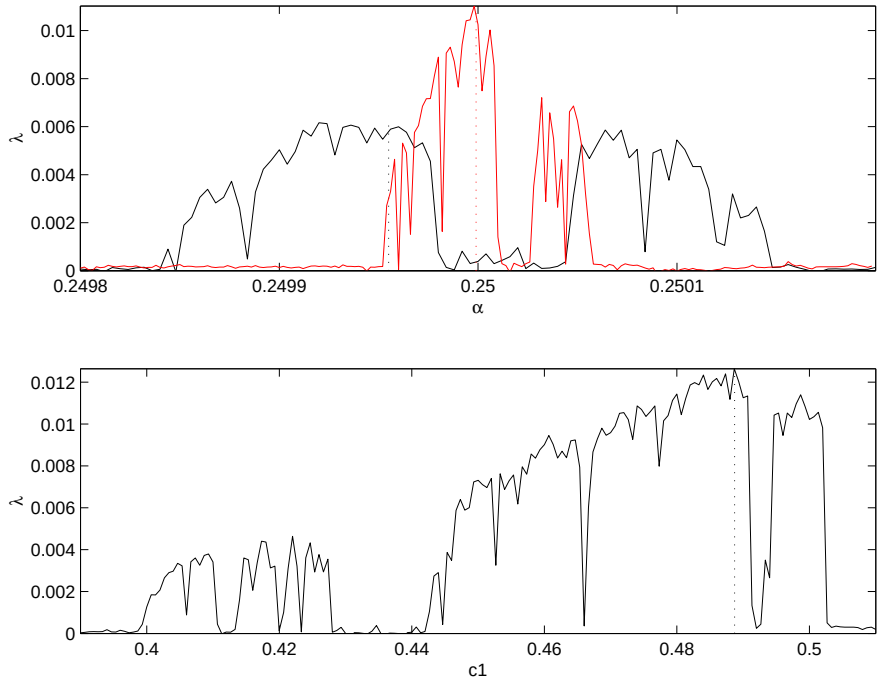

Figure 2.4: **Model dynamics.** Phase space attractors and temporal evolution in days of state variables in units of gC m^{-3} d^{-1} for SH81 (*left*), SH81b (*middle*) and HP91 (*right*). Parameter values are set to those giving maximum largest Lyapunov exponent λ in d^{-1}. Transient dynamics not shown. *Key: blue - nutrients, green - phytoplankton, black - herbivorous zooplankton, red - carnivorous zooplankton.*

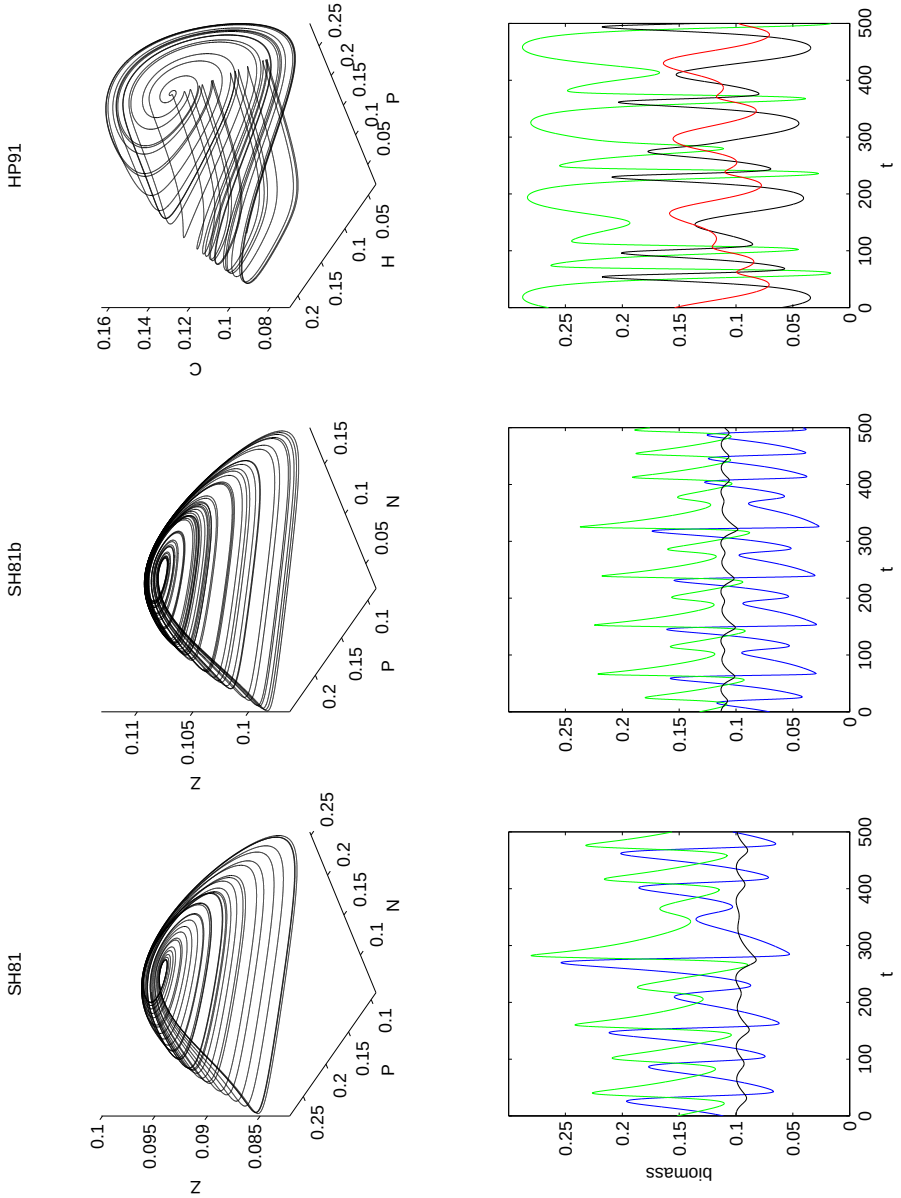

Figure 2.5: **Critical coupling strength.** Calculated largest normal Lyapunov exponent Λ in d^{-1} as a function of coupling strength ε in d^{-1} for models SH81 (*black*), SH81b (*red*), HP91 restricted to suggested parameter ranges (*blue*) and HP91 not restricted to suggested parameter ranges (*green*). Model parameters are set at values giving maximum largest Lyapunov exponent λ in d^{-1}. The critical coupling strength ε_c is indicated by the value of ε giving $\Lambda(\varepsilon) = 0$.

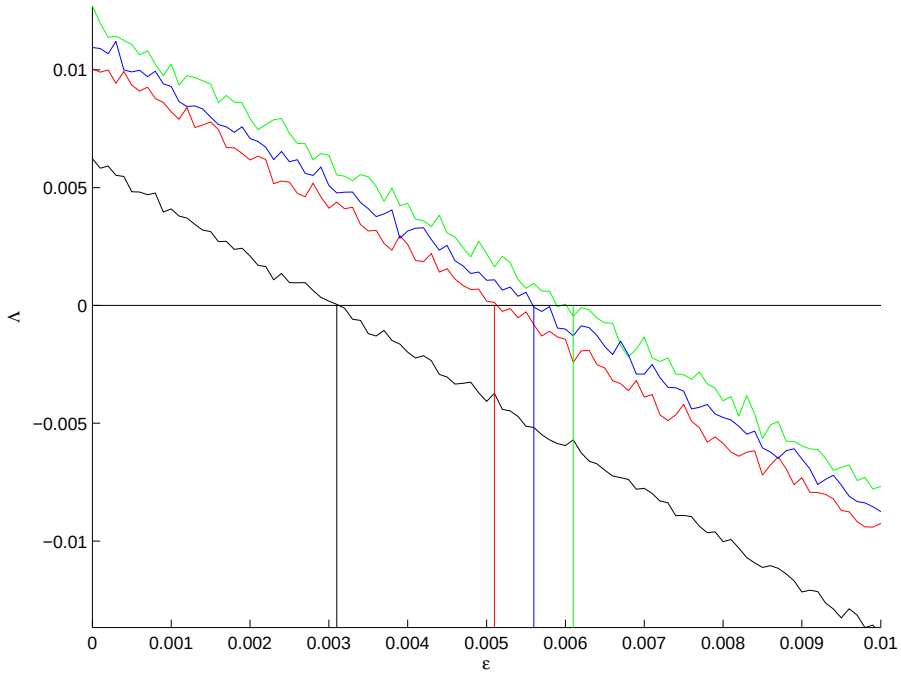

Figure 2.6: **Two-patch dynamics.** Time evolution in days of the difference between phytoplankton components P_1 and P_2 in gC m^{-3} plotted for coupling strength $\varepsilon = 0.0025$ d^{-1} ($< \varepsilon_c$) and $\varepsilon = 0.0035$ d^{-1} ($> \varepsilon_c$) in the top and bottom panels respectively. Model used is SH81 and parameters are set at values giving maximum largest Lyapunov exponent λ.

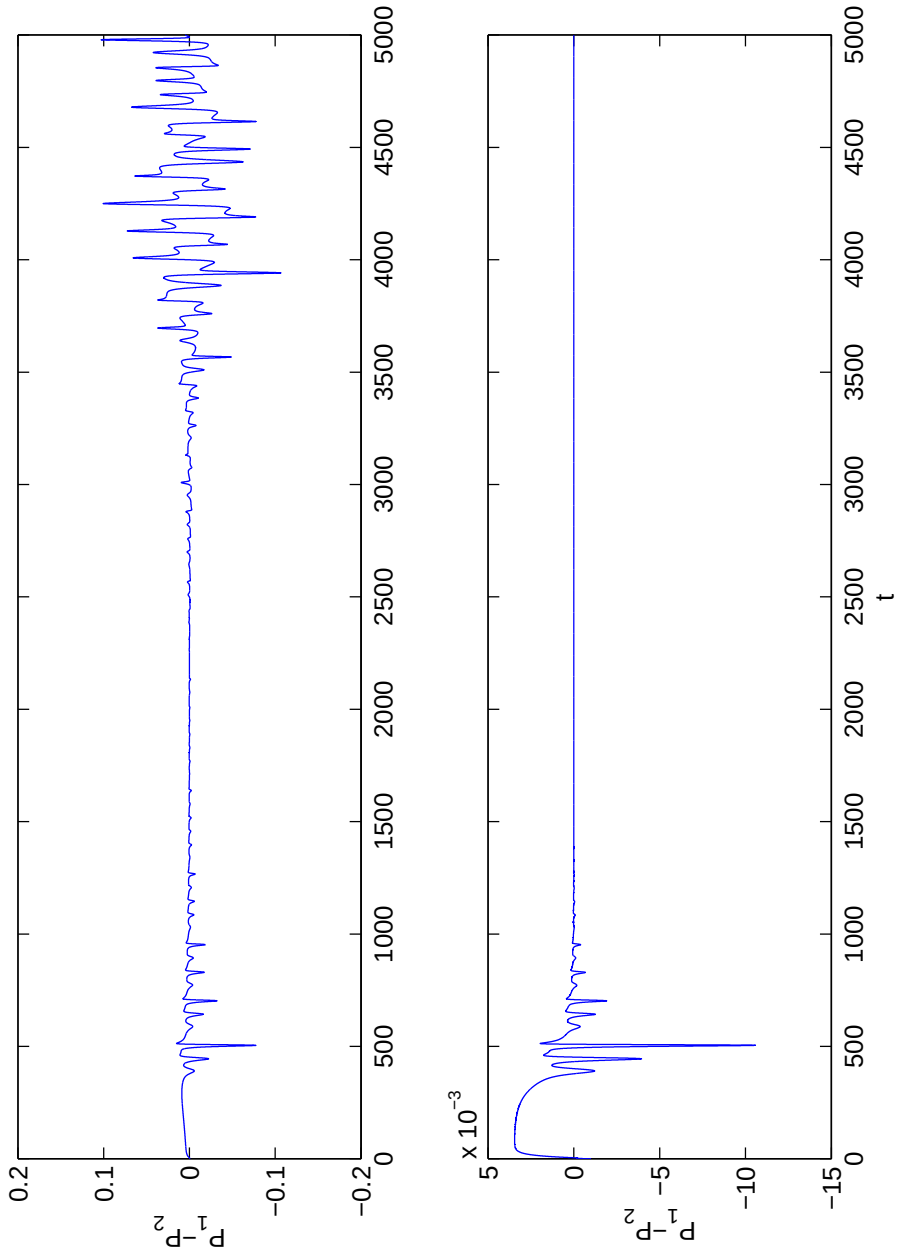

Figure 2.7: **Comparison with theory of Fujisaka and Yamada (1983)**. Critical coupling strength ε_c in d^{-1} plotted across chaotic window for model SH81 phytoplankton growth parameter a in $\mathrm{m}^{-1}\ \mathrm{d}^{-1}$. *Solid line* shows directly calculated ε_c values and *dotted line* shows predicted ε_c according to the theory of Fujisaka and Yamada (1983), i.e. half largest Lypaunov exponent λ.

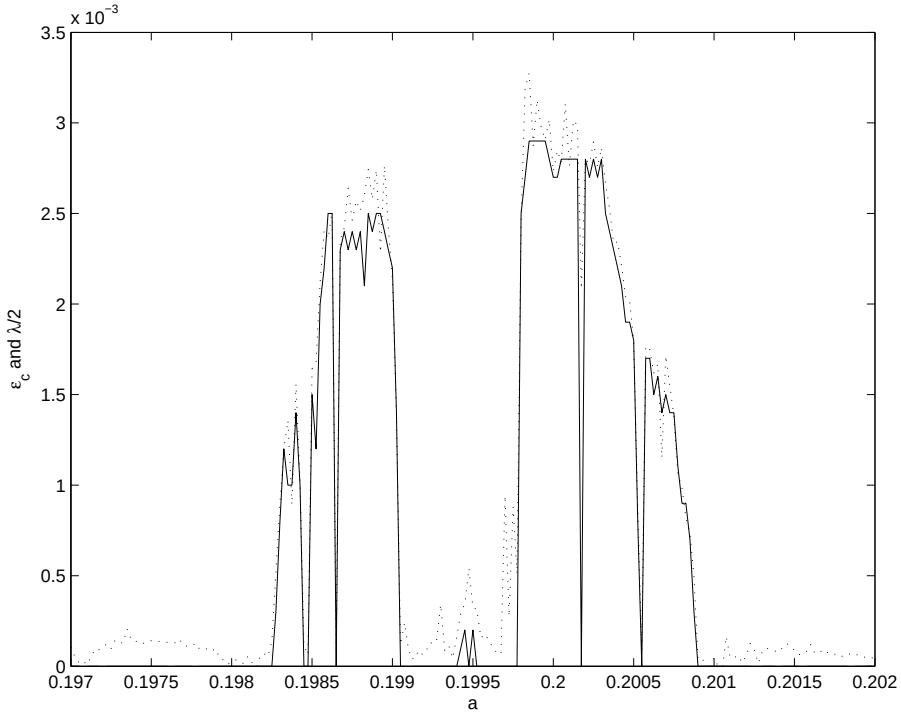

Figure 2.8: **n-patch chain.** Critical coupling strength ε_c in d^{-1} as a function of number of grid-cells n. Plankton dynamics in each grid-cell are represented by SH81 model and the chain has fixed-ends. *Crosses* indicate Λ in d^{-1} as predicted by Fujisaka and Yamada (1983). *Circles* indicate experimental results for 2 to 10-patch chains.

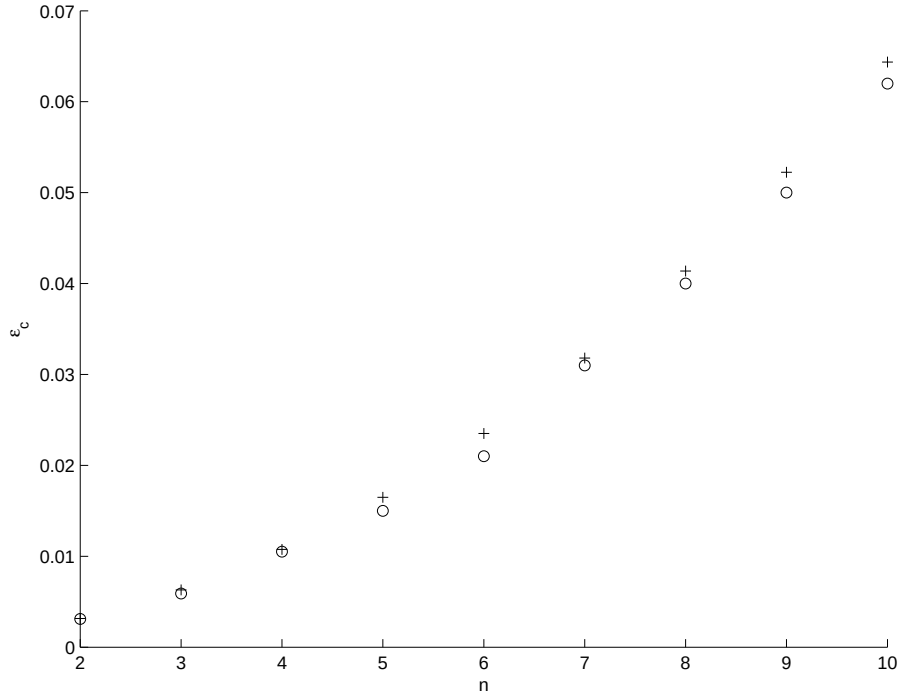

Figure 2.9: **Critical coupling strength.** Calculated largest normal Lyapunov exponent Λ in d^{-1} as a function of coupling strength ε in d^{-1} for a 5-patch (*dotted*) and 10-patch chain (*solid*) of NPZ oscillators represented by SH81 (see text). Biological model parameters are set at values giving maximum largest Lyapunov exponent λ. The critical coupling strength for stable synchrony is indicated by $\Lambda(\varepsilon) = 0$.

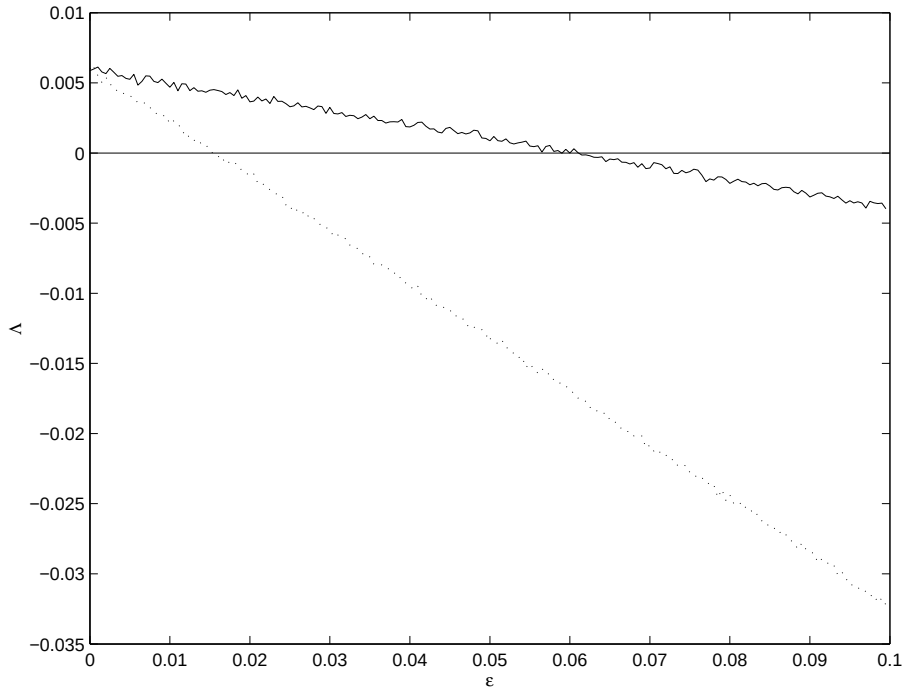

Figure 2.10: **Bulk properties.** Time evolution in days of total primary production (TPP) in gC m^{-3} d^{-1} for a ten grid-cell chain of SH81 oscillators for coupling strength $\varepsilon = 0$ d^{-1} (*red*) and $\varepsilon > \varepsilon_c$ (*blue*).

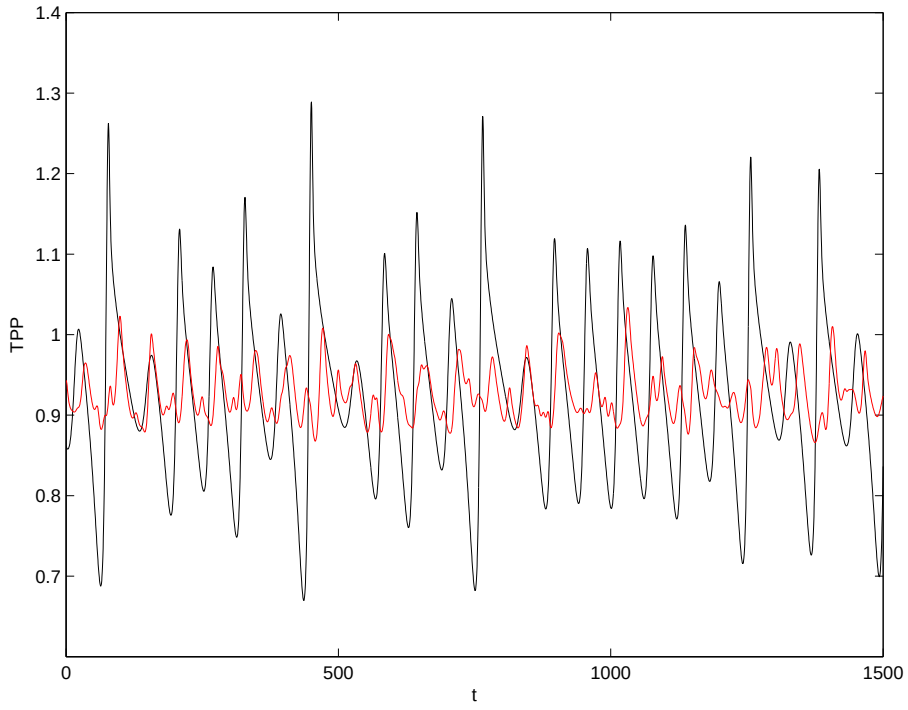

Parameter	Symbol SH81	HP91	Reported range	Chaotic window SH81	SH81b	HP91	Units
P growth parameter	a		0.1-0.6	0.198-0.201	0.199-0.201		$m^{-1}\ d^{-1}$
P growth rate		$R \equiv \frac{a}{b}$	0.1-0.6			0.7-3.75	d^{-1}
Light attenuation by water	b		0.04-0.2	0.199-0.203	0.1995-0.2005		m^{-1}
Self-shading by P	c		0.3-1.2	0.37-0.43			$m^2\ gC^{-1}$
P carrying capacity		$K \equiv \frac{2b}{c}$	0.04-0.2			0.28-0.32	$gC\ m^{-1}$
Herbivorous Z mortality	d		0.015-0.15	0.1418-0.1421	0.1401-0.1402		d^{-1}
		d_1	0.015-0.15			0.09-0.125	d^{-1}
Carnivorous Z mortality		d_2	0.015-0.15			0-0.05	d^{-1}
N half-saturation constant	e		0.02-0.15	0.027-0.04	0.0295-0.0305		$gC\ m^{-3}$
Exchange rate with lower layer	k		0.0008-0.13	0.0499-0.0506	0.0498-0.0502		d^{-1}
P respiration	r		0.05-0.15	0.143-0.157	0.148-0.153		d^{-1}
P sinking	s		0.032-0.08	0.038-0.043	0.039-0.041		d^{-1}
Lower layer N concentration	N_0		0.1-2.0	0.998-1.01	0.998-1.002		$gC\ m^{-3}$
Herbivorous Z assimilation efficiency	α		0.2-0.75	0.2498-0.2502	0.2499-0.2501		
		c_1				0.39-0.51	
Carnivorous Z growth efficiency		c_2	0.2-0.75			0.4-0.65	
Z excretion fraction	β		0.25-0.8	0.325-0.335	0.328-0.332		
Remineralisation of Z excretion	γ		0.5-0.9	0.49-0.54	0.495-0.507		
Herbivorous Z grazing rate	ζ		0.6-1.4	0.5995-0.6003	0.5998-0.6002		d^{-1}
		a_1	0.6-1.4			0.48-0.72	d^{-1}
Carnivorous Z grazing rate		a_2	0.6-1.4			0.3-0.75	d^{-1}
Herbivorous Z grazing half-sat. const.	μ		0.02-0.1	0.0347-0.0351	0.0349-0.0351		$gC\ m^{-3}$
		b_1	0.02-0.1			0.08-0.11	$gC\ m^{-3}$
Carnivorous Z grazing half-sat. const.		b_2	0.02-0.1			0.01-0.16	$gC\ m^{-3}$

Table 2.1: **Biological Model Parameters.** Ranges are taken from Edwards and Brindley (1996), wherein values from various studies are collated.

SH81	SH81b	HP91 (inside)	HP91 (outside)
$a = 0.19994$	$a = 0.2$	$k = 0.3058$	$k = 0.31$
$b = 0.200267$	$b = 0.2$	$r = 0.748$	$r = 0.908$
$c = 0.394733$		$a_1 = 0.672$	$a_1 = 0.712$
$d = 0.142012$	$d = 0.140136$	$a_2 = 0.6$	$a_2 = 0.3$
$e = 0.03137$	$e = 0.03004$	$b_1 = 0.1$	$b_1 = 0.0881$
$k = 0.050132$	$k = 0.05$	$b_2 = 0.1$	$b_2 = 0.1528$
$r = 0.1483$	$r = 0.15$	$c_1 = 0.5$	$c_1 = 0.488$
$s = 0.04072$	$s = 0.03997$	$c_2 = 0.225$	$c_2 = 0.424$
$N0 = 1.00236$	$N0 = 1.0$	$d_1 = 0.104$	$d_1 = 0.096$
$\alpha = 0.249956$	$\alpha = 0.25$	$d_2 = 0.055$	$d_2 = 0.049$
$\beta = 0.32894$	$\beta = 0.33$		
$\gamma = 0.50675$	$\gamma = 0.5$		
$\zeta = 0.59982$	$\zeta = 0.6$		
$\mu = 0.0349475$	$\mu = 0.035$		

Table 2.2: **Chaotic apex.** Parameter values giving maximum largest Lyapunov exponent $\lambda_{\max}$ for each biological model. Parameter units are as in Table 2.1.

Chapter 3

Non-identical oscillators.

3.1 Introduction

In the previous section, a plankton distribution was modelled as an interacting ensemble of identically-represented plankton populations. That is, the biological model equations and parameter values were the same for each population. This makes the assumption that the dynamics are spatially uniform, so that the same set of parameter values represents the plankton population dynamics equally well across the whole of the area of interest. In reality, spatial variation is inherent in nature, so that the most appropriate set of biological model parameters to use in the representation of each population may vary in space. For example, if temperature or mixed layer depth are likely to vary across the modelling domain, then any biological parameter which is related to these physical parameters is likely also to vary (see Section 1.2).

Consequently, although a useful mathematical simplification, it is not entirely realistic to model a metapopulation using an identical representation for each individual population. By introducing some mismatch into the dynamical representation of each population, it is possible to model a spatially varying distribution more representative of the real world. This mismatch may be introduced by using the same biological model for each population but allowing variation in the biological model parameter set. As a result of parameter mismatch, each oscillator is slightly different in terms of its natural frequency and amplitude of oscillation so that it is now im-

possible to achieve a stable fully synchronised state. The synchronisation manifold, as defined in the previous chapter, is no longer invariant. However, a much richer array of approximate or *generalised* synchronous behaviour (see Pikovsky et al., 2001) is now possible where population dynamics are related by a one-to-one mapping. Generalised synchronisation encompasses a variety of behaviour observed in theoretical and real-world systems. Here we briefly describe some relevant synchronous behaviour possible in systems of non-identical oscillators.

Whereas in Chapter 2 the ensemble of plankton populations was observed to fully synchronise for a sufficient strength of interaction, systems of non-identical oscillators have been shown to exhibit an intermediate state of *cluster synchronisation* (Belykh et al., 2003) - the system breaks up into synchronised subsets of populations with no synchrony between clusters. The type of clustering, e.g. size, number, shape and positioning of synchronised subsets, has been seen to vary with a number of factors, including the size of the parameter mismatch (Belykh et al., 2003), the type (Belykh et al., 2003) and strength (Osipov and Sushchik, 1997) of coupling and the spatial arrangement of the natural (independent) frequencies (Osipov and Sushchik, 1997). Clustering states may emerge as an intermediate state between asynchrony and (almost) full synchrony. Osipov and Sushchik (1997) found that transitions between clustering states as the strength of interaction is varied may be "soft" - a gradual continuous enlargening and merging of clustering with increasing coupling strength - or "hard" - an arrangement of clusters persists with increasing coupling until altering suddenly at a sharp transition value of coupling strength.

For particular conditions, the strength of coupling may be sufficient to approximately synchronise the full system. This synchrony may take the form of *frequency locking*, where the natural frequency disorder is overcome to pull the populations towards a common frequency of oscillation (e.g. Rosenblum et al., 1997). There may still exist a constant phase difference between frequency-locked populations, a phenomenon referred to as *lag synchrony* (Rosenblum et al., 1997; Taherion and Lai, 1999).

Counter-intuitively, an increase in the strength of coupling may not lead to a monotonic increase in the synchrony between populations. For a system of non-

identical food-web oscillators, Blasius and Montbrió (2003) found that in some cases increased coupling was first able to increase the amount of frequency disorder before larger coupling was able to draw the system into synchrony. This coupling-induced desynchronisation or *anomalous synchronisation* (referring to the eventual synchronisation of the system) was shown to be caused by non-isochronicity or shear of phase flow around the oscillator attractors; the interaction has the effect of constantly pulling the populations away from their natural attractors, and if the rate of shear is affected by both the natural frequency of the oscillator and the strength of the coupling then the ability of the system to synchronise is enhanced or disrupted, depending on the nature of the relationship between the non-isochrony and coupling.

The ability to synchronise, and the kind of synchronous behaviour observed, are influenced by a number of factors. We have already seen in Chapter 2 that the ability to synchronise is dependent on the number of populations, their dynamic properties and the strength of interaction between them. With the introduction of spatial variation come the additional variables of the amplitude and probability distribution of the parameter variation and to which biological model parameter(s) the variation is applied. In this chapter, we focus on these new influences and do not attempt to describe the behaviour for the whole of biological model parameter space, for different plankton population models or for the full range of dynamical behaviour possible for a single population (steady-state, limit cycle and chaotic dynamics). Instead, we select a set of default biological model parameter values that, for an individual independent oscillator, lead to the simplest case of time-varying dynamics - that of regularly periodic dynamics - and describe in detail the emergent behaviour for this case.

Hence, to summarise, this chapter models a spatially varying plankton distribution by considering an interacting ensemble of *non-identical* plankton populations, each of which is oscillatory in nature. We use this set-up to explore how a spatially-varying plankton distribution might behave.

3.2 Method

As in the previous section, we model a spatial distribution of plankton as a lattice of interacting plankton populations with the evolution of each population represented by the same set of ordinary differential equations. We continue to use the Nutrient-Phytoplankton-Zooplankton model formulated by Steele and Henderson (1981). Additionally, we now introduce spatial variation by applying a small random perturbation to a particular biological parameter. This results in a small spread in the natural frequencies of the oscillating populations, where the natural frequency of an oscillator is the frequency at which it would oscillate in isolation of the influence of the other plankton populations.

Again, as in the previous section, the plankton populations interact via a nearest neighbour coupling term representing effective diffusivity. We consider a square region of ocean of size L km $\times$ L km, modelled as a 2D lattice of $n \times n$ interacting plankton populations

$$\mathbf{v}_{i,j} = (N_{i,j}, P_{i,j}, Z_{i,j})$$

where $\mathbf{v}_{i,j}$ occupies the grid-cell in row i and column j of the lattice. Each plankton population interacts with neighbouring populations so that

$$\dot{\mathbf{v}}_{\mathbf{i,j}} = F_{i,j}(\mathbf{v}_{i,j}) + \varepsilon \mathbf{g} \cdot \mathbf{q}$$

where

$$\mathbf{g} = \left(\mathbf{v}_{i-1,j}, \mathbf{v}_{i,j-1}, \mathbf{v}_i, \mathbf{v}_{i,j+1}, \mathbf{v}_{i+1,j}\right),$$

$$F_{i,j}(\mathbf{v}_{i,j}) = F_{i,j}(N_{i,j}, P_{i,j}, Z_{i,j}) = \begin{pmatrix} -\frac{a_{i,j}N}{(e+N)(b+cP)}P + rP + \frac{\zeta\beta P^2}{\mu^2+P^2}Z + \gamma dZ + k(N_0 - N) \\ \frac{a_{i,j}N}{(e+N)(b+cP)}P - rP - \frac{\zeta P^2}{\mu^2+P^2}Z - sP - kP \\ \frac{\zeta\alpha P^2}{\mu^2+P^2}Z - dZ \end{pmatrix}$$

The vector

$$\mathbf{q}_{i,j} = (q_1, q_2, q_3, q_4, q_5)$$

determines which grid-cells interact with grid-cell (i, j), where q_1, q_2, q_4 and q_5 represent material entering from the grid-cells directly adjoining grid-cell i from above, to the left, to the right and from below, respectively, and take a value of 1 if such a grid-cell exists and 0 otherwise, i.e. for grid-cells on the edges of the lattice.

$q_3 = -(q_1 + q_2 + q_4 + q_5)$ determines the amount of material leaving grid-cell (i, j) under the assumption of mass conservation, e.g.

$$\mathbf{q}_{i,j} = (1, 1, -4, 1, 1)$$

for an interior population and

$$\mathbf{q}_{1,1} = (0, 0, -2, 1, 1)$$

for the top left-hand grid-cell. Hence the model describes a lattice with nearest-neighbour effectively-diffusive coupling and no-flux boundary conditions on all edges.

The default biological parameter set, for which the model exhibits limit cycle behaviour, is given in Table 3.1. Note that although we model the nutrient component by its nitrate content, the model has currency of gC m^{-3}.

We introduce a spread in the natural frequencies of the populations by adding a small mismatch $\Delta_{i,j}$ to the default phytoplankton growth parameter a_0 so that $a_{i,j} = a_0 + \Delta_{i,j}$. The random mismatch values $\Delta_{i,j}$ are chosen from a uniform distribution on an interval of width Δ centred on a_0 so that phytoplankton growth rates $a_{i,j} \in [a_0 - \frac{\Delta}{2}, a_0 + \frac{\Delta}{2}]$. The application of mismatch to a implies mesoscale variation in the phytoplankton growth rate. This assumption is justified on the basis that phytoplankton growth has been shown to vary with such factors as temperature (Eppley, 1972) and mixed layer depth (Alpine and Cloern, 1988), all of which vary on the mesoscale (see Chapter 1.2).[1]

3.2.1 Model

The main tool for the investigation of this ensemble of non-identical oscillators is computer code written in the C programming language to initialise and integrate the lattice in time and to write to file the dynamics of each plankton population and other data. The number of oscillators can be altered within the code.

[1]Note that the mismatch values could have been chosen from a different distribution, such as Gaussian; since we do not specify the underlying cause of the spatial variability in this case, our choice of distribution is not constrained by any factors and so we arbitrarily choose a uniform distribution.

Parameter	Symbol	Value	Units
P growth parameter	a_0	0.2	$\mathrm{m}^{-1}\ \mathrm{d}^{-1}$
Light attenuation by water	b	0.2	m^{-1}
Self-shading by P	c	0.4	$\mathrm{m}^2\ \mathrm{gC}^{-1}$
Herbivorous Z mortality	d	0.14	d^{-1}
N half-saturation constant	e	0.03	$\mathrm{gC\ m}^{-3}$
Exchange rate with lower layer	k	0.05	d^{-1}
P respiration	r	0.15	d^{-1}
P sinking	s	0.04	d^{-1}
Lower layer N concentration	N_0	1.0	$\mathrm{gC\ m}^{-3}$
Herbivorous Z assimilation efficiency	α	0.25	
Z excretion fraction	β	0.33	
Remineralisation of Z excretion	γ	0.5	
Herbivorous Z grazing rate	ζ	0.6	d^{-1}
Herbivorous Z grazing half-sat. const.	μ	0.035	$\mathrm{gC\ m}^{-3}$

Table 3.1: Biological model parameters. Note that the model has currency $\mathrm{gC\ m}^{-3}$.

The phytoplankton growth parameter mismatch values are chosen using a random number generator seeded with an integer value; a different choice of seed value leads to a different set of mismatch values with the same probability distribution. The width Δ of the mismatch spread can be altered to be equal to any percentage of the default growth parameter value a_0 and the mismatch values are chosen with a uniform distribution.

Each population $\mathbf{v}_{i,j}$ of the ensemble is given the same set of initial conditions for $N_{i,j}$, $P_{i,j}$ and $Z_{i,j}$, chosen by integrating a single population with parameter values as in Table 3.1 and phytoplankton growth rate a_0, i.e. $\Delta = 0$. Hence the distribution is initially in synchrony. As we know, for non-identical oscillators this synchronous state is not invariant, so the distribution will not remain in synchrony, although it may return to synchrony if the coupling between the populations has the result of counteracting the natural difference in frequencies.

The coupled system is first integrated for a time length T_1 sufficient for transient

behaviour to die away, after which the system is said to be on its attractor. The integration time required for the system to reach its attractor varies depending on the particular set-up, as will be indicated in later sections, e.g. a larger T_1 is required for a larger number of grid-cells comprising the lattice. The necessary T_1 is found by using the technical computing package MATLAB to compare the system dynamics and diagnostic statistics (see Section 3.2.2) output from the main C code for different integration lengths. The system was judged to be on its attractor once the oscillator frequencies had come sufficiently close to steady state (judged visually), after which the system was integrated forward for a further 5,000 time-steps of length dt = 0.1 days to generate a time series of 500 days for calculating the measures used to diagnose different synchronous behaviour.

3.2.2 Diagnostic tools

A first indication of the effect of population interaction on the ensemble dynamics is obtained by plotting the dynamics output from the main C code. In particular, the time evolution of the spatial structure is visualised by using MATLAB to make two-dimensional colour plots of the biological distributions for each time-step. In addition, various diagnostic tools are used to check for different synchronous effects.

The average angular frequency $\omega_{i,j}$ of each oscillator is calculated in order to check for frequency locking of the ensemble. During integration of the system, a note is made of times when each oscillator reaches a peak in its phytoplankton concentration. This gives a series $\{T_{i,j}\}$ of peak times for each oscillator which is used to calculate the average frequency

$$\omega_{i,j} = \left(\frac{N-1}{T_{i,j}(N) - T_{i,j}(1)} \right) \times 2\pi$$

where there are N peaks in the series.

The average rather than instantaneous frequency is calculated in case any of the oscillators are chaotic or have a variable period as a result of interaction with the other oscillators, the interaction having the effect of constantly pulling the populations away from their natural attractors. Once the frequency calculations had converged and were therefore stable with respect to the length of integration, the system was judged to be in statistical steady-state.

From the set of frequencies we calculate the relative standard deviation

$$\sigma = \frac{\text{standard deviation}(\omega_{i,j})}{\text{mean}(\omega_{i,j})} \times 100.$$

The spread of frequencies indicates how the interaction between plankton populations is influencing their behaviour. The ensemble is said to be *frequency locked* when σ is close to 0.

The frequency calculations made in the main C code were checked in two ways. Firstly, the same calculations were carried out in MATLAB using the output $\mathbf{v}_{i,j}$ dynamics from the main C code and the results of these calculations were found to be identical. This indicated that no coding or typing errors were present in the main code. To check the validity of the method for calculating the frequencies, the main code was altered slightly in order to reproduce the results of Fairen (2004), who coupled together 500 non-identical Rössler oscillators in a chain and calculated the frequencies as a function of coupling strength. Both checks indicated that the frequency calculations made by the main code were correct.

The peak times data were also used to calculate phase information for each population. We linearly interpolate between peaks so that the phase at time t is

$$\theta_{i,j}(t) = \left(\frac{t - T_m}{T_{m+1} - T_m} \right) 2\pi$$

where T_m is the peak in $P_{i,j}$ that occurred most recently.

Given the phase $\theta_{i,j}$ of each oscillator, we then calculate the centroid of the oscillators positions on the circle

$$Z = R\mathrm{e}^{\imath\psi} = \frac{1}{n^2} \sum_{i=1}^{n} \sum_{j=1}^{n} \mathrm{e}^{\imath\theta_{i,j}}$$

so that ψ gives the average phase and the *order parameter* R is a measure of the phase coherence of the ensemble. For uncorrelated populations, the phases are uniformly distributed on $[0, 2\pi]$ and so R is around zero. For phase synchronised oscillators at a common phase θ, calculation of the centroid gives $\psi = \theta$ and $R = 1$. Intermediate values of R indicate that the phases of the populations are neither equal nor uniformly spread, e.g. local synchrony or clustering of phases.

R is calculated in MATLAB using the series of peak times output by the main C code. Again, to check the method the R calculations made by Fairen (2004) for a

chain of 500 Rössler oscillators were compared with results from the modified main C code and the two sets of results were found to be identical.

3.2.3 Spatial structure diagnostics

Whilst σ and R give an indication of the coherency in behaviour of the ensemble as a whole, they can mask *local* synchronous effects such as the clustering of the ensemble into sychronised subsets of populations. Hence we use a simple cluster measure $c \in [1, n]$ of grid-cells that gives an indication of the size of clusters in one-dimension. A c value of 1 would be expected for zero coupling, $\varepsilon = 0$, since populations then oscillate in isolation. If the whole ensemble is synchronised, we expect a c value of the length of the domain, i.e. $c = n$. A value of c between 1 and n indicates a certain degree of local synchronisation.

For each time step, c is calculated by taking the $n \times n$ $P_{i,j}$ field

$$\mathbf{P}(t) = \begin{pmatrix} P_{11} & P_{12} & \cdots & P_{1n} \\ P_{21} & \cdots & \cdots & P_{1n} \\ \vdots & & & \\ P_{n1} & P_{n2} & \cdots & P_{nn} \end{pmatrix}$$

and removing its mean to obtain

$$\bar{\mathbf{P}}(t) = \mathbf{P}(t) - \text{mean}(\mathbf{P}(t)).$$

We look at the size of structure in the x and y directions separately to obtain measures c_x and c_y but since the method is identical it is described here for c_x:

We take a transect

$$P_i = (P_{i1}, P_{i2}, \ldots, P_{in})$$

across the lattice for each of the $i = 1, \ldots, n$ rows of grid-cells of the mean-removed field. Clusters are defined as regions of adjacent grid-cells with continuously positive or negative values and their boundaries are found by recording zero-crossings of P_i. Over all rows, this gives a set of clusters

$$\text{clusters}_x = \{c_1, c_2, \ldots, c_m\},$$

where c_k, for $k = 1, \ldots, m$, are integer numbers of grid-cells and $\sum_{k=1}^{m}(c_k) = n^2$. The median of this set of clusters is then calculated for each time-step to give a measure of the local coherency $c_x(t)$, which can also be averaged over time. $c_y(t)$ is calculated in exactly the same manner, but using columns rather than rows of $\bar{\mathbf{P}}(t)$.

The cluster measure given here is only well-defined when clusters exist. That is, it has meaning when there exist well-defined synchronised regions separated by sharp transitions. In this case, c is a good representation of the size, in grid-cells, of these clusters. If such clusters do not exist, and we have instead a gradual shift in phytoplankton biomass values from grid-cell to grid-cell, then the cluster measure as defined here is not appropriate. Take the simple example of a frequency-locked but not phase-locked ensemble with a linear increase in phytoplankton biomass from the left-hand edge to the right-hand edge of the lattice; removing the mean and calculating c in this example will give $c = \frac{n}{2}$, apparently indicating a representative cluster size of half the lattice, whereas actually a cluster size of n is more meaningful since no sharp transitions exist. Additionally, for large cluster sizes with respect to the domain size, the c measure will be inherently less reliable than for small clustering: fewer larger clusters will fit into the domain, reducing the probability when taking the median of obtaining an accurate estimate for c.

For this reason, in conjunction with the cluster measure we also consider a measure of the sharpness of transitions from grid-cell to grid-cell across the lattice to show the sharp edges of clusters and to highlight where c is less appropriate. For each time-step we normalise the $\mathbf{P}(t)$ field to obtain

$$\hat{\mathbf{P}}(t) = \left(\frac{\mathbf{P}(t) - \min(P_{i,j}(t))}{\max(\mathbf{P}(t) - \min(P_{i,j}(t)))} \right)$$

with $0 \leq \hat{P}_{i,j}(t) \leq 1$ for $i, j = 1, \ldots, n$. For each grid-cell, we define $g_{i,j}(t)$ as the maximum value of the absolute difference between $\hat{P}_{i,j}(t)$ and the phytoplankton biomass in each of its up to eight (for interior populations) nearest neighbours, i.e. for interior populations,

$$g_{i,j}(t) = \max\{|\hat{P}_{i,j} - \hat{P}_{i',j'}|\}$$

for $i' = i - 1, i, i + 1$ and $j' = j - 1, j, j + 1$.

Then,

$$g(t) = \max_{i,j}(g_{i,j}(t)).$$

In the limit case of fully synchronised dynamics, we have $g(t) = 0$. As the sharpness of the gradient between clusters increases, $g(t) \to 1$. The maximum rather than mean or median is appropriate here as we wish to identify the presence of extreme gradients rather than get an impression of the average gradient for the lattice.

Calculations of the cluster measure c and gradient measure g are made with MATLAB using the dynamical output from the main C code.

Finally, we calculate the 2D power spectrum of the mean-removed $\mathbf{P}(\mathbf{t})$ for each time-step. Here we give an outline of the method, but full details are available in Press et al. (1992).

To prevent spectral leakage, inevitable when taking the Fourier transform of a field with abrupt edges, the edge gradient is softened by multiplying $\mathbf{P}(t)$ by an $n \times n$ Hann window defined by

$$W(i,j) = \frac{1}{4}\left(1 - \cos\frac{2\pi i}{n}\right)\left(1 - \cos\frac{2\pi j}{n}\right)$$

to obtain

$$\mathbf{P_w}(t) = \mathbf{P}(t) \cdot W.$$

As required by the Fast Fourier Transform (FFT), the $n \times n$ field $\mathbf{P_w}(t)$ is padded with zeros to make it of size $2^N \times 2^N$ where $N = \text{ceiling}\left(\frac{\log(n)}{\log(2)}\right)$, i.e. the next power of 2.

The MATLAB function `fft2` is used to calculate the Fourier components $FT(k_x, k_y)$ in wavenumber space, where the wavenumbers indicate the number of full waves contained in the region represented by $\mathbf{P}$. To obtain the power spectrum, we sum the energy in annuli of width one in wavenumber space about the centre as follows:

$$S(I) = \frac{\sum_{d(k_x,k_y)\in(I,I+1)} |FT(k_x,k_y)|^2}{\pi((I+1)^2 - I^2)}$$

where $d(k_x, k_y) = \sqrt{k_x^2 + k_y^2}$ and $I = 0, \ldots, \frac{n}{2} - 1$.

For a fully synchronised ensemble, we expect to see all energy focused at the wavenumber $k = 1$ since no spatial structure exists below the level of the full domain. How the peak of the power spectrum changes with, for example, time or coupling

strength, gives an indication of the changing spatial organisation of the interacting ensemble.

These diagnostic tools, summarised in Table 3.2, used together allow us to describe in detail the different synchronous behaviour displayed by the plankton distribution as variables of the model set-up are altered.

Measure	Symbol	Range	Units
Phytoplankton biomass of population (i, j)	P_i	0-0.5	gC m^{-3}
Angular frequency of population (i, j)	ω_i	0.05-0.15	$2\pi d^{-1}$
Frequency spread	σ	0-25	%
Phase order	R	0-1	
Cluster measures	c_x, c_y	1-n	grid-cells
Gradient measure	g	0-1	

Table 3.2: Summary of diagnostic statistics.

3.3 Dependence on strength of interaction

We first explore how the emergent features of this lattice of coupled plankton populations depend upon the *strength of interaction* between the populations. How does the interaction alter the oscillations of the individual populations to determine the temporal and spatial structures of the plankton distribution? We will explore this by varying the strength of effective diffusivity in the model as described below.

For a lattice of coupled plankton populations set up as previously described, the coupling term, which is essentially the coupling strength ε multiplied by the difference in concentration δC between neighbouring grid-cells of size l, where C may represent nutrient, phytoplankton or zooplankton concentration, represents mixing processes between adjacent grid-cells so that

$$\varepsilon \delta C \approx D \frac{\partial^2 C}{\partial x^2}$$

where D is effective diffusivity. Hence we may equate ε with the effective diffusivity so that

$$\varepsilon \approx \frac{D}{l^2}$$

where l is the grid-cell length-scale and $\frac{1}{l^2}$ approximates the second order spatial derivative

The effective diffusivity has been shown by Okubo (1971) to scale with spatial length-scale according to the empirical relationship

$$D(l_s) \approx 0.01 {l_s}^{1.15}$$

with l_s in cm and effective diffusivity $D(l_s)$ in cm^2 s^{-1}. If we then take the grid-cell length-scale l km of the lattice as the spatial scale at which effective diffusivity acts in the model, then

$$\varepsilon \approx 0.01 l^{-0.85} \times 60 \times 60 \times 24$$

for ε in d^{-1}. For mesoscale processes on the order of 1 km to 100 km, this gives a range of coupling

$$\varepsilon \in [0.001, 0.05] \text{ d}^{-1}$$

between adjacent grid-cells with coupling strength increasing with decreasing length-scale (see Figure 3.1). Varying ε in this range is equivalent to varying the spatial resolution of the model from 100 km to 1 km, i.e. $l \in [1, 100]$ km. However, since an understanding of the uncoupled system ($\varepsilon = 0$) is essential to an understanding of the coupled system ($\varepsilon > 0$), in this work we consider the range

$$\varepsilon \in [0, 0.05] \text{ d}^{-1}.$$

For this investigation into how the strength of effective diffusivity determines the emergent properties of the ensemble, we have the following specific set-up.

We set $n = 100$ to give a lattice of 100×100 populations. This number of grid-cells is chosen so that the ensemble remains small enough to be computationally inexpensive but large enough to give an unbiased sample of the uniform distribution for the random mismatch values $\{\Delta_{i,j}\}$, for $i, j = 1, \ldots, n^2$, to be applied to the phytoplankton growth parameter a_0. We set $\Delta = 5\%$ of a_0 so that the mismatch values are uniformly distributed on an interval $a_0 \pm 2.5\%$, giving

$$a_{i,j} \in [0.195, 0.205]$$

as shown in Figure 3.2 (*top panel*). For these parameter values, the biological model displays oscillatory dynamics, with the parameter mismatch resulting in a

Figure 3.1: Coupling strength ε according to Okubo (1971) empirical relationship between grid-cell spatial scale l in km and effective diffusivity in d^{-1}.

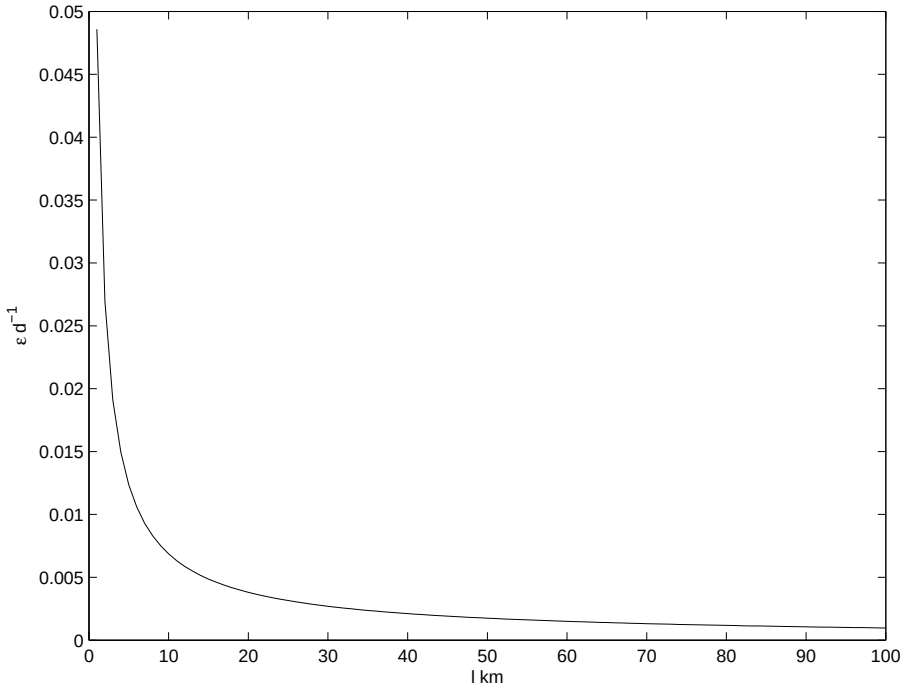

slight difference in amplitude and period of oscillation for each population: the resulting spread in natural frequencies of the plankton populations is approximately 2.5% as shown in Figure 3.2 (*bottom panel*), with mean frequency $\Omega = 0.052$. The resulting natural frequencies are not uniformly distributed; evidently the impact of the parameter mismatch on the frequency of the plankton population is non-linear.

Using exactly the same set and spatial arrangement of mismatch values $\Delta_{i,j}$ for each simulation, the coupling strength ε is varied in the range given above. Varying ε in this range is equivalent to varying the grid-cell length-scale from 100 km to 1 km, which, since $n = 100$ for each run, is equivalent to varying the domain size $L \times L$ from 10,000 km $\times$ 10,000 km to 100 km $\times$ 100 km.

3.3.1 Temporal evolution

The system is integrated from initially synchronised dynamics for T_1 time-steps of length dt = 0.1 days sufficient for statistically steady-state dynamics to be reached. In general, $T_1 = 50,000$ iterations $= 5,000$ days is found to be sufficient, with

Figure 3.2: Histogram of phytoplankton growth parameters $a_{i,j}$ and resultant natural frequencies $\omega_{i,j}(\varepsilon = 0)$ for $i, j = 1, \ldots, 100$.

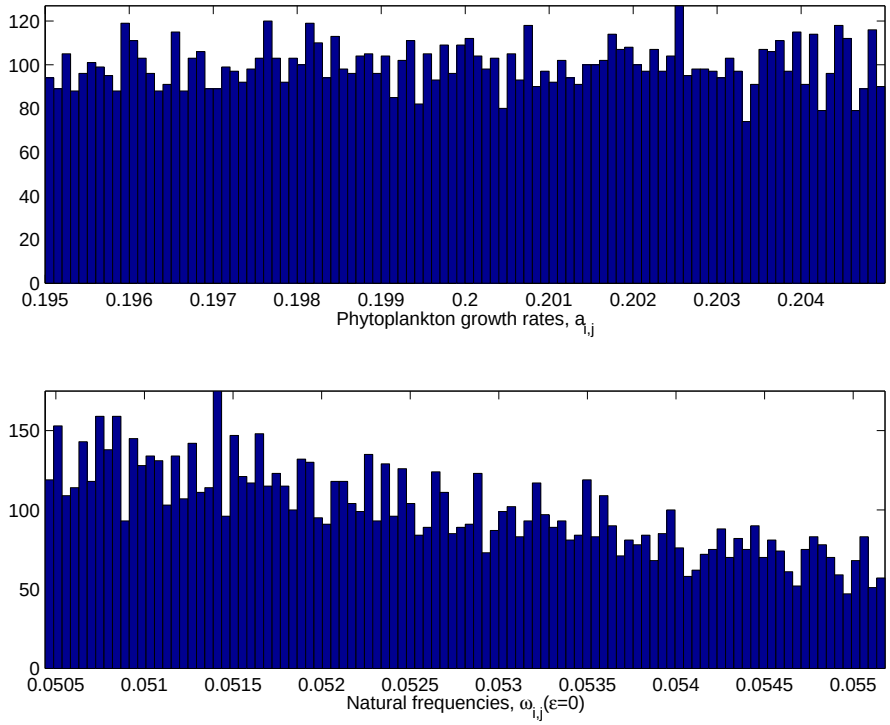

spatial statistics remaining stable for $T > T_1$. However, as will be discussed later, the steady-state dynamics take longer to emerge for coupling strengths near to transitions in system behaviour.

Figure 3.3 gives an example of how spatial structure emerges from the initially homogeneous state; the phytoplankton field is shown at 100 day intervals for a coupling strength of $\varepsilon = 0.01$ d^{-1}. We see how the initial domain-sized structure breaks down into well-defined clusters. Circular regions appear, containing small scale-clusters, which are themselves not circular but appear as elongated shapes. These circular regions grow, increase in number and merge until the domain is filled with clusters which change in size with time until appearing to reach a statistical steady state at around $t = 2,500$ days. The calculated cluster measures $c_x(t)$ and $c_y(t)$ plotted in Figure 3.4 confirm what can be seen visually: the structure in both directions reaches a steady state length-scale of 4 to 5 grid-cells. Relating the coupling strength $\varepsilon = 0.01$ to a grid-cell length-scale of around 6.4 km using the Okubo relationship, this gives a steady-state cluster size of approximately 25 to

32 km. The clusters are well-defined synchronised regions, with sharp transitions at their boundaries, as indicated by a steady state value of $g(t) \approx 0.85$ in Figure 3.4. Importantly, although the cluster size converges, the position of these clusters is non-stationary, indicating that the spatial arrangement of the structure is not a simple reflection of the spatial arrangment of the underlying natural frequencies; the clustering structure continues to evolve in time after the spatial structure mean size has reached a steady-state, hence we speak of a *statistical* steady-state.

The time-evolution plots clearly show that $\varepsilon = 0.01$ d^{-1} is not a strong enough coupling to counteract the natural frequency disorder and keep the system in full synchronisation, but a certain amount of local synchronisation does exist.

A clear, approximately 120 day oscillation, can be seen in $c_x(t)$, $c_y(t)$and $g(t)$ and, initially, in the phytoplankton dynamics plotted in Figure 3.4. This may explain why the system takes such a long time - approximately 7 years - to shed its transient behaviour. From the initially synchronised state, the amount of disparity in phytoplankton biomass increases with each period of oscillation. Since the period of oscillation is long - approximately 120 days - the synchronous state persists for some time before the system reaches its attractor. Since the model is not subject to any seasonal forcing and also has not been tuned to any particular period, this 120 day period is not intended or considered as a realistic period of oscillation. It is hypothesised, although not explored directly here, that a shorter period of oscillation would shorten the time of transient dynamics.

For the same system ($\varepsilon = 0.01$ d^{-1}; n=100), Figure 3.5 shows the biomass fields for nutrient, phytoplankton and zooplankton at time $t = 5000$ days. Figure 3.5 also shows the time evolution of all three model components for the last 500 days at the centre grid-cell $v_{50,50}$ of the lattice and a snapshot transect across the centre of the lattice ($i = 50$) at time $t = 5000$ days. The same spatial structure is seen for all three components, with synchronised regions of phytoplankton biomass roughly corresponding to synchronised regions of zooplankton biomass and nutrients. However, clusters of high phytoplankton biomass may correspond to areas of high or low nutrient levels and zooplankton biomass, as expected from the nature of species interaction and illustrated by the time-series and transect. The transect clearly

shows the sharp gradients in biomass at cluster edges. Since the same synchronous properties are observed for all three model components, further results are illustrated only in terms of the phytoplankton components for brevity and clarity.

Figure 3.3: **Temporal dynamics.** Evolution of phytoplankton biomass field for 5,000 days from initially synchronised conditions for lattice of 100×100 plankton populations interacting with effective diffusivity $\varepsilon = 0.01$ d^{-1}. Figure labels indicate time in days.

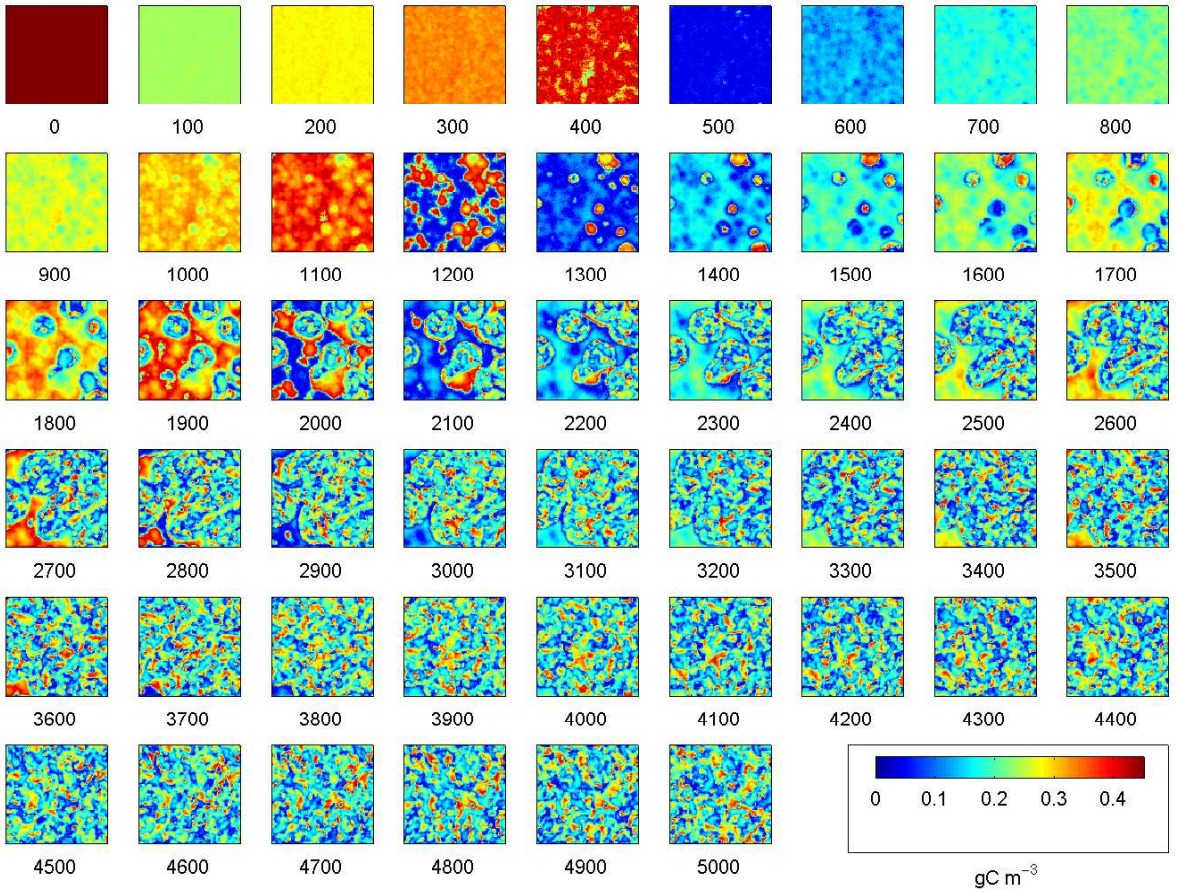

3.3.2 Steady-state dynamics

An integration of a further $T_2 = 500$ days was used to calculate the diagnostics. Figure 3.6 shows how the frequency spread σ, phase order parameter R and the frequencies of the oscillators vary as a function of coupling strength for $\varepsilon \in [0, 0.05]$ d^{-1}. It is immediately seen that increasing the coupling strength does not have the intuitive effect of monotonically increasing the degree of synchrony exhibited by the ensemble: we do not have a monotonic decrease in σ and increase in R as ε is increased. The final phytoplankton field at time $t = (T_1 + T_2)$ for each value of ε is shown in Figures 3.7 to 3.12. Figure 3.13 shows the spatial measures c_x, c_y and g as a function of ε. In Figure 3.14, the cluster measures c_x and c_y in grid-cells are scaled by the length-scale $l(\varepsilon)$ km according to the Okubo relationship to give cluster length-scales in km.

As ϵ is increased from zero, the diagnostic tools and spatial phytoplankton biomass plots indicate that the dynamics of the ensemble exhibits four qualitatively different states.

- **$\varepsilon = 0$ $\mathbf{d^{-1}}$: independent populations.**

  For zero coupling the plankton populations oscillate independently, so that the phytoplankton field shown in the first subplot of Figure 3.7 is random with no spatial structure larger than the grid-cell, as confirmed by c_x and c_y values of 1 in Figure 3.13 and a wide frequency spectrum in Figure 3.7. As expected, $\sigma \approx 2.5$ % (see Figure 3.6). Since there is no interaction between neighbouring populations, there can be a sharp transition in phytoplankton biomass from grid-cell to grid-cell, indicated by gradient measure value of $g = 1$ (Figure 3.13).

- **$0 < \varepsilon \leq 0.001$ $\mathbf{d^{-1}}$: small increase in frequency spread; small-scale clustering.**

  For $0 < \varepsilon < 0.001$ the spread in frequencies increases with increased coupling strength (Figure 3.6). The frequencies are seen in general to increase but, since the oscillators do not all increase in frequency at the same rate as a function of ε, σ increases to more than 5%. Despite the increase in σ, the clustering in the

Figure 3.4: **Temporal dynamics.** Evolution of spatial structure for 5,000 days from initially synchronised conditions for lattice of 100×100 plankton populations interacting with effective diffusivity $\varepsilon = 0.01$ d^{-1}, showing phytoplankton dynamics for each $P_{i,j}(t)$ for $i, j = 1, \ldots, 100$, cluster measures $c_x(t)$ (*black*) and $c_y(t)$ (*red*) and gradient measure $g(t)$.

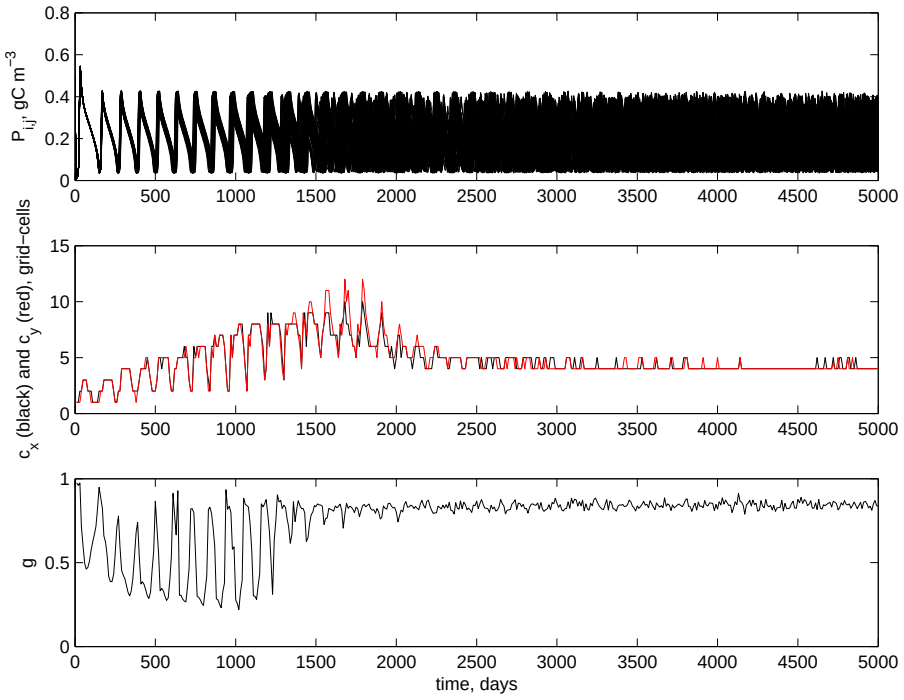

Figure 3.5: **NPZ dynamics**. Nutrient (N), phytoplankton (P) and zooplankton (Z) biomass fields in gC m^{-3} at time $t = 5000$ days after integration from homogenous initial conditions; evolution of N (black), P (green) and Z (red) for final 500 days of integration for the population in the centre of the lattice ($i = j = 50$); and $N(x)$, $P(x)$ and $Z(x)$ at time $t = 5000$ for a transect across the centre of the lattice ($i = 50$, $j = 1, \ldots, 100$). Coupling strength $\varepsilon = 0.01$ d^{-1}, $n = 100$.

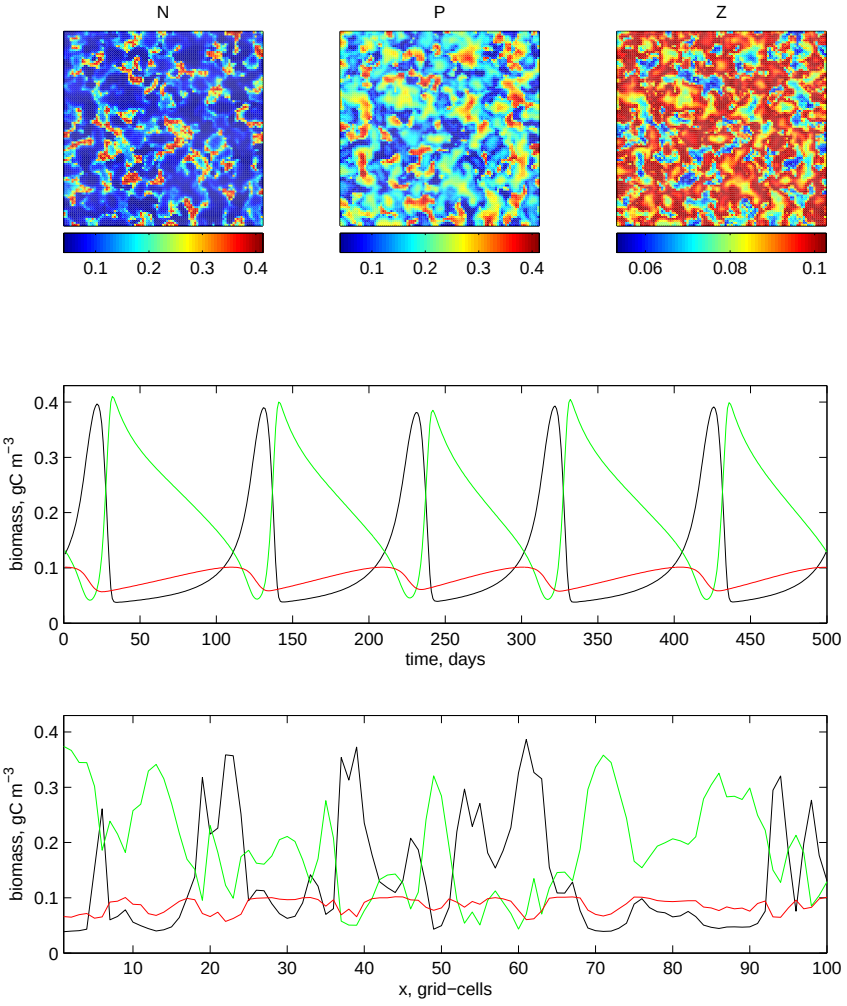

biomass plots and the narrowing of the associated spatial frequency spectra in Figure 3.7 indicate that the size of spatial structure in the phytoplankton field has increased between $\epsilon = 0.0005$ and $\epsilon = 0.001$. It is evident that the increase in coupling has caused an increase in local synchronisation although the size of the clusters remain small with only a small increase in c to 2-3 grid-cells. These clusters are well-defined, as indicated by $g = 1$ in this region (Figure 3.13).

- **$0.001 < \varepsilon \leq 0.0025$ d^{-1}: frequency-locking; large-scale clustering.**

  For coupling around $\varepsilon = 0.002$ d^{-1} there is a small region of near frequency locking, seen by a rapid decrease in σ to $< 1\%$ (Figure 3.7). The scale of spatial structure increases; the phytoplankton biomass field shows much larger clusters, the spectrum narrows and the cluster measure increases to $c_x = c_y =$ 10 grid-cells (Figure 3.13). However, the system is clearly not phase locked since neighbouring clusters coexist with some at their peak in phytoplankton biomass and some at their trough, confirmed by an order parameter value of $R \approx 0.6$ (Figure 3.6), with sharp transitions at cluster boundaries indicated by $g = 0.9$ (Figure 3.13).

- **$0.0025 \leq \varepsilon \leq 0.02$ d^{-1}: large frequency spread; small-scale clustering.**

  For $\varepsilon = 0.0025$ d^{-1}, two discrete sizes of spatial structure appear to coexist. However, this system is not in steady state even after 5000 days. When the system is integrated for a further 5000 days, the large-scale structure disappears and the entire domain is filled with the small-scale spatial structure. The transient behaviour takes longer to disappear when the system is near a change in behaviour, which is what ocurs at this point.

  As ε is increased above 0.0025 d^{-1}, the ensemble bursts out of frequency locking and enters a desynchronised region for $\varepsilon \in (0.0025, 0.02)$ d^{-1}, shown in Figures 3.7 to 3.9. The spread in frequencies reaches an order of magnitude higher than the spread in natural frequencies and increasing ϵ within this region apparently has no effect on the amount of disorder in the frequencies (Figure 3.6). However, clustering is clearly visible in the phytoplankton distri-

bution snap-shots for coupling in this region (Figures 3.7 to 3.9). Additionally, although σ gives no evidence of an increase in the amount of synchrony for increased coupling, the phytoplankton fields clearly show an increase in the size of clusters as ϵ is increased; the amount of local synchrony in both the x and y directions increases and c_x and c_y increase slowly and monotonically from 2 to 7 grid-cells (see Figure 3.13). However, Figure 3.14 indicates that the actual cluster size monotonically *decreases* from around 50 km to 20 km. The gradient measure remains high ($g > 0.7$) in this region as clusters are still well-defined (Figure 3.13).

Note that the statistical steady-state for the temporal dynamics shown in Figure 3.3 occupies this small-scale clustering region.

- **$0.02 < \varepsilon \leq 0.05$ d^{-1}: frequency-locking; near domain-sized spatial dynamics; near phase-locking.**

  Above $\epsilon = 0.02$ there is a rapid, threshold-like transition to a frequency-locked state, with a decrease in σ to near zero. This transition is seen in the phytoplankton fields in Figure 3.10.

  The dynamics are largely synchronised, with structure almost at the size of the domain and no sharp transitions between neighbouring grid-cells, unlike in the clustering state. We see a rapid decrease in g at this threshold to values around 0.3 (Figure 3.13), showing that clusters are no longer well-defined and that changes in phytoplankton biomass across the lattice occur instead on a gentle gradient. As explained above, the cluster measure is no longer appropriate for a low value of g, although we note that c_x and c_y increases rapidly to approximately half the domain size at this threshold (Figure 3.14), indicating a rapid increase in dominant spatial structure.

  The system remains frequency-locked for increased coupling after this transition and the resultant frequency of the synchronised system tends towards the mean of the natural frequencies, $\Omega = 0.052$. Figure 3.15 shows how the distribution of the population frequencies develops as the effective diffusivity is increased. For $0 < \varepsilon < 0.003$ the original distribution of natural frequencies

narrows as the system becomes nearly frequency locked. For $\varepsilon \geq 0.003$ the distribution widens, showing a tendency for populations to oscillate faster as a result of interaction. From $\varepsilon = 0.015$ d^{-1}, a bimodal distribution develops, with a wide residual group of faster oscillators and a distinct "break-away" narrow band of populations with frequencies around $\Omega \approx 0.05$. An increasing number of populations is recruited into this second group, seen in Figure 3.15 as a diminishing of the wide group of faster oscillators, until at the critical coupling for frequency locking, $\varepsilon_{FL} \approx 0.02$, the faster group disappears, the distribution in frequencies appears as a single spike at $\Omega \approx 0.05$ and the ensemble is frequency-locked. Since this state remains for $\varepsilon > 0.02$, histograms are not shown for the full range of ε.

In contrast to the threshold-like change to frequency-locking, the transition to phase-locking after $\epsilon = 0.02$ is gradual, as seen by a slow monotonic increase in R towards 1 (Figure 3.6). For coupling in the range considered here of $\epsilon < 0.05$, we see that the ensemble never achieves fully phase-locked dynamics, as $R < 1$ (Figure 3.6) and the variation in colour in the biomass plots in Figures 3.10 to 3.12 always indicates some variation in the phase of oscillation of the populations across the domain. However, the dynamics gradually become more homogeneous and the spatial frequency spectra in these regions are narrow with peaks at a wavenumber of 1, indicating dominant structure at the domain size.

From the incomplete invasion of small-scale spatial structure apparent in Figure 3.10 for $\varepsilon = 0.02$, we see again that transients persist for longer near to threshold-like changes in system behaviour. Comparing this plot with the temporal evolution plots shown in Figure 3.3, we might ask whether there is really a transition in behaviour at $\varepsilon > 0.02$ or whether the dynamics above this coupling strength have simply not been integrated for long enough to come to steady state. Would small-scale structure, like that seen for $\varepsilon < 0.02$, develop if the system were integrated for longer for $\varepsilon > 0.02$? To check this, a further integration with $T_1 = 20,000$ iterations (four times longer) was carried out for $\varepsilon \in (0.0175, 0.0225)$, the area around the apparent transition. The resultant spread in frequencies is shown in Figure 3.16. Although the longer

integration time alters σ values around the threshold, as dynamics have longer to reach steady-state, the value of ε at which the transition occurs is the same. By simulation alone, it cannot be shown conclusively that a longer integration would not allow smaller-scale structure to develop for $\varepsilon > 0.02$, pushing the transition further to the right on Figure 3.16. However, if that were the case then it would be expected that the threshold would have moved at least some distance further to the right after the longer integration shown by the solid line in Figure 3.16. Hence we are confident that the apparent threshold is a real transition to a different type of dynamics.

3.3.3 Boundary conditions and initial conditions

We are interested in the ensemble statistics and spatial structure that result from the interaction between the individual populations. Hence, it is necessary to be sure that these emergent properties are not imposed upon the system by the choice of initial and boundary conditions.

No-flux boundary conditions are used as default in this investigation. An additional simulation was carried out with all parameters as in the previous section ($n = 100$, $\varepsilon \in [0, 0.05]$, $\Delta = 5\%$ and the same set of $a_{i,j}$) but with doubly-periodic rather than no-flux boundary conditions. Figure 3.17 shows the resultant spread in population frequencies as a function of coupling strength, with results for the no-flux case shown as a dotted curve for comparison. The shapes of the two curves are seen to be almost identical, with transitions between types of ensemble dynamics occurring at the same values of ε. Equally, the emergent spatial structure in phytoplankton biomass shown in 3.17 is close to that seen in the case of no-flux boundary conditions. This indicates that the ensemble dynamics are not sensitive to the choice of boundary conditions.

The influence of the initial conditions was also investigated. The system is usually integrated from homogeneity and this state is observed to persist or break down into asynchrony or clustering, depending upon the parameters of the system. An additional simulation was carried out for $n = 100$, $\varepsilon \in [0, 0.05]$ and $\Delta = 5\%$ with *asynchronous* initial conditions, obtained by integrating the *uncoupled* system

($\varepsilon = 0$) for 5000 days and using the final N_i, P_i and Z_i values as initial conditions in the *coupled* case ($\varepsilon > 0$), so that in this case the clustering or fully synchronous state was seen to emerge from asynchrony. The results of $\sigma(\varepsilon)$ and the emergent spatial dynamics in the cases of (i) synchronised and (ii) desynchronised initial conditions were found to closely match and are as in Figures 3.6 and 3.7 to 3.12 (and so are not reproduced here). Hence the system is not sensitive to the choice of initial conditions. Additionally, this confirms $\varepsilon \approx 0.02$ d^{-1} as a bifurcation point to stable synchrony.

Figure 3.6: **Diagnostics for n = 100 as a function of coupling strength**. Frequencies $\omega_{i,j}(\varepsilon)$ for $i, j = 1, \ldots, 100$ (*top panel*), standard deviation of frequencies σ (*dotted line*) and order parameter R (*solid line*) for $\varepsilon \in [0, 0.05]$ d^{-1} (*middle panel*) and a zoomed-in section of σ for $\varepsilon \in [0, 0.0025]$ d^{-1} (*bottom panel*).

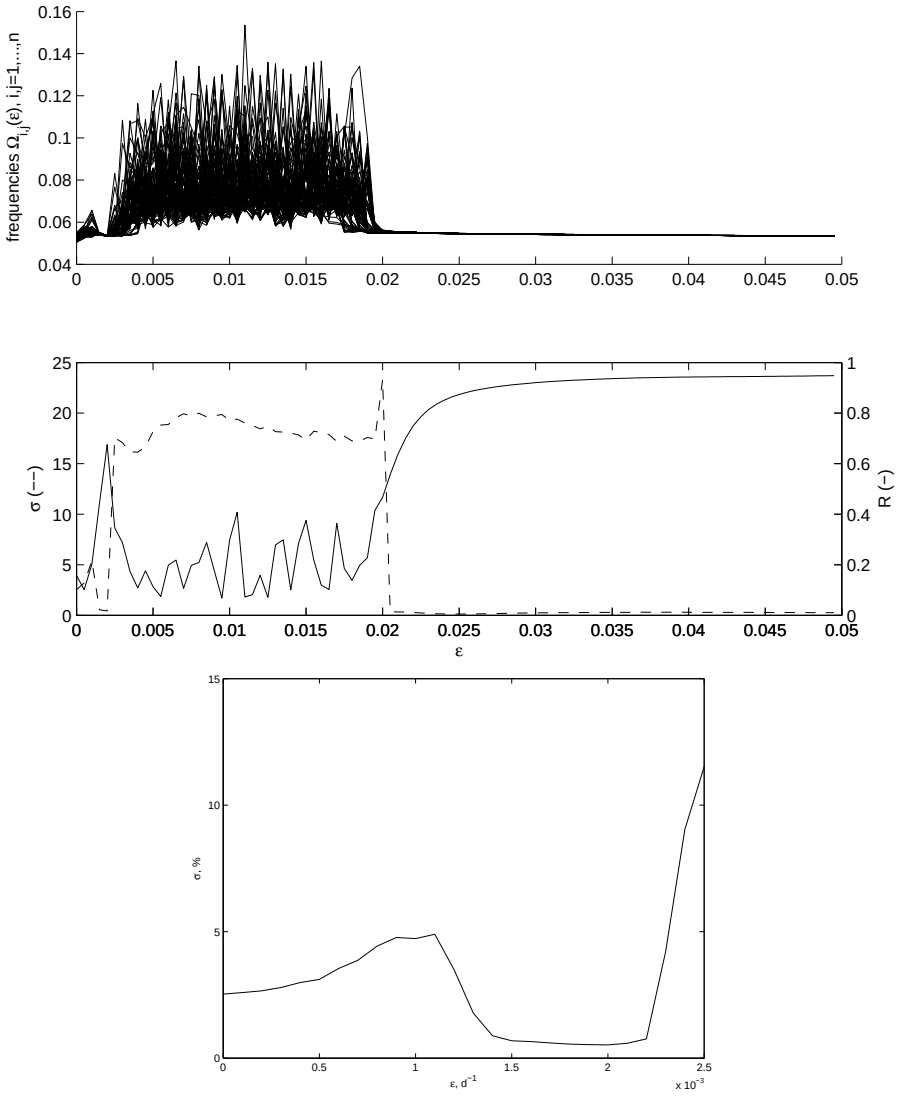

Figure 3.7: **Spatial dynamics for varying effective diffusivity**. Phytoplankton biomass field (*columns 1 and 3*) and wavenumber spectra (*columns 2 and 4*) for $n = 100$ at time $t = T_1 + T_2$, after initial integration of length $T_1 = 5,000$ days to remove transients and additional integration of length $T_2 = 500$ for calculation of diagnostics for $\varepsilon \in [0, 0.0045]$ d^{-1}. Figure title numbers indicate value of ε.

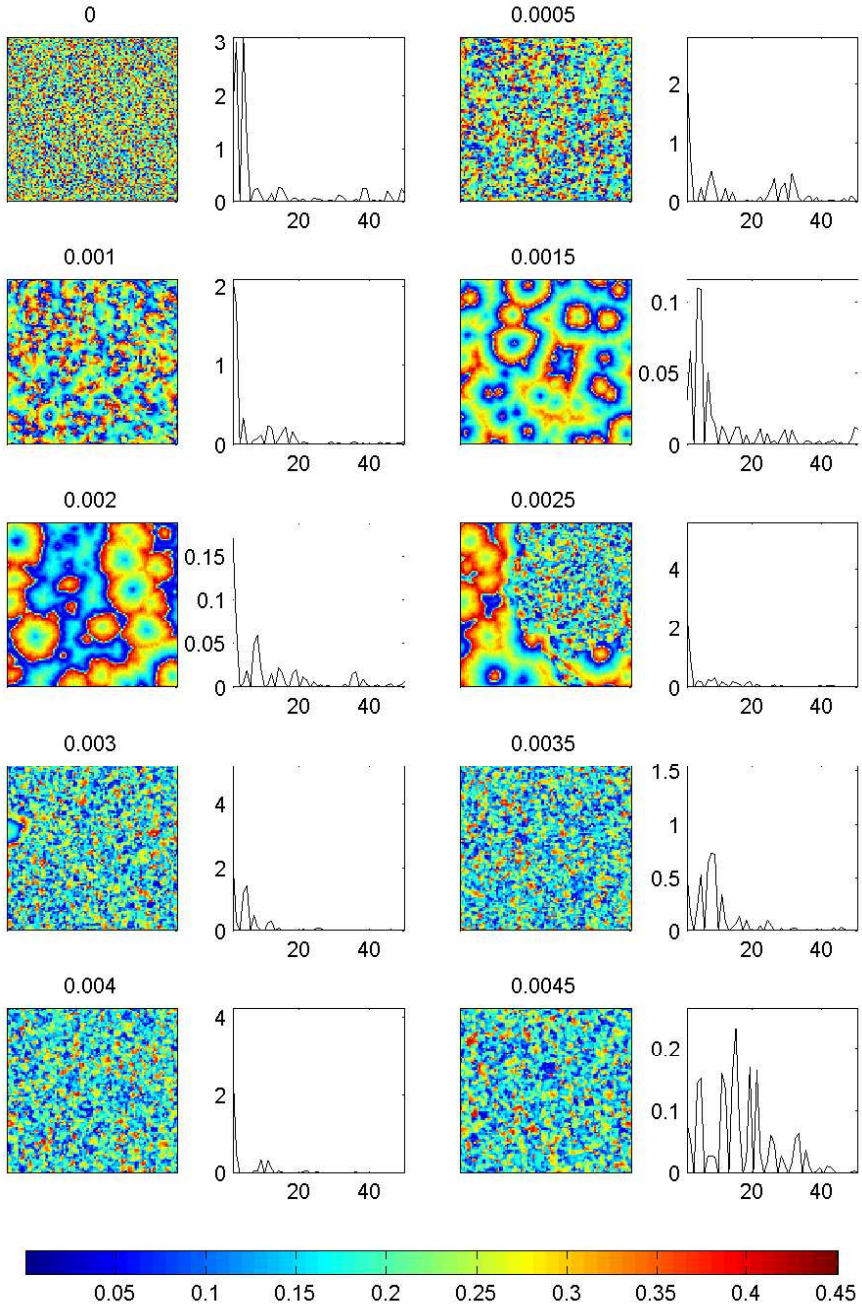

Figure 3.8: **Spatial dynamics for varying effective diffusivity**. Phytoplankton biomass field (*columns 1 and 3*) and wavenumber spectra (*columns 2 and 4*) for $n = 100$ at time $t = T_1 + T_2$, after initial integration of length $T_1 = 5,000$ days to remove transients and additional integration of length $T_2 = 500$ for calculation of diagnostics for $\varepsilon \in [0.005, 0.0095]$ d^{-1}. Figure title numbers indicate value of ε.

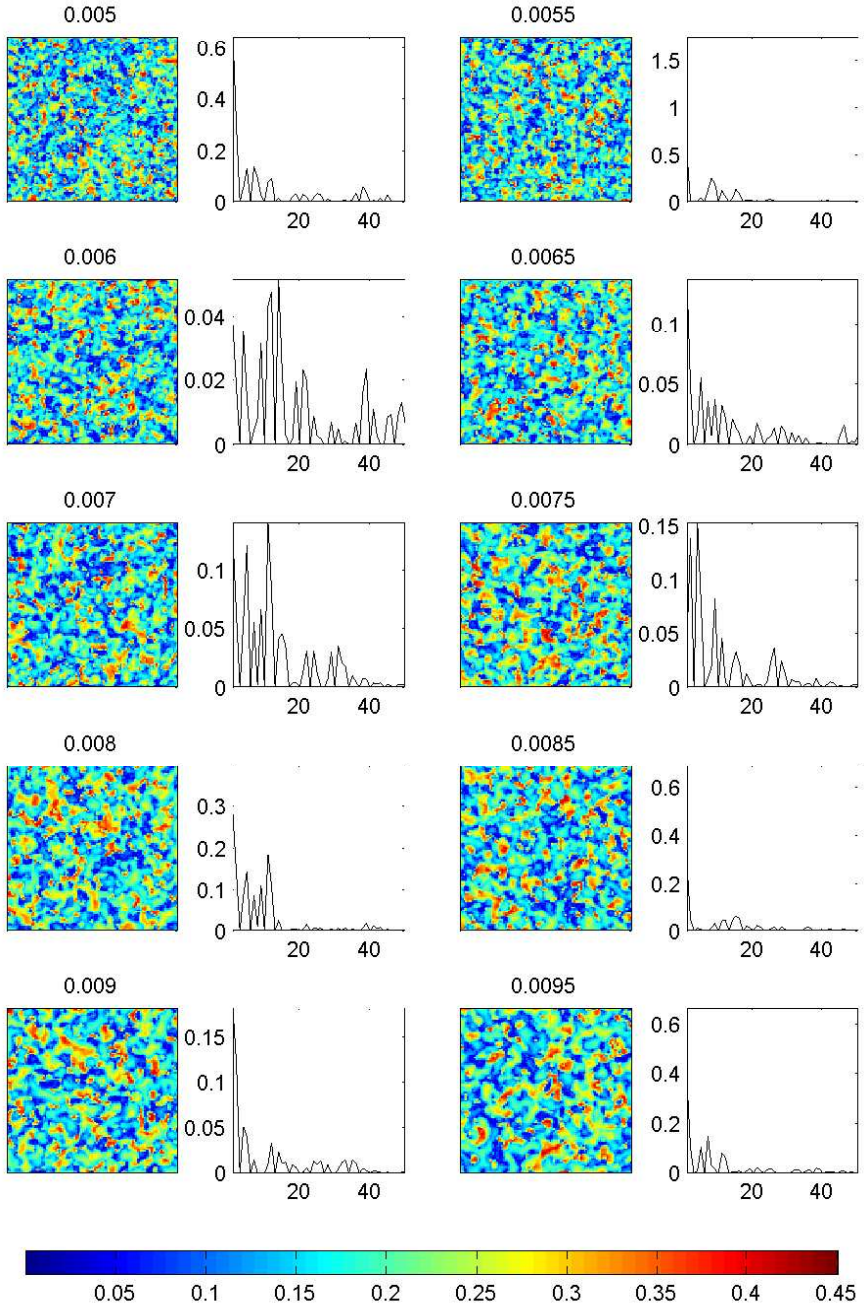

Figure 3.9: **Spatial dynamics for varying effective diffusivity**. Phytoplankton biomass field (*columns 1 and 3*) and wavenumber spectra (*columns 2 and 4*) for $n = 100$ at time $t = T_1 + T_2$, after initial integration of length $T_1 = 5,000$ days to remove transients and additional integration of length $T_2 = 500$ for calculation of diagnostics for $\varepsilon \in [0.01, 0.019]$ d^{-1}. Figure title numbers indicate value of ε.

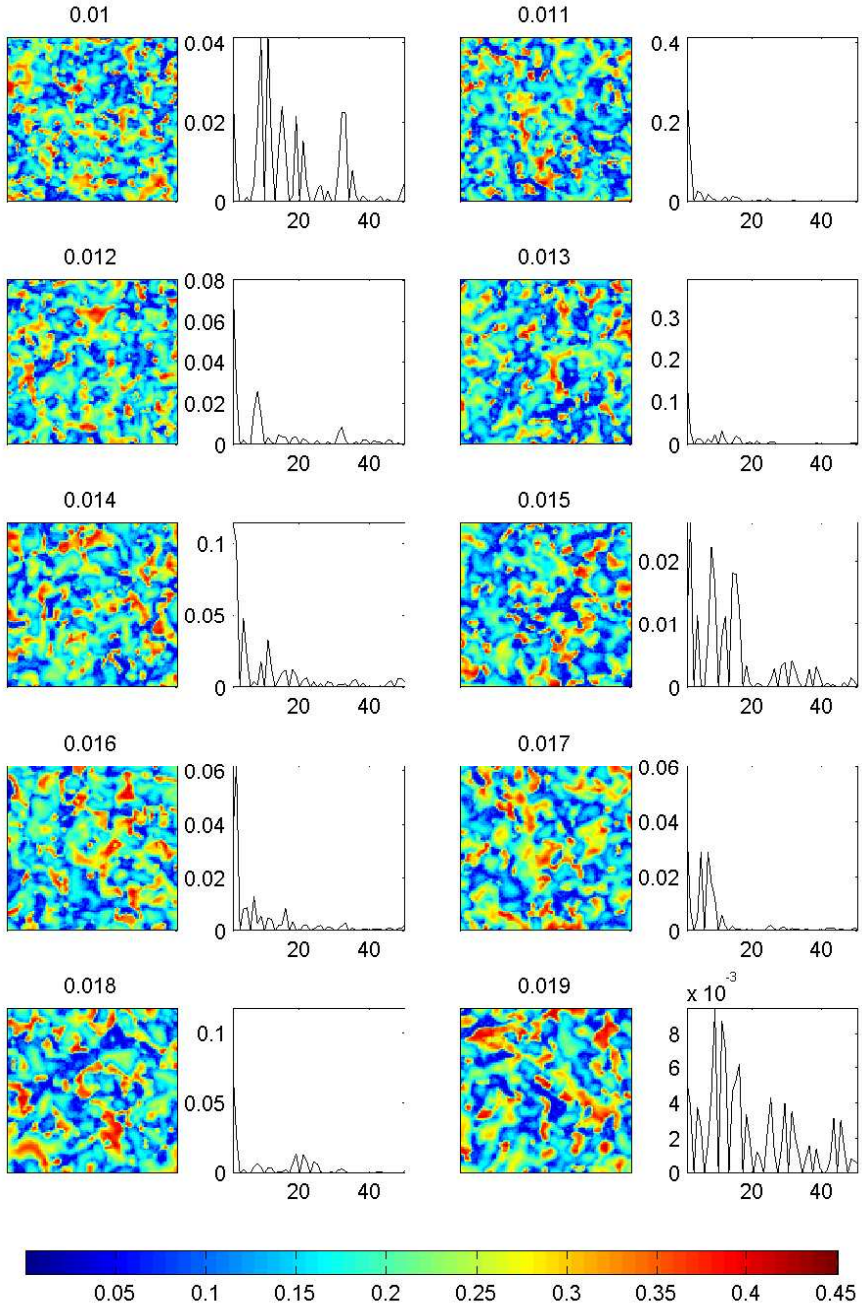

Figure 3.10: **Spatial dynamics for varying effective diffusivity**. Phytoplankton biomass field (*columns 1 and 3*) and wavenumber spectra (*columns 2 and 4*) for $n = 100$ at time $t = T_1 + T_2$, after initial integration of length $T_1 = 5,000$ days to remove transients and additional integration of length $T_2 = 500$ for calculation of diagnostics for $\varepsilon \in [0.02, 0.029]$ d^{-1}. Figure title numbers indicate value of ε.

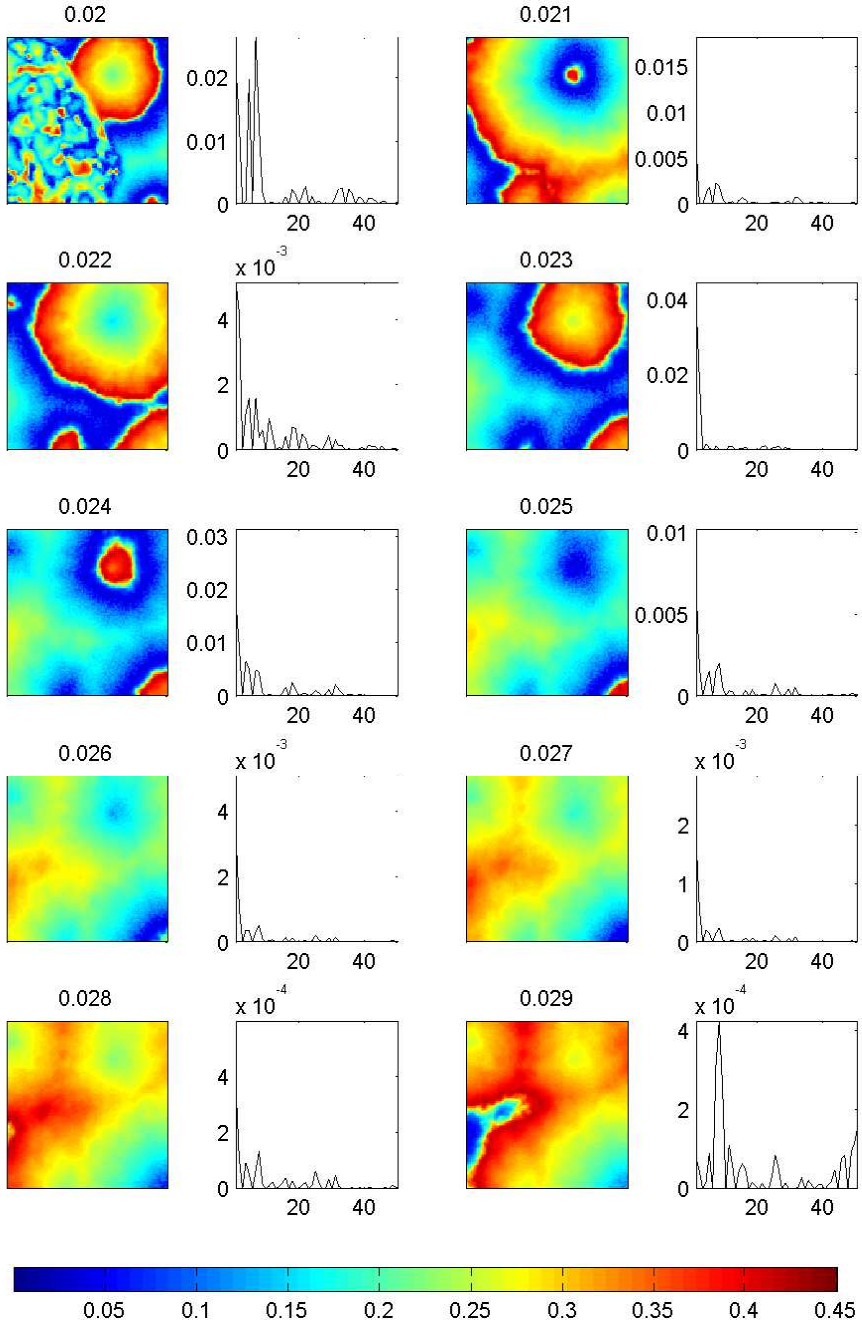

Figure 3.11: **Spatial dynamics for varying effective diffusivity**. Phytoplankton biomass field for (*columns 1 and 3*) and wavenumber spectra (*columns 2 and 4*) $n = 100$ at time $t = T_1 + T_2$, after initial integration of length $T_1 = 5,000$ days to remove transients and additional integration of length $T_2 = 500$ for calculation of diagnostics for $\varepsilon \in [0.03, 0.039]$ d^{-1}. Figure title numbers indicate value of ε.

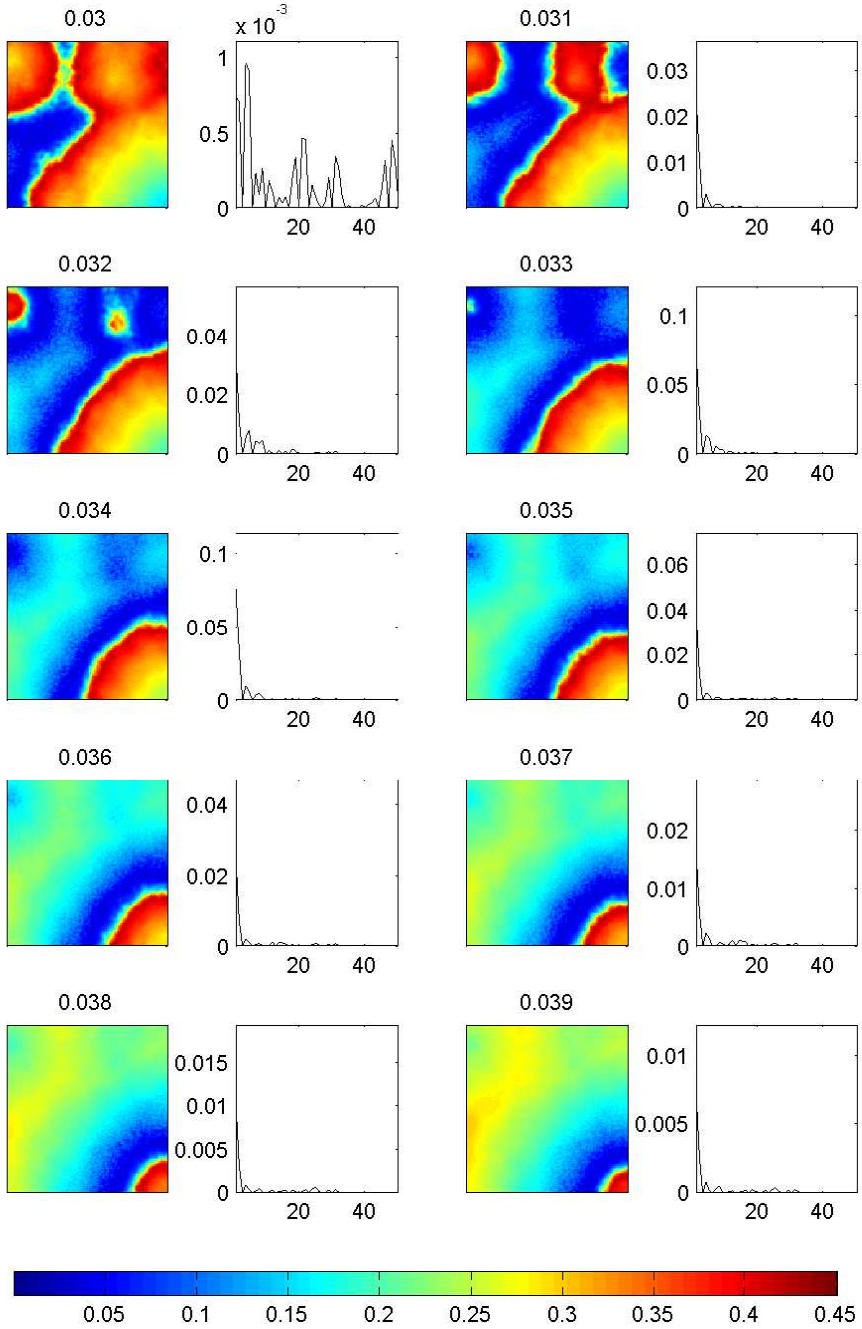

Figure 3.12: **Spatial dynamics for varying effective diffusivity**. Phytoplankton biomass field for (*columns 1 and 3*) and wavenumber spectra (*columns 2 and 4*) $n = 100$ at time $t = T_1 + T_2$, after initial integration of length $T_1 = 5,000$ days to remove transients and additional integration of length $T_2 = 500$ for calculation of diagnostics for $\varepsilon \in [0.04, 0.049]$ d^{-1}. Figure title numbers indicate value of ε.

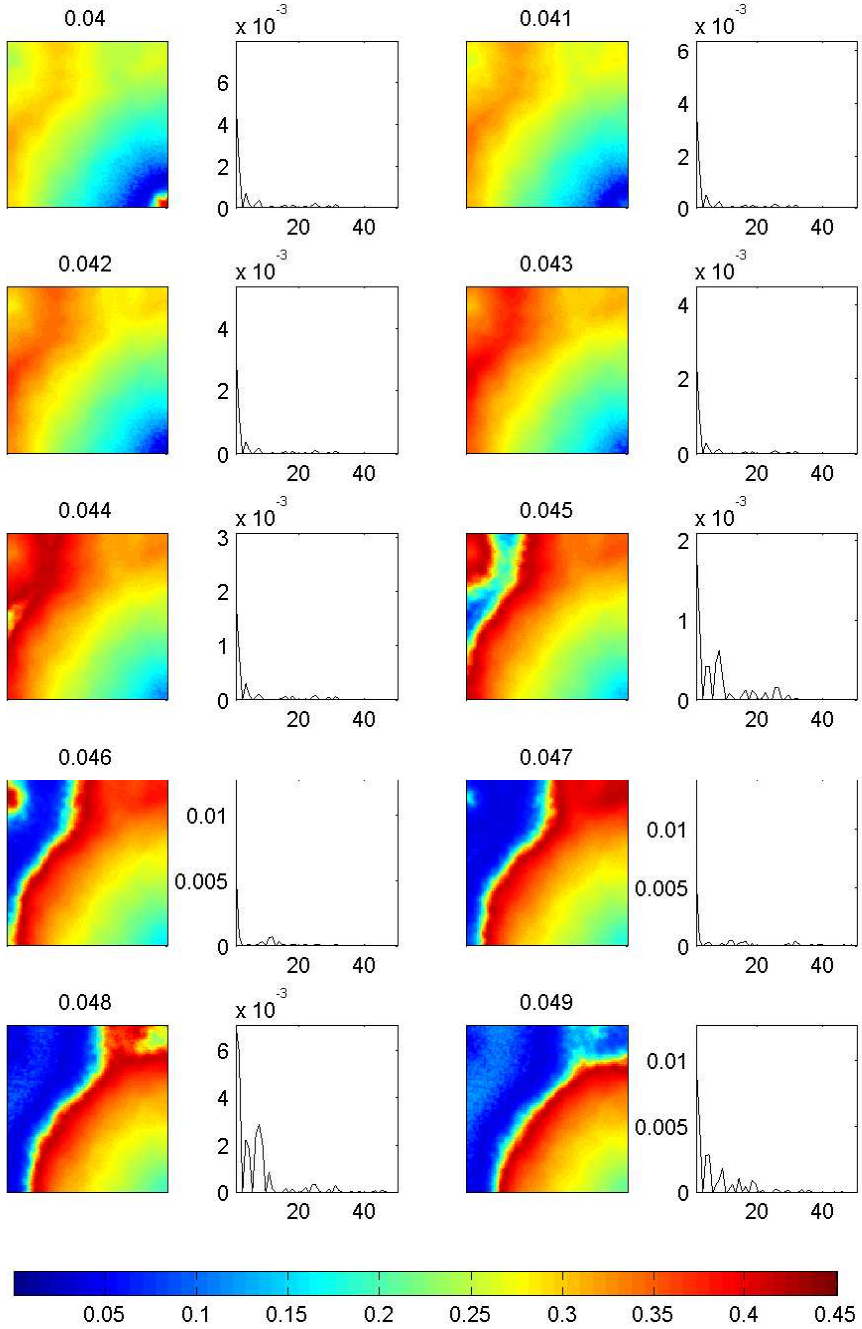

Figure 3.13: **Spatial structure diagnostics as a function of effective diffusivity**. Cluster size measures $c_x(\varepsilon)$ (*black*) and $c_y(\varepsilon)$ (*red*) and gradient measure $g(\varepsilon)$ for $n = 100$ at time $t = T_1 + T_2$, after initial integration of length $T_1 = 5000$ days to remove transients and additional integration of length $T_2 = 500$ for $\varepsilon \in [0, 0.05]$ d^{-1}. Frequency spread $\sigma(\varepsilon)$ is shown for reference (*dotted*).

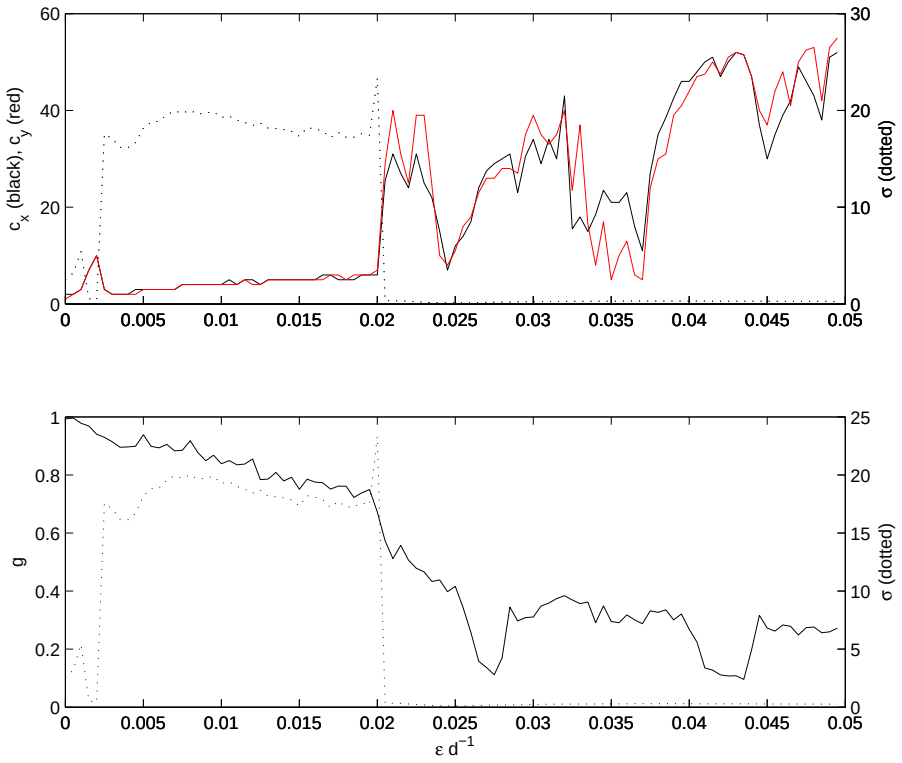

Figure 3.14: **Spatial structure as a function of effective diffusivity**. Cluster measures $c_x(\varepsilon)$ (*black*) and $c_y(\varepsilon)$ (*red*) scaled by grid-cell length-scale $l(\varepsilon)$ for $n = 100$ and $\varepsilon \in [0, 0.05]$ d^{-1}.

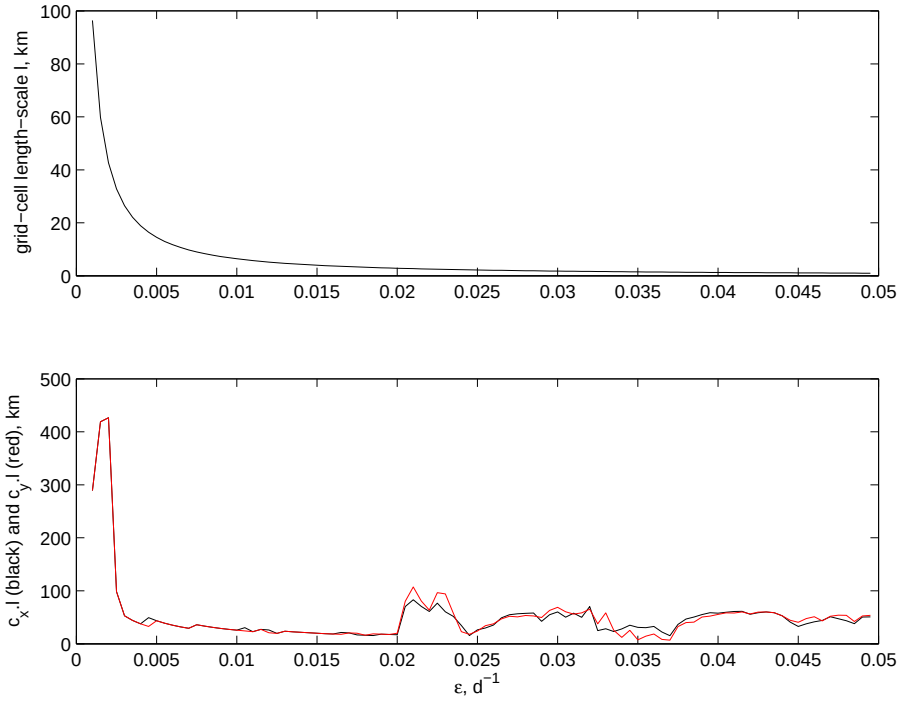

Figure 3.15: Distribution of frequencies $\omega_{i,j}$ as a function of coupling strength ε for $n = 100$. Figure title numbers indicate value of ε.

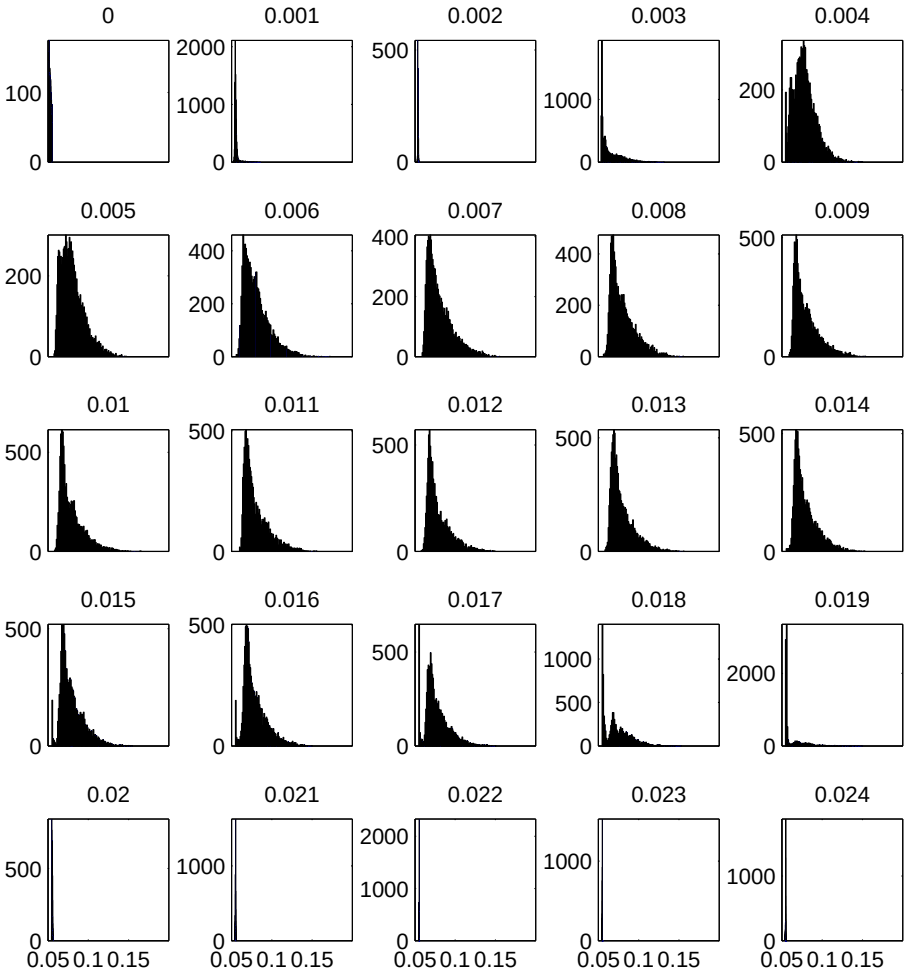

Figure 3.16: **Checking transition to frequency-locking.** Calculation of frequency disorder σ for $\varepsilon \in (0.0175, 0.0225)$ d^{-1} for length of integration $T_1 = 5000$ days (dotted line) and $T_1 = 20000$ days (solid line) for $n = 100$.

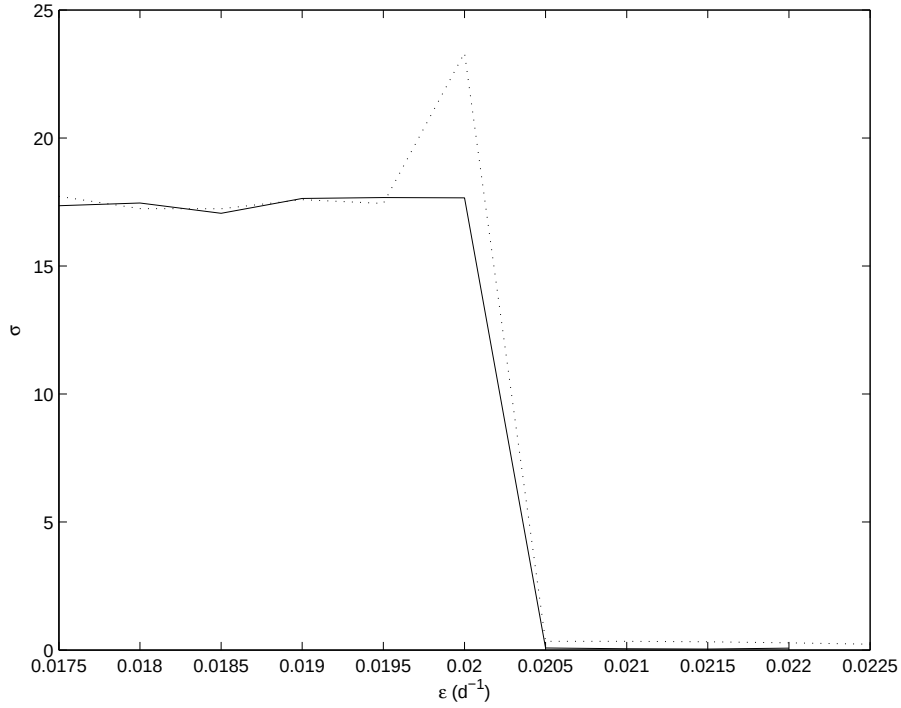

Figure 3.17: **Impact of boundary conditions.** Phytoplankton biomass and standard deviation σ of population frequencies as a function of coupling strength ε at time $t = 5000$ days after integration from homogenous initial conditions for $n = 100$ with doubly-periodic boundary conditions. $\sigma(\varepsilon)$ for the same system with no-flux boundary conditions is shown for comparison. Figure title numbers indicate value of ε. Colour scale is as in Figures 3.7 to 3.12.

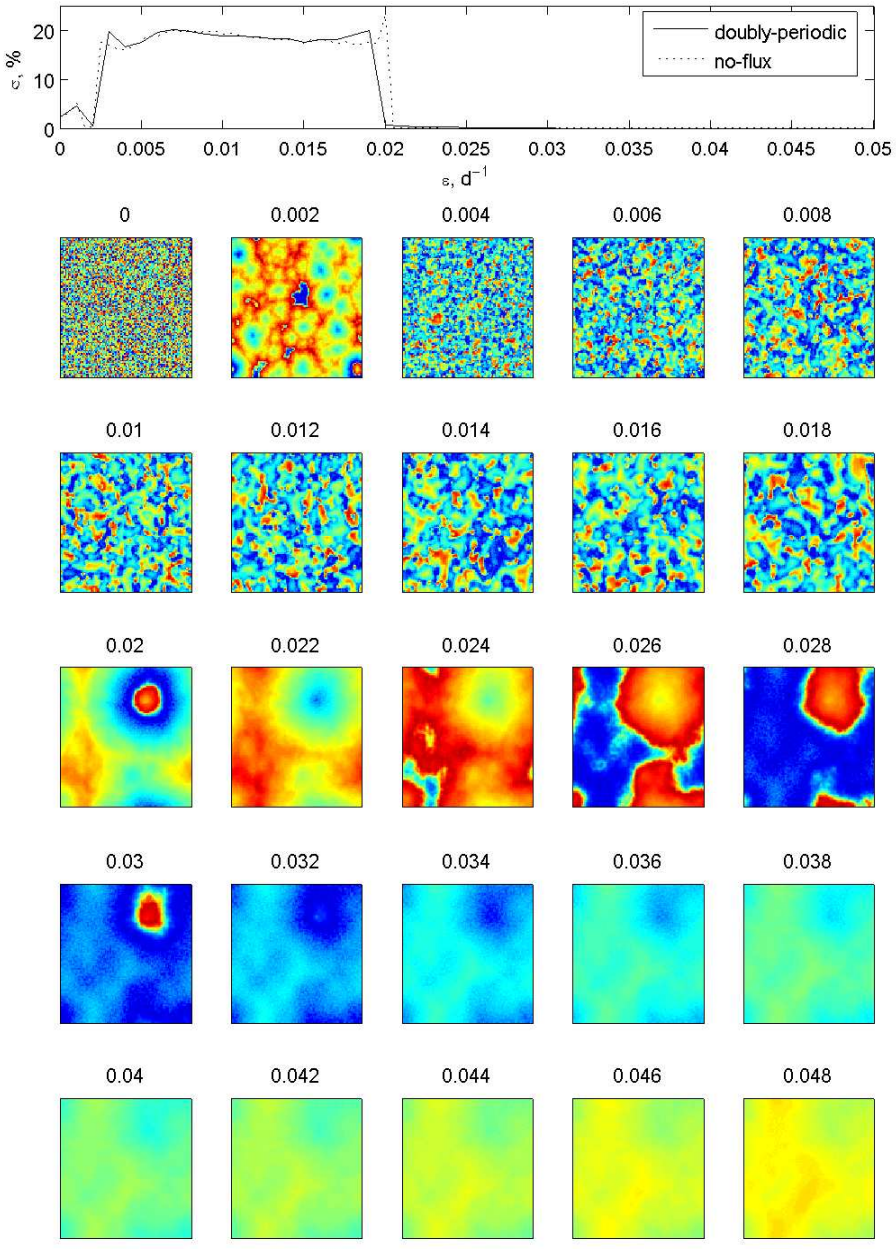

3.4 Dependence on model resolution

Following on from the previous section, we now consider the system from a different angle. Suppose we have a particular ocean region for which we wish to simulate plankton dynamics. In modelling this region, the spatial resolution chosen for the simulation may be decided by a number of different factors such as available computing power or the spatial resolution of observed data which we hope to reproduce. By fixing the domain size L of the lattice of interacting plankton populations and varying the number $n \times n$ of grid-cells, we can investigate how the behaviour of the system changes as the spatial resolution is increased.

Instead of fixing n and varying the effective diffusivity ε so that the grid-cell spatial scale and hence total domain length effectively varies, we now fix the domain size and consider varying the grid-cell length-scale l. As before, we consider the spatial mesoscale so that l varies from 1 km to 100 km. With this in mind, and in order to prevent the simulations becoming too computationally expensive, a domain size of 512 km is chosen. The number of grid-cells $n \times n$ is then given by $n \times n = \frac{L}{l} \times \frac{L}{l}$, covering a range of *whole*[2] grid-cells $[5 \times 5, 500 \times 500]$ grid-cells.

The domain size of 512 km was chosen for computational reasons. A domain size larger than 512 km leads to a larger number of grid-cells when considering a spatial resolution of 1 km than can be integrated in a reasonable length of time. Equally, a smaller domain size leads to too small a number of grid-cells when considering a spatial resolution of 100 km.

For each simulation with a particular number of grid-cells $n \times n$, we use the empirial Okubo relationship to set the coupling strength $\varepsilon\left(\frac{L}{n}\right)$ so that again $\varepsilon \in (0, 0.05]$ d^{-1} and the uncoupled case $\varepsilon = 0$ d^{-1} is included for completeness. As in the previous experiment, a mismatch spread $\Delta = 5\%$ is applied to the phytoplankton growth rate. Each simulation requires $n \times n$ phytoplankton growth parameter values

[2]Note that the domain length 512 km was also originally chosen to be consistent with some modelling work by A. P. Martin (*personal communication*); it was hoped to make some comparisons between that work and the present results. Although this line of research was not pursued, the domain length of 512 km rather than 500 km was retained and is accurately reported. This makes no difference to the results and merely leads to non-integer grid-cell length-scales.

$a_{i,j}$. The random mismatch values are not the same for all simulations, however, since a larger value of $n \times n$ calls for a larger number of mismatch values. These are generated for each simulation using the same integer seed for the random number generator and consequently, for each $n_2 > n_1$, the first $n_1 \times n_1$ values of $\{a_{i,j}\}$ for $n = n_2$ will be composed of the full set of $\{a_{i,j}\}$ of $n = n1$; the remaining $n_2^2 - n_1^2$ will be "new". Hence each simulation differs from the last not only in the number of grid-cells and resultant spatial resolution but also in the underlying set of natural frequencies (which are always uniformly distributed). The consequences of this will be discussed in Section 3.5.

As before, we have a number of diagnostic tools to give a clear picture of how changing the spatial resolution of the 512 km $\times$ 512 km model changes the kind of structure and synchronous effects exhibited.

Figure 3.18 shows how the spread of population frequencies and phase order parameter vary with n. For reference, the accompanying subplots indicate how the grid-cell length-scale $l = \frac{L}{n}$ and corresponding coupling strength ε, set as a function of l according to Okubo (1971), vary with n.

The cluster measures $c_x(n)$ and $c_y(n)$ in numbers of grid-cells, the cluster measures $c_x(n) \cdot l$ and $c_y(n) \cdot l$ scaled by the grid-cell length-scale $l = \frac{512}{n}$ km and the gradient measure $g(n)$ are plotted with varying n in Figure 3.19, with frequency spread σ shown as a dotted line for reference.

Figures 3.20 to 3.24 show final time-step spatial phytoplankton biomass and corresponding power spectra for each value of n, where the length of integration is 5,000 days to remove transients and a further 500 days for calculation of diagostics, as in the previous section. In the previous section the length of the domain was equal to the length-scale corresponding to each value of $\varepsilon \in [0, 0.05]$ d^{-1} according to Okubo (1971) relationship, multiplied by the 100 grid-cells; that is, $l \in [1, 100]$ km multiplied by 100. Here, the domain is of a fixed length, so that each of the lattice plots shown in these figures is of equal area.

Finally, to explain the patterns seen in Figures 3.20 to 3.24, Figure 3.25 shows how the frequency spread varies across the full range of $\varepsilon \in [0, 0.05]$ d^{-1} for $n = 20$, $n = 50$, $n = 80$ and $n = 140$. The values of $\varepsilon \left(\frac{512}{n}\right)$ set according to Okubo (1971), as

used in the calculations shown in Figure 3.18, are indicated by dashed lines. These plots are analogous to Figure 3.6 from the previous section, where we had $n = 100$. We see the same general shape of profile for each value of n for which the whole range of ε has been considered, as described in detail in the previous section. It is clear that the value of ε given by the Okubo relationship dictates which region of this profile is occupied by the dynamics for a given n when the domain length is fixed.

Using all this information together to understand how changing the spatial resolution affects the synchronous properties of the simulation of this fixed area, we see that there are essentially three regions of system-level dynamics.

- **$n < 20$: near frequency-locking; domain-scale structure; no phase-locking.** For very low n ($n < 20$), the low values of σ in Figure 3.19 indicate near frequency locking of the ensemble but the spatial plots in 3.20 clearly show that it is not fully phase-locked since there is a wide variation is phytoplankton biomass values. Spatial structure is large, with a peak in the power spectra at the domain-scale frequency. There is no distinct clustering: the cluster measure is equal to approximately $\frac{n}{2}$ in this region and the gradient measure is low, apart from at $n = 5$ where the very small number of grid-cells may have led to a misleading result.

  The (ε,σ) curve given in Figure 3.25 for $n = 20$ shows why this is so: the coupling strength fixed according to grid-cell length-scale $l = \frac{512}{20}$ km puts the dynamics into a frequency-locked region.

- **$20 \leq n < 290$: either frequency-locking or disorder possible; domain-scale structure or clustering.** For middle values of n ($20 < n < 290$), the system alternates between two distinct states, always with a sharp transition between the two.

  For most n in this range, the length-scale dependent coupling strength has pushed the dynamics into a desynchronised region, with frequency disorder $\sigma \approx 20\%$ and no phase synchrony. An example of this is given in Figure 3.25 for $n = 50$. Note also that the dynamics for $n = 100$, as described in detail in

the previous section, occupy this region when $L = 512$ km, since $\varepsilon\left(\frac{512}{100}\right) \approx 0.01$ (see Figure 3.6).

Within these non-frequency-locked parameter regions, there is a consistent increase in the cluster measures $c_x(n)$ and $c_y(n)$ grid-cells with n, indicating an increase in the number of grid-cells occupying a typical cluster, although the corresponding cluster size $c \cdot l$ decreases (see Figure 3.19). Spatial structure in these regions is small-scale, with clusters of size 3 to 10 grid-cells (40 km to 20 km) and sharp transitions between them, as shown by the high gradient measure values; $g(n) \approx 0.7 - 1.0$ (Figure 3.19).

These desynchronised parameter regions are interspersed with regions of frequency-locking, with $\sigma \approx 0$. Figure 3.18 shows $n = 140$ to occupy one of these frequency locked intervals, and the full (ε,σ) curve shown in Figure 3.25 explains why this is the case, since the value of coupling $\varepsilon(l)$ set according to grid-cell length-scale $l = \frac{512}{140}$ km is in the frequency-locked region.

The size of spatial structure seen in these frequency locked regions is much larger than in the desynchronised regions, with high values of $c_x(n)$ and $c_y(n)$ around 20 grid-cells or 70 km and low values of g around 0.5 (Figure 3.19). The spectra for these regions have peaks at the domain wavenumber (Figures 3.20 to 3.22).

Near transitions where increasing n moves the dynamics between the two states of (i) small-scale structure and frequency disorder and (ii) the large-scale structure and frequency-locking, we can see coexisting distinct areas of each scale of structure. For example, in Figure 3.21 we have large-scale structure for $n = 150$ and a combination of small and large for $n = 160$. As seen in the previous section, this is due to the need for longer integration times for transients to disappear near to unstable regions where we move from one type of dynamics to another.

The jumps in type of behaviour as n is varied between $n = 20$ and $n = 220$ region are caused by the interaction of three different factors. In general, an increase in n leads to an increase in the strength of coupling required for

frequency locking. We saw this for identical oscillators in Chapter 2 and it is hinted at again in the (ε, σ) curves for various n shown in Figure 3.25, although not conclusively (because there are other factors at work here too, which have not yet been discussed - see Section 3.5). However, the value of ε used in the simulation is set according the grid-cell length scale $l = \frac{L}{n}$ and it is seen in Figure 3.18 that this coupling strength increases with n. Hence the increase in number of grid-cells, which in general makes it harder for the system to synchronise, is in competition with the increase in coupling strength.

If these were the only two factors involved, we hypothesis that a critical number of grid-cells n_c would exist such that $\varepsilon\left(\frac{L}{n_c}\right) = \varepsilon_{FL}(n_c)$ so that for $n < n_c$ we would see one type of ensemble behaviour (small-scale clustering) for $n > n_c$ we would see another type of behaviour (frequency-locking; domain-sized structure). In other words, for n_c the two influences would be in balance. This assumes that only one point of intersection between the curves $\varepsilon\left(\frac{L}{n}\right)$ (as set by Okubo (1971)) and $\varepsilon_{FL}(n)$ exists.

The confounding third factor, which prevents us from determining the shape of the curve $\varepsilon_{FL}(n)$ is the variability in the natural frequencies of the individual grid-cells, as given by the mismatch values selected at random from a uniform distribution. It has been seen (Osipov and Sushchik, 1997) that changing the particular arrangement of natural frequencies which have the same probability distribution can alter the synchrony thresholds and hence emergent structure of a simulation. Osipov and Sushchik (1997) found that a larger strength of coupling was required to fully synchronise a chain of N oscillators with natural frequencies monotonically increasing along the chain than a chain with randomly distributed natural frequencies. They argue that in the case of ordered frequency mismatch the "pull" exerted on every oscillator by its two nearest neighbours is in opposition; it is sped up by the oscillator to the right and slowed down by the oscillator to the left, increasing the coupling required to overcome the natural frequency disorder.

- $n > 290$**: frequency-locking; increasing phase-locking; domain-scale structure.** For $n > 290$ grid-cells, the ensemble finally remains in the frequency-

locked region, with $\sigma \approx 0$ (Figure 3.18), large-scale structure and no well-defined clusters (Figure 3.19). High values of R, near 1, indicate an increase in the degree of phase-locking (Figure 3.18). This tells us that, of the competing influences of increasing number of grid-cells and increasing corresponding coupling strength, the increase in ε ultimately has the stronger influence.

There is a rapid decrease in c_x and c_y as n increases past 290, after which they stay at a value of 3 grid-cells (around 10 km) for increasing n. This indicates small-scale variability, but the low and decreasing values of $g < 0.5$ imply a gentle gradient across locally-synchronised regions rather than well-defined clusters, so that the c measure is unreliable (Figure 3.19). The wavenumber spectra for $n > 290$ indicate domain-scale dominant structure.

The amount of phase order increases with increasing number of grid-cells. This is seen in the phytoplankton biomass snap-shots of Figures 3.23 and 3.24 as an increasingly monotonous lattice plot and narrow spectrum, although some small-scale variability is still observed, accounting for the $c_x = c_y = 3$ grid-cells value. Evidently, for our domain of $L = 512$ km the largest coupling strength, which, set according to Okubo (1971), corresponds to the smallest grid-cell length-scale and therefore largest number of grid-cells into which the domain may be divided, is insufficient to pull the ensemble into full phase-locking.

We see that, as the number of grid-cells and resultant spatial resolution is increased, the final transition to frequency-locking occurs at higher values of ε. In other words, if this final transition occurs at $\varepsilon = \varepsilon_{FL}$ then, in general, ε_{FL} increases as n increases. This increase in the the difficulty of achieving full synchrony as n is increased is offset by the concurrent increase in effectively diffusive coupling strength $\varepsilon(l)$ as the resultant grid-cell length-scale l km decreases. In general, we have seen from the eventual permanent frequency-locking seen for large values of n in Figure 3.18 that the latter effect has the stronger influence on the ability of the system to synchronise.

For the domain considered here of $L = 512$ km, the system is not able to fully phase-lock. Bearing in mind our conclusions above, we hypothesize that it may be possible for a simulation with a *smaller* domain size to fully phase lock within the

range of grid-cell length-scales considered here. This is because the largest value of $\varepsilon(l)$ corresponds to the smallest grid-cell length-scale, which here is fixed as 1 km. On the other hand, the corresponding number of grid-cells $n \times n = \frac{L}{1} \times \frac{L}{1}$ decreases with the size of domain L and we have seen that a smaller number of grid-cells is able to synchronise more readily. We therefore suggest that for a small enough domain size and correspondingly small number of grid-cells, the value of coupling $\varepsilon(l)$ for $l = 1$ km would be sufficient to phase lock the ensemble.

The factor not yet fully explored is the impact of the underlying disorder in parameter values. We will see that the particular values of ε at which the transitions between the different types of system behaviour occur vary widely with the particular choice and arrangement of the natural frequencies of the populations. It is the resultant variability in the critical values of ε that causes the system with fixed domain size and varying spatial resolution to "jump" back and forth between the two discrete system states (as seen in Figure 3.18) as n is increased.

Figure 3.18: **Diagnostics for L=512 km as a function of number of grid-cells**. Spread in frequencies σ (*solid line*) and order parameter R (*dashed line*) as a function of number of grid-cells, $n \times n$, for $L = 512$ km. Showing also coupling strength $\varepsilon\left(\frac{L}{n}\right)$ and grid-cell length-scale $l = \frac{L}{n}$.

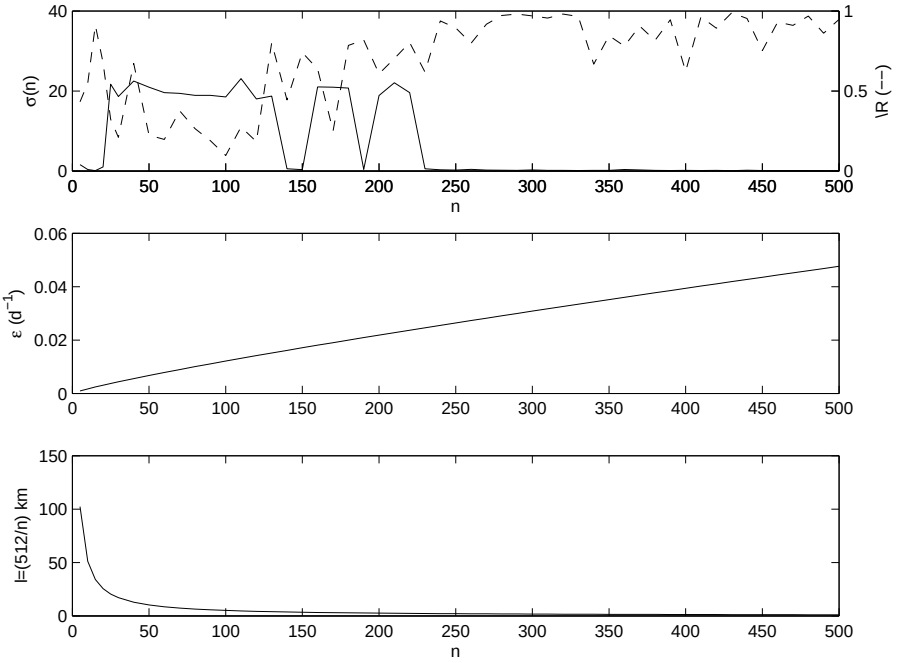

Figure 3.19: **Spatial structure diagnostics as a function of number of grid-cells**. Cluster measures $c_x(n)$ (*black*) and $c_y(n)$ (*red*) (*top panel*), cluster measures scaled by grid-cell length-scale (*middle panel*) and gradient measure $g(n)$ (*bottom panel*) for $L = 512$ km and $n \in [5, 500]$. Dotted line shows spread in frequencies $\sigma(n)$ for reference.

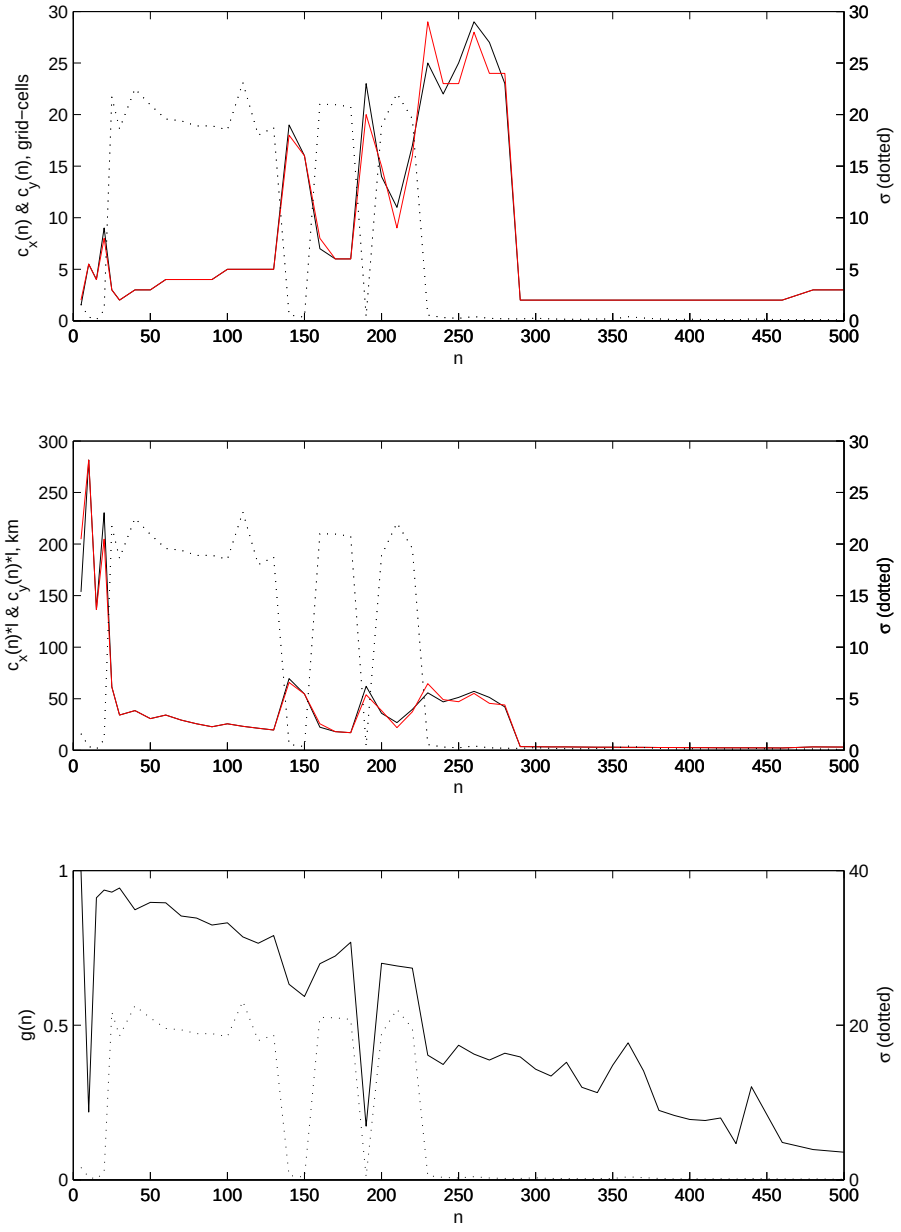

Figure 3.20: **Spatial structure for varying spatial resolution**. Phytoplankton biomass in gC m^{-3} (*columns 1 and 3*) and wavenumber spectra (*columns 2 and 4*) after integration length 5,500 days from homogeneous initial conditions for domain length $L = 512$ km and number of grid-cells $n \in [0, 70]$.

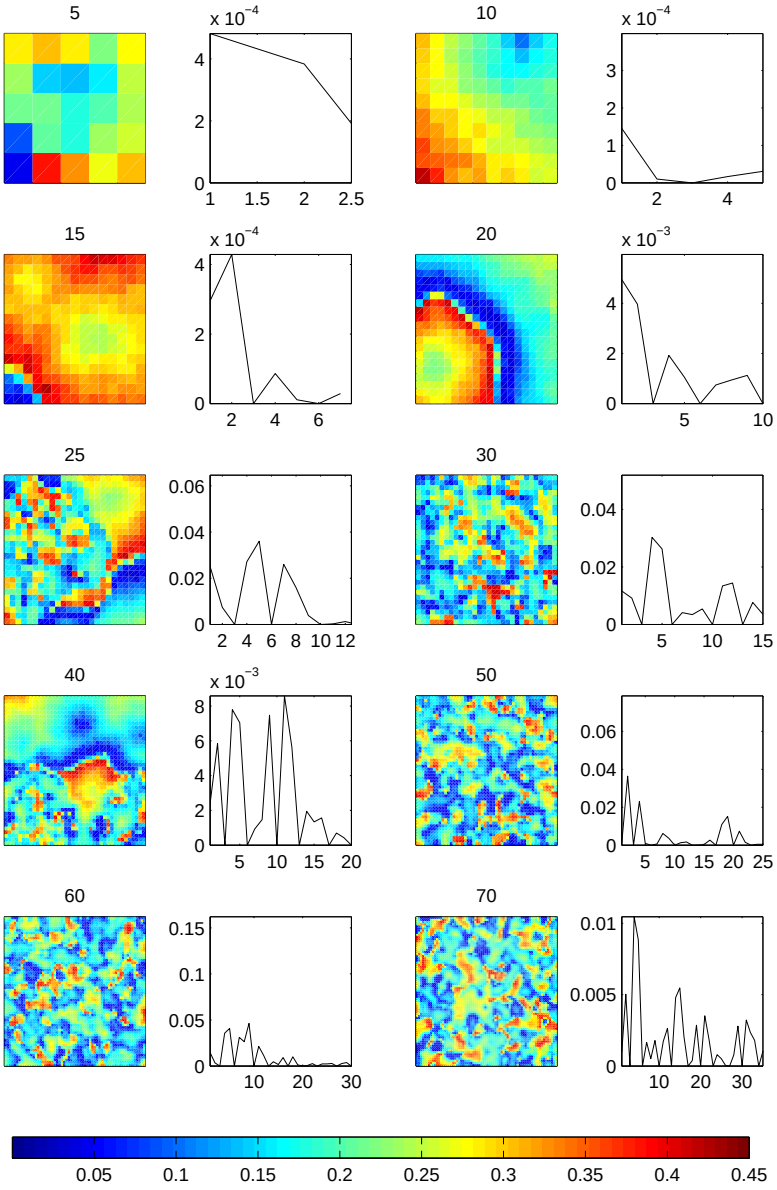

Figure 3.21: **Spatial structure for varying spatial resolution**. Phytoplankton biomass in gC m^{-3} (*columns 1 and 3*) and wavenumber spectra (*columns 2 and 4*) after integration length 5,500 days from homogeneous initial conditions for domain length $L = 512$ km and number of grid-cells $n \in [80, 170]$.

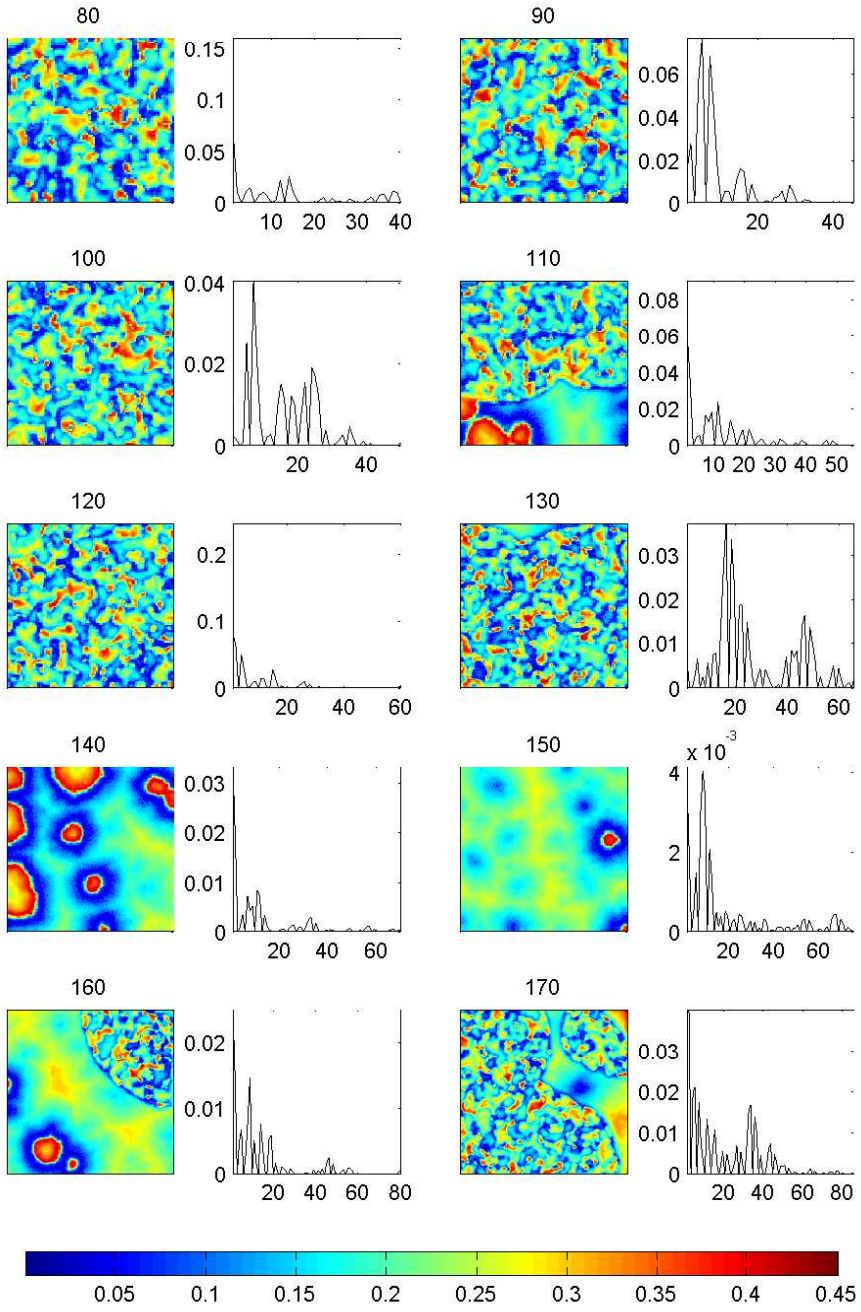

Figure 3.22: **Spatial structure for varying spatial resolution**. Phytoplankton biomass in gC m^{-3} (*columns 1 and 3*) and wavenumber spectra (*columns 2 and 4*) after integration length 5,500 days from homogeneous initial conditions for domain length $L = 512$ km and number of grid-cells $n \in [180, 270]$.

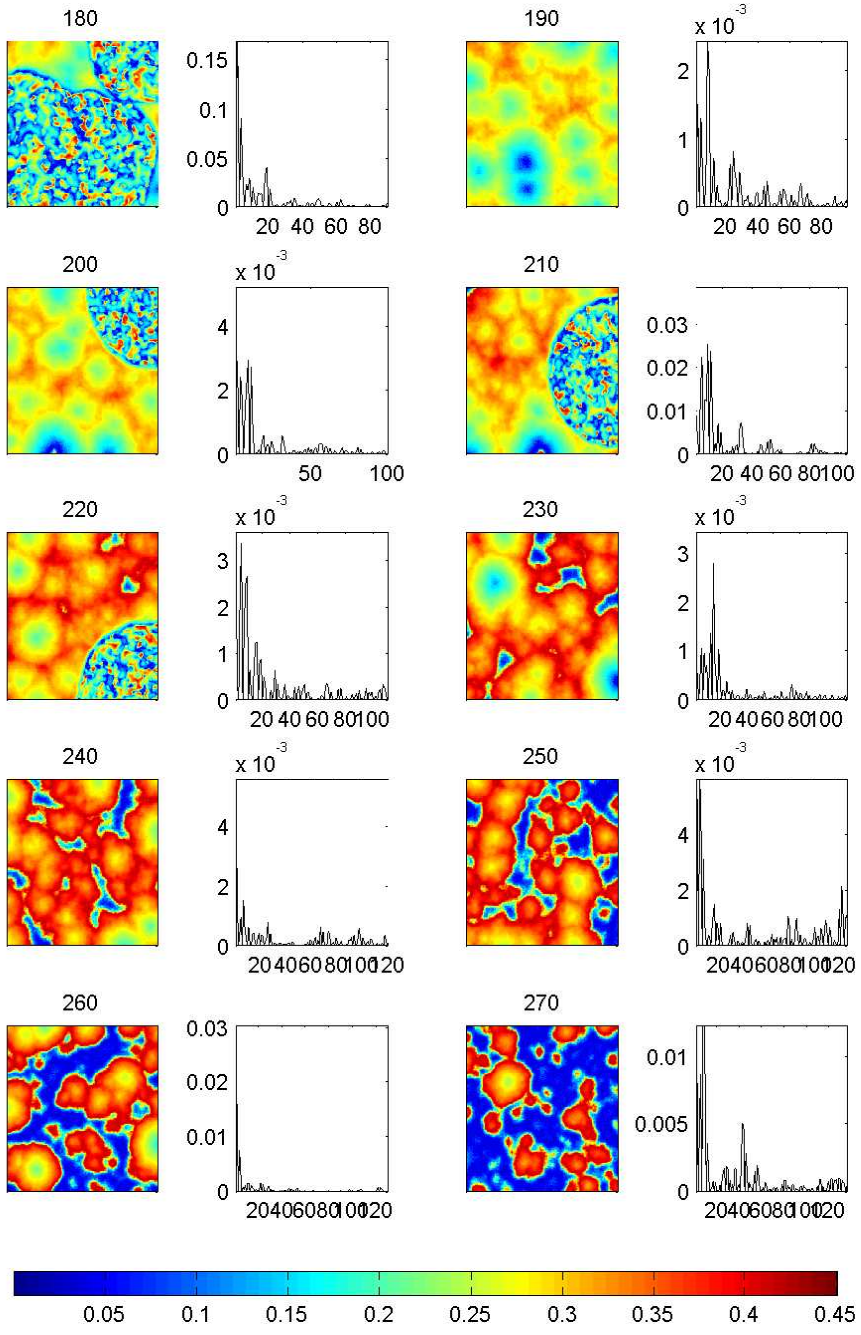

Figure 3.23: **Spatial structure for varying spatial resolution**. Phytoplankton biomass in gC m^{-3} (*columns 1 and 3*) and wavenumber spectra (*columns 2 and 4*) after integration length 5,500 days from homogeneous initial conditions for domain length $L = 512$ km and number of grid-cells $n \in [280, 370]$.

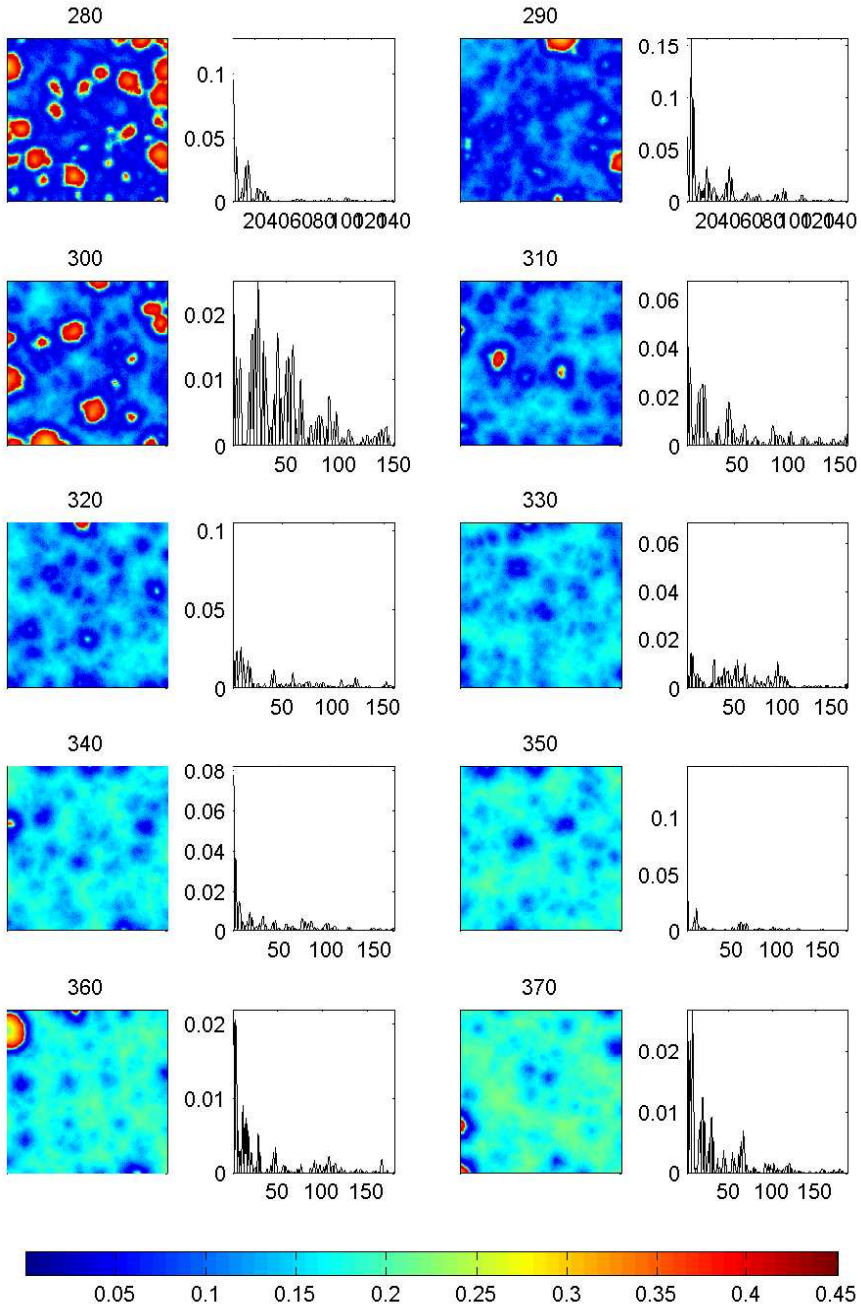

Figure 3.24: **Spatial structure for varying spatial resolution**. Phytoplankton biomass in gC m^{-3} (*columns 1 and 3*) and wavenumber spectra (*columns 2 and 4*) after integration length 5,500 days from homogeneous initial conditions for domain length $L = 512$ km and number of grid-cells $n \in [380, 500]$.

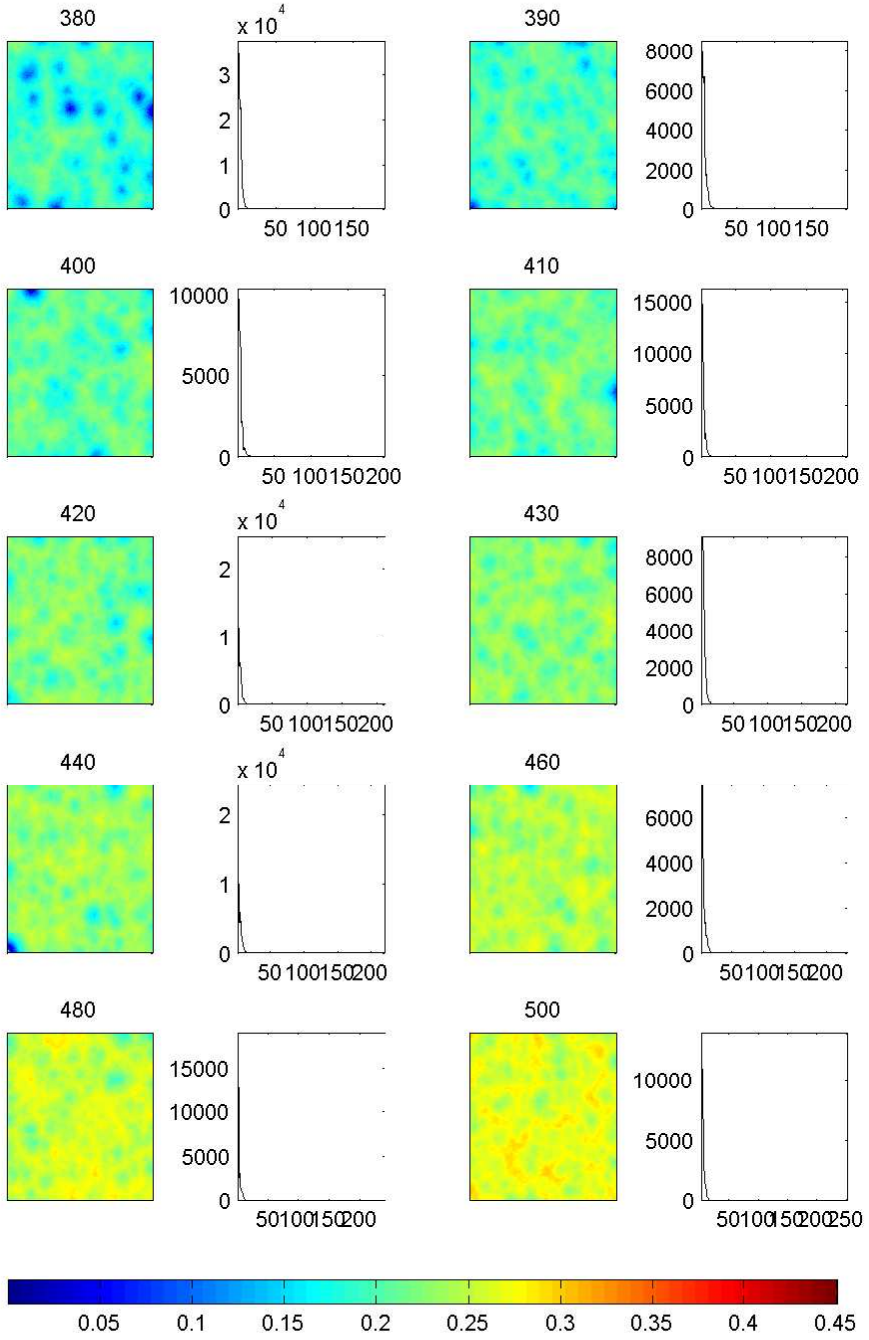

Figure 3.25: **Examples of spread in frequencies as a function of effective diffusivity for different numbers of grid-cells**. $\sigma(\varepsilon)$ for n=20, 50, 80 and 140. The values of effective diffusivity $\varepsilon\left(\frac{L}{n}\right)$ for $L = 512$ km set according to the spatial resolution are indicated by dashed lines.

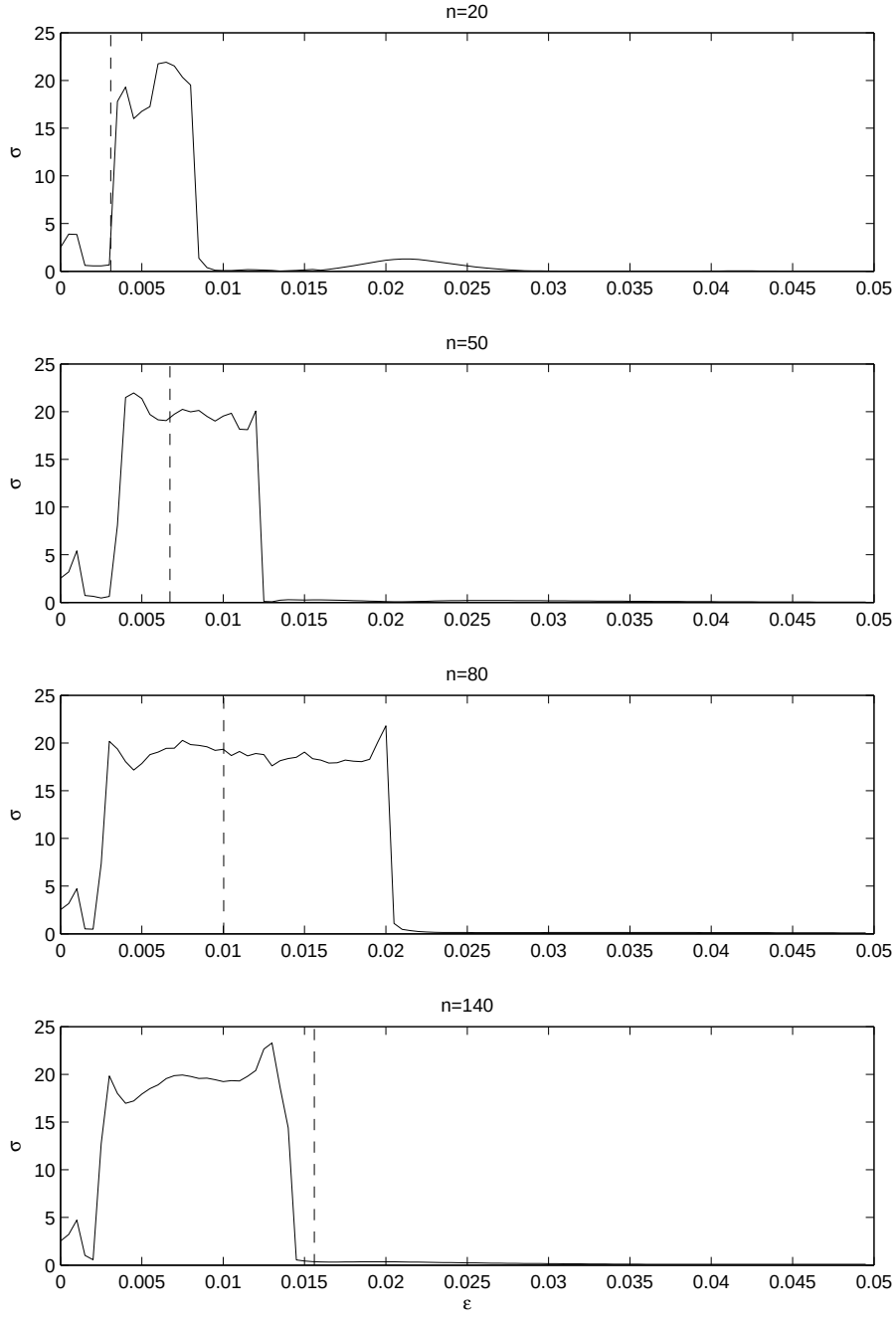

3.5 Investigation of variability

Motivated by the findings of the previous section, we examine the influence of the particular choice and spatial arrangement of natural frequencies from the same uniform distribution on the ability of the ensemble to synchronise.

In order to isolate the influence of the arrangement of the frequency disorder from the two influences of the changing number of grid-cells and concurrently changing the effective diffusivity, we fix the number of grid-cells and look at the full range of mesoscale diffusivity $\varepsilon \in [0, 0.05]$ d^{-1} as in Section 3.3. The spread in natural frequencies is fixed at $\Delta = 5\%$ and the $n \times n$ phytoplankton growth rate values $\{a_{i,j}\}$ are selected at random with a uniform distribution, as before. The random number generator requires an integer seed J, so that the same J gives the same set of mismatch values for a fixed n. Here, we vary J from $J = 1$ to $J = 100$ to give 100 sets of mismatch values, all with the same probability distribution. Each of these sets is then used in the integration of the phytoplankton dynamics and the resultant $\sigma(\varepsilon)$ is calculated for $\varepsilon \in [0, 0.05]$. Hence we have an ensemble of 100 simulations differing only in the particular choice and arrangement of natural frequencies.

For computational speed, it has been necessary to restrict this investigation to $n = 10$ since carrying out 100 different simulations for a lattice of greater than 10×10 populations is very time-consuming.

Figure 3.26 shows the calculations of the spread in frequencies σ as a function of coupling strength between grid-cells ε for each of the 100 simulations. Although this figure indicates the large amount of variability in the profiles, there are some noteworthy common features. For each simulation, the initial part of the profile, for low ε in the range approximately 0 to 0.001 d^{-1}, shows an increase in frequency spread to about double the natural frequency disorder $\sigma(\varepsilon = 0)$ and a subsequent sharp decrease in frequency spread at $\varepsilon \approx 0.002$ d^{-1}, i.e. at the same value of ε for each profile. Qualitatively, with some variation in the actual values of $\sigma(\varepsilon)$, this part of the profile, which was also seen for $n = 100$ in Section 3.3 (Figure 3.6) and in Section 3.4 for n =20, 50, 80 and 140 (Figure 3.25), is the same for all simulations. For $\varepsilon > 0.002$ the results diverge into two distinct types of profile: (1) as seen in the previous sections, there is a bursting out of frequency-locking at

some value of ε into a desynchronised region with values of σ around 20% and an eventual rapid return to frequency-locking at some coupling strength ε_{FL}, or, (2) the system remains frequency locked. Some illustrative examples of this are given in Figure 3.27. All simulations become permanently frequency-locked for sufficiently high effective diffusivity, i.e. $\varepsilon_{FL} < 0.05$ d^{-1} $\forall$ J.

Clearly, whether or not a region of desychronisation occurs, and for what range of ε it persists, depends on the particular mismatch values used in the simulation. The coupling strength ε_{FL} at which there is a transition to permanent frequency-locking ranges from 0.002 to 0.023 d^{-1}. Why is there such a spread in ε_{FL} when we have a spread in phytoplankton growth rates of $\Delta = 5\%$ and with the same probability distribution for each simulation? Firstly, we note that although $\Delta = 5\%$ for each simulation, the resultant spread in natural frequencies, as given by $\sigma(\varepsilon = 0)$ varies from 2.3% to 2.9% with J (see Figure 3.28). We might hypothesise that a spread in natural frequencies at the lower end of this range would lead to a profile without a desynchronised region, since presumably populations with smaller natural frequency discrepancy would synchronise more readily. However, the scatter plot of natural frequency disorder against maximum frequency disorder obtained for $\varepsilon \in [0, 0.05]$ (see Figure 3.29) shows this hypothesis to be false. Here we clearly see the two distinct profiles as two discrete clusters, one at a maximum σ value around 20% and one at around 5%, but there is no obvious correlation between natural frequency disorder and whether the system exhibits the desynchronised region or not. Hence, it is the actual arrangement of natural frequencies of plankton populations in the lattice that determines the synchronous properties. This could be investigated further by applying a specified spatial arrangement of frequencies, e.g. monotonically increasing across the domain, a line of research not explored further in the present study.

We see that the system may exhibit a range of behaviour for a fixed value of the coupling strength ε depending on the set of growth rate parameters $\{a_{i,j}\}$. For the system of 10×10 populations, if we fix the domain size L then we fix the effective diffusivity according to the grid-cell length-scale l given by $\frac{L}{10}$. Consider the four cases of $L = 512$ km, $L = 150$ km, $L = 100$ km and $L = 50$ km, giving grid-cell

length-scale $l = 51.2$ km, $l = 15$ km, $l = 10$ km and $l = 5$ km, respectively, and, by the empirical Okubo relationship between length-scale and effective diffusivity, $\varepsilon = 0.0017$ d^{-1}, $\varepsilon = 0.0049$ d^{-1}, $\varepsilon = 0.007$ d^{-1} and $\varepsilon = 0.012$ d^{-1}, respectively. The values of ε are indicated by red lines in Figure 3.26. Histograms of the values of σ calculated at these values of ε for each of the 100 simulations of 10×10 populations are shown in Figure 3.30. These results show that the kind of spatial dynamics observed in the simulation will depend upon the particular values and arrangement of natural frequencies. In particular, for a domain size of $L = 150$ km, $L = 100$ km or $L = 50$ km, sometimes frequency-locked dynamics with large-scale structure (see previous section) and sometimes desynchronised dynamics with small-scale clustering will result (Figure 3.30), even though the domain size L, number of populations $n \times n$, parameter mismatch Δ, the choice of biological model F used to represent plankton dynamics and the strength ε of interaction between populations are all fixed. As the domain size is decreased, the corresponding ε increases and hence the dynamics are more likely to inhabit a frequency-locked region.

Figure 3.26: **Ensemble runs**. Frequency disorder σ as a function of coupling strength ε in d^{-1} for $n = 10$ for 100 different sets of phytoplankton growth parameter values $a_{i,j}$ for $i, j = 1, \ldots, 10$, uniformly distributed on an interval of width $\Delta = 5\%$ centred on a_0. Each set seeded by a different integer J. Red lines indicate the value of effective diffusivity for grid-cell length-scale $l = \frac{L}{10}$ for four different domain sizes: $L = 512$ km, $L = 150$ km, $L = 100$ km and $L = 50$ km (see Figure 3.30).

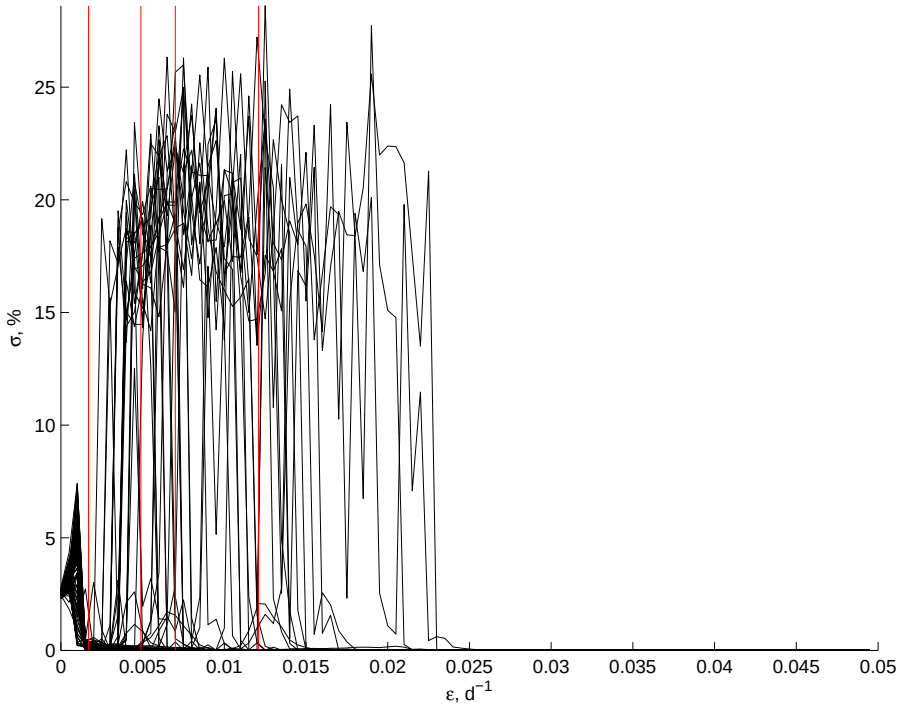

Figure 3.27: **Typical profiles**. Frequency disorder σ as a function of coupling strength ε for $n = 10$ for four different seeds.

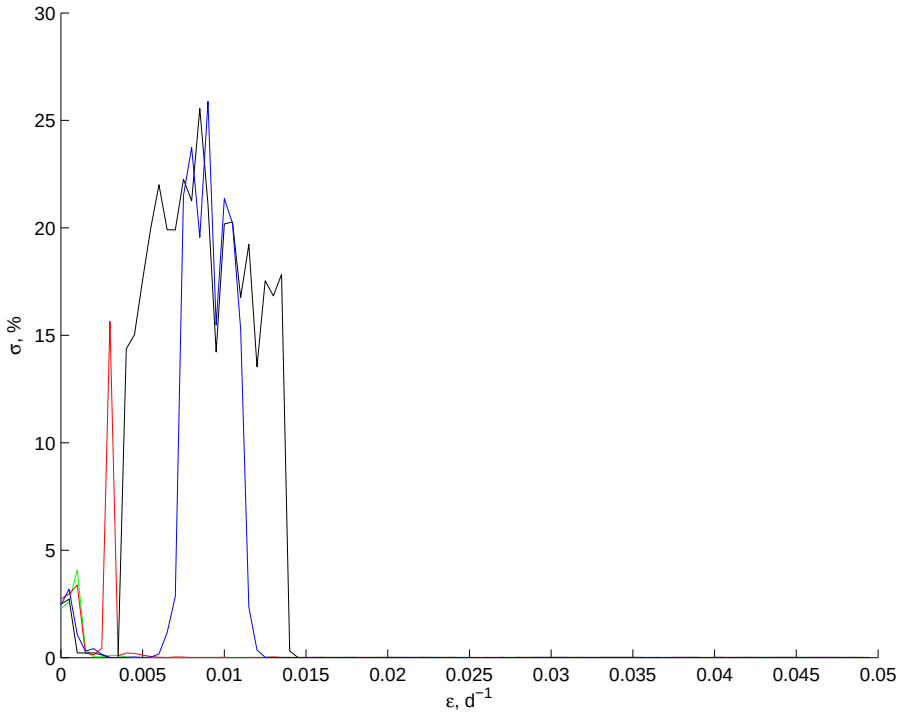

Figure 3.28: **Natural frequency disorder**. Histogram of the spread in natural frequencies $\sigma(\varepsilon = 0)$ for 100 simulations with $n = 10$. For each simulation, a different integer seed is used in the random number generator to obtain the set of phytoplankton growth parameters $a_{i,j}$.

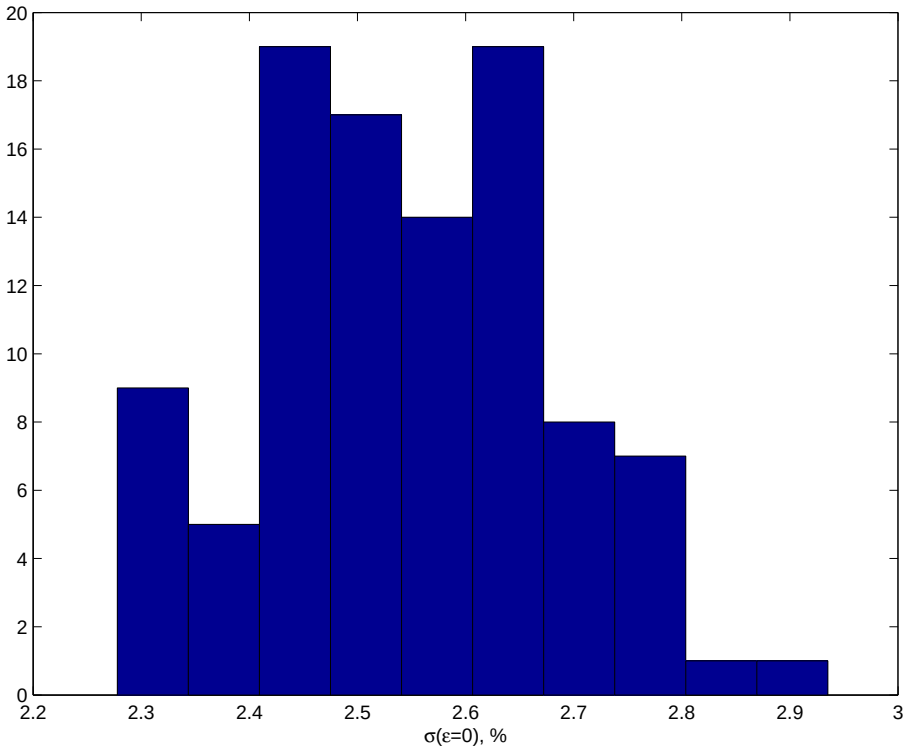

Figure 3.29: **Relating maximum to natural frequency spread**. Relationship between maximum frequency spread σ for $\varepsilon \in [0, 0.05]$ and natural frequency spread $\sigma(\varepsilon = 0)$ for an ensemble of 100 simulations with $n = 100$ and a different integer seed used in the random number generator to obtain the set of phytoplankton growth parameters $a_{i,j}$ for each simulation.

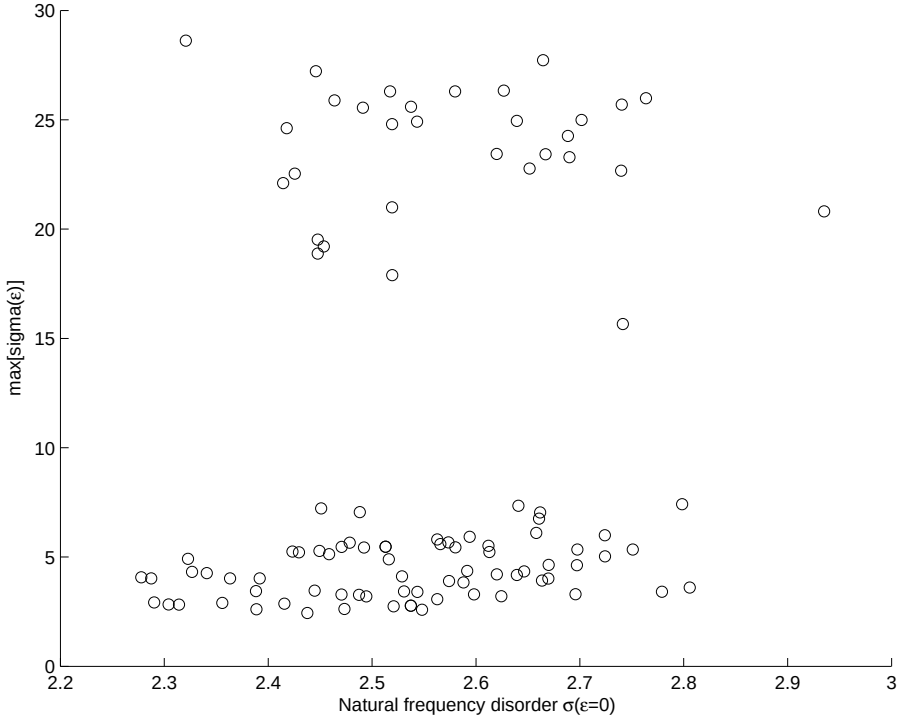

Figure 3.30: Histogram of frequency disorder σ calculated at $\varepsilon = \varepsilon(L/10)$ for a domain size $L = 512$ km, $L = 150$ km, $L = 100$ km and $L = 50$ km (see Figure 3.26) for 100 differently-seeded simulations with $n = 10$.

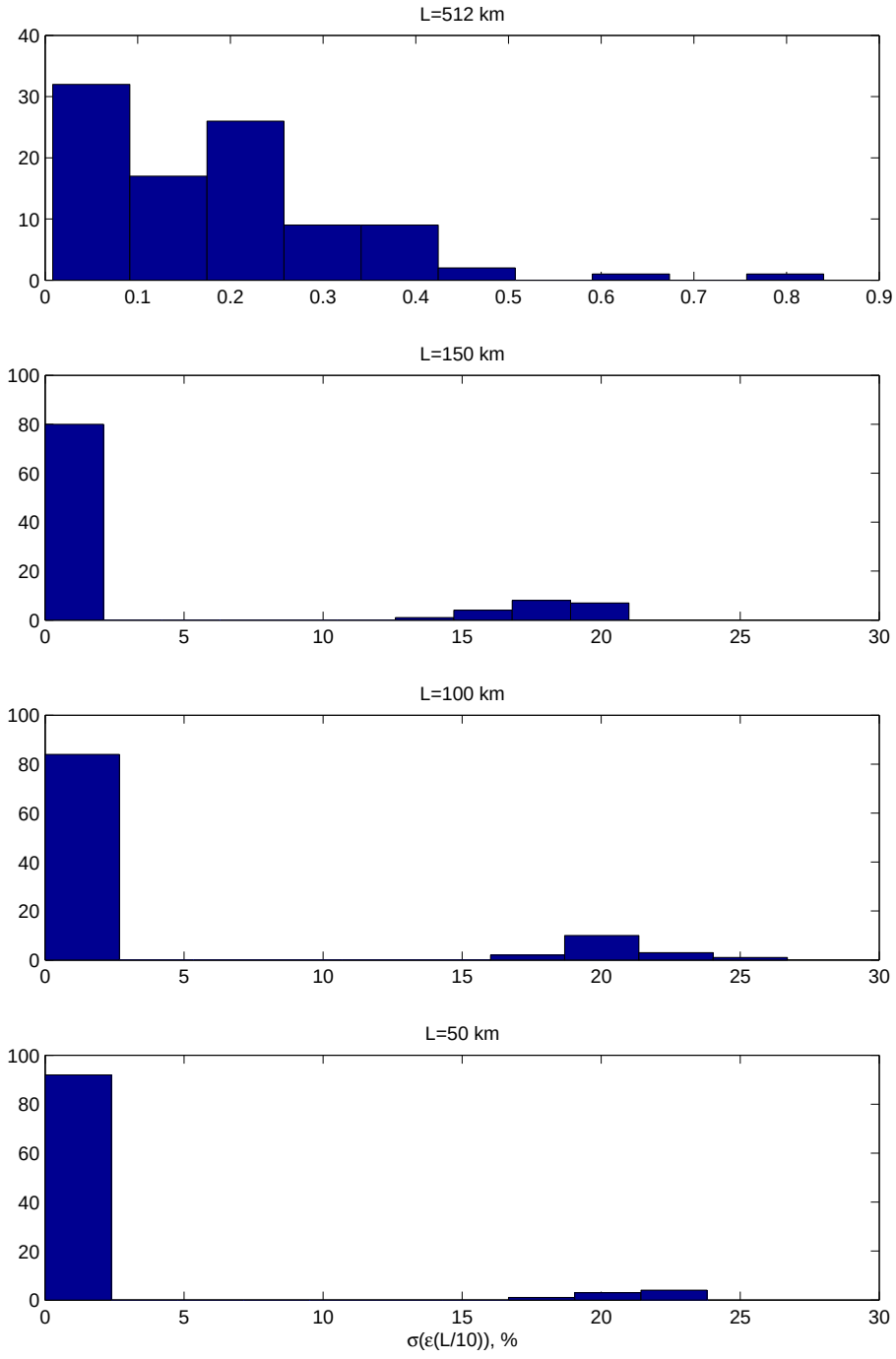

3.6 Discussion

A basic model of a lattice of $n \times n$ interacting non-identical plankton populations, each represented by the same NPZ model but with random mismatch in the phytoplankton growth rate parameters used in the biological model, has been used to investigate several aspects of the dynamics of a spatially-varying plankton distribution. To summarise these experiments: the effect of varying effective diffusivity has been considered by fixing the number of grid-cells and varying the coupling strength between grid-cells; the effect of model resolution has been considered by fixing the domain size L km $\times$ L km and varying the number of grid-cells and therefore grid-cell spatial scale; and the effect of variation in the parameter disorder values has been explored by carrying out a number of simulations with differently-seeded random mismatch values. The experiments have shown that altering the strength of interaction, number of grid-cells, domain size or underlying parameter disorder alters the emergent structures of the plankton simulation.

An increase in the strength ε of grid-cell interaction does not automatically lead to an increase in the observed synchrony, even when all other factors mentioned are kept fixed. Remarkably, interaction between the populations has been shown for intermediate coupling strengths to *increase* the frequency disorder by an order of magnitude compared with the natural frequency disorder. This system state manifests as small-scale local synchrony (clustering).

Eventually, as the coupling strength ε is increased, intuitive behaviour returns and the system locks into frequency synchronisation at a critical value of coupling $\varepsilon = \varepsilon_{FL}$. Importantly, although there is a gradual increase in cluster size within the intermediate coupling regime, the transition to domain-sized structure is not continuous, but alters abruptly at the threshold coupling strength. This system state is characterised by a frequency disorder close to zero, domain-scale structure and gentle gradients in plankton biomass between grid-cells.

As various factors such as number of grid-cells or choice of parameter mismatch values are varied, the phytoplankton distribution flips discontinuously between these two qualitatively different states.

On the other hand, once frequency locking is achieved and persists, the transition

to full phase-locking is in general slow and steady, with increasingly homogeneous spatial dynamics as ε is increased or number of grid-cells decreased.

There are consequences of these results for ocean modelling studies. Once again we encounter the problem of model resolution: this section has shown that the emergent features of a modelled plankton distribution can alter discontinuously at a threshold number of grid-cells.

Where this threshold occurs has been shown to vary with the competing influences of increasing n and the corresponding increase in ε set according to the empirical relationship between length-scale and effective diffusivity (Okubo, 1971), plus the variability caused by the mismatch in underlying population dynamics, causing intermittency in which kind of emergent structure is observed. Altering the spatial resolution of a spatially varying model of plankton distribution could therefore have unpredictable consequences for the model results and, importantly, for the conclusions and predictions drawn from them.

It has been seen that even when domain size, number of grid-cells, biological model, and size and probability distribution of parameter mismatch spread are all fixed, a huge amount of variability in the synchronisation thresholds can still be caused by changing the particular arrangement of natural frequencies. Clearly this is problematic for biological modelling of spatially varying distributions, but what might this study tell us about the impact of natural variability on plankton distributions in the ocean? We can deduce that for the same amount of observed variability in a particular biological parameter, the cause and therefore spatial arrangement of this variability might differ, in which case the synchronous effects observed might also differ. Taking the case of spatial variability in the phytoplankton growth rate, such variability might be caused by, for example, varying water temperatures or underlying differences in species composition. If the former were true then we could imagine a monotonic horizontal temperature gradient across the area of ocean, leading to an ordering in the resultant natural frequencies across the gradient. The latter case might lead to a more disordered arrangement of frequency mismatch. The results of this section would lead us to expect the observed synchronous effects to differ between these two cases. Further work could look at arranging the frequency

disorder across the lattice to investigate these two cases.

Near to the observed sharp transitions in system behaviour, we have seen that very long transients are required for steady-state dynamics to become established. Even away from the transition points, the transient integration times are long; here we have used 5000 days. The necessity of these long transient times brings into question the relevance of the steady-state dynamics observed here to real-world ocean observations. In reality, the structure caused by these synchrony effects would be constantly disturbed by advection so that steady-state dynamics may be unable to establish themselves. The transient behaviour observed in, for example, Figure 3.3, where in some cases we have an interesting coexistence of the two different scales of dynamics, might be more relevant to real-world plankton dynamics in an ever-shifting ocean. Note, however, that much of the steady-state spatial structure emerges early on in the integration, e.g. emergence of coherent clusters by $t = 1000$ days (Figure 3.3). Additionally, although the biological model parameters have been selected from a region of parameter space leading to oscillatory dynamics, they have not been "tuned" to give a particular period of oscillation, and so the long integration time is not a reason to discount the results.

Chapter 4

Influence of advection

4.1 Introduction

In this chapter, we investigate the robustness of our previous results to the inclusion of stirring of populations at spatial scales larger than the grid-cell. A simple representation of advection allows us to gain insight into the relevance of our results to real-world plankton distributions. To this end, a linear shear is applied to the lattice of populations, causing advection of rows of populations with respect to one another. In all other aspects, the distribution is modelled as in Chapter 3, with $n \times n$ non-identical populations each represented by the NPZ model of Steele and Henderson (1981) and interacting via a nearest-neighbour coupling of strength ε. Since the advection causes the rows to become misaligned, however, the nearest-neighbours of each plankton population alter with time. This will be fully described in Section 4.2.

This set up will be used to investigate how the results of the previous chapter ae modified by shear of increasing strength. These results will be more relevant to regions of high shear in the ocean, whereas the previous chpater was representative of regions of negligible shear.

Specifically, we determine the influence of advection on the ability of the lattice of populations to stably sychronise and upon the emergent spatial structure observed. By varying the *rate* of shear in the simulation, we can explore the importance of advection, with respect to the other biological and physical processes governing

evolution of the populations, in setting this structure.

4.2 Methods

As in previous chapters, we consider a lattice of $n \times n$ non-identical plankton populations, each represented by the NPZ model SH81 (Steele and Henderson, 1981). Biological model parameters are as in Chapter 3 with a random mismatch of spread $\Delta = 5\%$ applied to the default phytoplankton growth rate a_0 to obtain phytoplankton growth rates making a uniform distribution centred on a_0. Previously, interaction between populations was provided by a nearest neighbour effective diffusivity term. In this chapter, we retain the effective diffusivity and introduce an explicit advection, resulting from a constant shear

$$\frac{\partial u}{\partial y} = -\kappa$$

(where the positive y-axis is defined as distance from the top edge of the lattice) with κ in units of d^{-1} so that the velocity u in the x-direction varies linearly with y.

In our spatially discrete model, this means that row i moves at a velocity

$$\kappa \times l \text{ km d}^{-1}$$

with respect to row $i+1$, where l is the grid-cell lengthscale, so that in implementation the velocity profile is a step function. This is shown schematically in Figure 4.1. Arbitrarily, we set $u = 0$ for the top row; the choice of stationary row may be varied by adding a suitable constant velocity to each row. Boundary conditions are singly periodic to allow leaving advected material to re-enter the area at the opposite edge; no-flux boundary conditions are imposed at the top and bottom edges.

4.2.1 Implementation

The code used for the integration of the mixing-only system considered in Chapter 3 was adapted for the addition of shear. The implementation of the described shear requires that the rows of the lattice travel at different speeds and therefore become

misaligned. At each time-step of length dt days, each row i is shifted with respect to row $i+1$ by a distance $\rho \times l$ where $0 < \rho < 1$. This is shown schematically in Figure 4.2. The fraction of a grid-cell moved at each time-step is set according to the required rate of shear:

$$\kappa = \frac{\partial u}{\partial y} = \frac{\rho l/\mathrm{dt}}{l} = \frac{\rho}{\mathrm{dt}}$$

$$\Rightarrow \rho = \kappa \times \mathrm{dt}.$$

The misalignment between rows causes the population $v_{i,j}$ in row i and column j to interact with a varying set of at most six nearest neighbours rather than the usual fixed four neighbours (see Figure 4.2b). This is accounted for in the model by varying the proportion of coupling with neighbouring populations as described below.

In the case of no shear, we have (for non-boundary populations) the coupling term

$$\varepsilon \left(v_{i-1,j} + v_{i,j-1} - 4v_{i,j} + v_{i+1,j} + v_{i,j+1} \right)$$

representing material exchanging between population $v_{i,j}$ and each of four nearest neighbours. Since the inclusion of shearing causes rows to become misaligned, for $\kappa > 0$ there is now an additional interaction with populations $v_{i-1,j-1}$ and $v_{i+1,j+1}$ and the coupling term becomes a time varying function

$$\varepsilon \left[\left(A\left(t\right) v_{i-1,j-1} + \left(A\left(t\right) - 1 \right) v_{i-1,j} + v_{i,j-1} - 4v_{i,j} + v_{i,j+1} + \left(A\left(t\right) - 1 \right) v_{i+1,j} + A\left(t\right) v_{i+1,j+1} \right] \right.$$

for rows $i = 1, \ldots, n$ and columns $j = 1, \ldots, n$, with

$$A(t) = \rho \left[\left(\frac{t}{dt} \right) \bmod \left(\frac{1}{\rho} \right) \right]$$

so that

$$0 \leq A(t) < 1.$$

Every $\frac{1}{\rho}$ time-steps, that is at a time t such that $\frac{t}{dt} \bmod \left(\frac{1}{\rho} \right) = 0$, the rows are misaligned with respect to the original lattice by a whole grid-cell, e.g. grid-cell (i,j) is now "under" grid-cell (i-1,j-1) rather than grid-cell (i-1,j) (see Figure 4.2c). When this occurs a re-indexing step is applied to reflect the new position that each population occupies in the lattice, e.g. population (i,j) is re-labelled (i,j-1)

(see Figure 4.2c). Populations $v_{1,j}$, for columns $j = 1, \ldots, n$, are considered to be stationary and other rows are advected to the left proportionally according to the rate of shear. Any parcels of water leaving the lattice at the left hand edge re-enter at the right-hand edge and the populations are re-labelled according to their new position. The dynamics $\mathbf{v}_{i,j}(t)$ therefore represents an Eulerian time-series describing the biological evolution of the area of ocean bounded by the original lattice. Figure 4.2 shows this schematically.

The populations are taken to advect with the parcels of water, so that a re-indexing of the phytoplankton growth rate $a_{i,j}$ associated with each population $v_{i,j}$ is also applied, resulting in a time-dependent arrangement of growth rates and hence natural frequencies.

Additionally, a Lagrangian time-series is recorded describing the evolution of the biology in the parcel of water orginally labelled $v_{i,j}$ and now occupying a time-dependent position on the lattice. Accordingly, population frequencies, calculated as described in Chapter 3, are calculated using the Lagrangian time-series. This assumes that the spatial variability is related to local properties of the water. This may be true, for example, if the difference in phytoplankton growth rates relected small differences in species composition between populations advected with the water. In some cases, it might be more appropriate to consider the variability as fixed in space, for example if the variability were generated by varying bathymetry of a latitudinal temperate gradient.

Spatial dynamics are plotted using the Eulerian time-series.

4.2.2 Verification

To check for errors in the modified code, a number of tests were carried out.

Firstly, the advection scheme was checked by setting

$$\varepsilon = 0,$$

i.e. no mixing between grid-cells, and,

$$F_{i,j}(N_{i,j}, P_{i,j}, Z_{i,j}) = 0 \; \forall \; i, j,$$

i.e. no evolution of the biology (see Section 3.2). For ease of visualisation, the initial conditions are set to be uniform in the y-direction and linearly varying in the x-direction so that at time $t = 0$ a 2D plot of the lattice exhibits vertical stripes (see Figure 4.3). The system is integrated forward in time. As expected, the Lagrangian time-series for each population is unvarying:

$$\mathbf{v}_{i,j}(t) = \mathbf{v}_{i,j}(0) \; \forall \; t$$

so that lattice plots with the value in grid-cell (i,j) representing the phytoplankton biomass of the parcel of water originally occupying position (i,j) are seen to preserve the initial conditions (see Figure 4.3 columns 1 and 3). Lattice plots of the Eulerian phytoplankton biomass time-series are seen to shift by one grid-cell with respect to one another after each $\frac{1}{\rho}$ time-steps (see Figure 4.3 columns 2 and 4), indicating a correct implementation of the required shear.

Secondly, the frequency calculations, made by recording peaks in the Lagrangian phytoplankton biomass time-series, were checked by again setting $\varepsilon = 0$ but now allowing the biology to evolve. As expected, it was found that the standard deviation of frequencies $\sigma(t) = \sigma(t = 0) = \sigma(\epsilon = 0) \; \forall \; t$, i.e. the population frequencies, in the absence of any modifying interaction, remained at the natural frequencies for all time.

All other aspects of the code are unchanged and were checked prior to use in the simulations in Chapter 3 (see Section 3.2).

4.3 Results

For all simulations we set $n = 100$ to give a grid of 100×100 non-identical populations. Each population $v_{i,j}$ evolves according to (i) the internal dynamics represented by the NPZ system of Steele and Henderson (1981) with a 5% spread in the phytoplankton growth rates, (ii) interaction provided by effective diffusivity ε and (iii) advection of the water parcel as a result of shear of rate κ. Simulations are carried out for five different rates of shear, with the rate of shear remaining fixed throughout each simulation. For each value of shear, the effective diffusivity is varied in the range $\varepsilon \in [0, 0.05]$ d^{-1} as in Chapter 3. The system is integrated forward in time for

5000 days from synchronised initial conditions to allow transient behaviour to decay and for an additional 500 days to calculate the frequency and phase disorder and spatial statistics, as described in Section 3.2. As in Chapter 3, we present results for the phytoplankton components only (see Section 3.3.1).

4.3.1 No shear

For comparison, we first carried out a simulation with zero shear and varying effective diffusivity, i.e. $\kappa = 0$ d^{-1} and $\varepsilon \in [0, 0.05]$ d^{-1} with singly-periodic boundary conditions. Figure 4.4 shows final phytoplankton biomass for the lattice and Figure 4.5 shows the calculated frequency disorder σ as a function of effective diffusivity ε. As expected from the tests carried out in Section 3.3.3 on sensitivity to different boundary conditions, the results are as in Section 3.3 where the simulation differs only in having no-flux boundary conditions at all edges, but the results are nevertheless presented here for ease of comparision with the case of non-zero shear. To briefly recap, as ε is increased from 0 d^{-1}, for which the populations oscillate independently and asynchronously, the system level dynamics enter several distinct states. For $\varepsilon \in (0, 0.001]$, there is a small increase in the frequency disorder and small-scale local clustering; for $\varepsilon \in (0.001, 0.002]$, the system is nearly frequency-locked with large clusters; for $\varepsilon \in (0.002, 0.02]$ there us a large region of frequency disorder a magnitude larger than the natural frequency disorder and persistent small-scale clustering; for $\varepsilon > \varepsilon_{FL} = 0.02$, the system is frequency locked and approaches, although never fully achieves, phase locking as ε is increased.

4.3.2 Shear $\kappa > 0$

Simulations were carried out for five different rates of shear: $\kappa = 0.001$ d^{-1}, $\kappa = 0.005$ d^{-1}, $\kappa = 0.01$ d^{-1}, $\kappa = 0.05$ d^{-1} and $\kappa = 0.1$ d^{-1}, representing a change of three orders of magnitude from smallest to largest shear rate. These values cover a range typical of surface ocean shear (Sundermeyer and Price, 1998; Abraham et al., 2000). As described above, the emergent dynamics of the lattice are determined by the influences of the biological dynamics, the effective diffusivity and the advection caused by shear, each of which has an associated time-scale: T_{NPZ}, T_ε and T_κ,

respectively. $T_{NPZ} \approx 100$ days is the period of oscillation of the biological dynamics. $T_\varepsilon = \frac{1}{\varepsilon}$ ranges from infinitely slow up to 20 days since $\varepsilon \in [0, 0.05]$ d^{-1}. Since this chapter is concerned with an investigation of the relative influence of advection, values of κ have been chosen to give advection time-scales values T_κ slower than, equal to and faster than T_{NPZ} and T_ε.

The phytoplankton biomass fields in gC m^{-3} at time $t = 5000$ days are shown in Figures 4.6 to 4.10 for $\kappa = 0.001$ d^{-1}, $\kappa = 0.005$ d^{-1}, $\kappa = 0.01$ d^{-1}, $\kappa = 0.05$ d^{-1} and $\kappa = 0.1$ d^{-1}, respectively, for $\varepsilon \in (0, 0.05]$. The biomass plots for $\varepsilon = 0$ are omitted because in the absence of effective diffusivity the plankton populations do not interact and therefore do not alter their natural oscillations and are merely advected as a result of the shearing, resulting in the same grainy-structure of independently oscillating populations for any rate of shear.

Figures 4.6 to 4.10 indicate that under the influence of shear the system can retain the coherent structure (local synchrony, or clustering) caused by the effective diffusivity for all rates of shear considered. As in the no-shear case, small-scale clustering persists for increasing ε until a critical value ε_{FL} at which the whole ensemble frequency-locks and the spatial pattern is domain-sized.

This is seen more clearly in Figure 4.11, which shows the frequency disorder σ and phase coherency parameter R as a function of effective diffusivity for the five different rates of shear. The general pattern is as described fully in Section 3.3.2, with a region of frequency disorder indicated by high values of σ that increase from $\sigma(\varepsilon = 0) \approx 2.5\%$ to as much as 20%, followed by an abrupt shift to frequency locking signalled by $\sigma \approx 0\%$, although the small region of near frequency-locking observed in the case of zero shear for small ε no longer occurs. For shear rates of κ =0.001, 0.005, 0.01, 0.05 and 0.1 d^{-1}, $\varepsilon_{FL} = 0.035$, 0.041, 0.044, 0.027 and 0.019 d^{-1}, respectively. However, unlike in the zero shear case, for $0 < \kappa < 0.1$ d^{-1} the system "jumps" in and out of frequency-locking for values of effective diffusivity lower than the final critical ε_{FL}, in a similar fashion as seen in Figure 3.4 for the case of zero-shear with a fixed domain length and varying spatial resolutions. This is seen in Figure 4.11 as a series of changes in system state from $\sigma \approx 0\%$ to $\sigma \approx 20\%$ and in the biomass plots in Figures 4.6 to 4.10 as a succession of transitions from small-scale clustering

to domain-scale synchronisation and back again as ε is increased. For example, for $\kappa = 0.001$ d^{-1}, biomass plots for $\varepsilon = 0.03$ d^{-1} and $\varepsilon = 0.034$ d^{-1} show clustering but for $\varepsilon = 0.032$ d^{-1} the system is frequency-locked (Figure 4.6).

In all cases, for $\varepsilon > \varepsilon_{FL}$ the order parameter R tends rapidly to 1 (see Figure 4.11) and the corresponding biomass plots become increasingly homogeneous as the ensemble phase locks. Although the populations are phase-locked, the variation in colour seen in, for example, the phytoplankton biomass field for $\varepsilon = 0.05$ d^{-1} for $\kappa = 0.05$ d^{-1} (Figure 4.9), indicates that the amplitudes of oscillation across the domain remain unsynchronised. The result is that the plots vary in uniformity depending upon the phase of oscillation at the time $t = 5000$ days when we record the values of phytoplankton biomass; when recorded during the trough the plots appear monochrome and when during a peak the difference in amplitude is manifested as increased variation. This is why the biomass plot for $\varepsilon = 0.05$ d^{-1} for $\kappa = 0.05$ d^{-1} in Figure 4.9 shows bands of high and medium high phytoplankton biomass whereas the plots for lower values of effective diffusivity are uniform in colour. This phenomenon has been seen in nature, e.g. the hare-lynx dynamics studied by Moran (1953), and in modelling studies of population dynamics, e.g. Blasius and Stone (2000).

Figures 4.6 to 4.10 show clearly that, in comparison with the zero shear case, the inclusion of shear alters the spatial characteristics of the clustering seen in the ranges $0 < \varepsilon < \varepsilon_{FL}$. The advection does not, as might be expected, break up regions of local synchrony; there is still clear evidence of persistent coherent structure. Even for the largest shear (Figure 4.10; $\kappa = 0.1$ d^{-1}), the clusters are not simply stripes of uniform phytoplankton biomass aligned with the x-direction. This indicates that the *spatial positioning* of the clusters is non-stationary (as observed also in Section 3.3.1), since otherwise the effect of shear would be to narrow and stretch the clusters until they reached a steady-state as a horizontal stripe.

In fact, for the lowest values of shear, $\kappa = 0.001$ d^{-1} and $\kappa = 0.005$ d^{-1}, the clustering observed in Figures 4.6 and 4.7 is indistinguishable by eye from the kind of structure seen in the zero shear case in Figure 4.4. The shear rate is too slow to impose directionality upon the clustering generated by the effectively diffusive coupling. For higher values of shear, $\kappa = 0.01$ d^{-1}, $\kappa = 0.05$ d^{-1} and $\kappa = 0.1$ d^{-1}

(Figures 4.8 to 4.10), there is a definite directionality to the spatial structure. With respect to the no-shear simulation, the clusters are narrowed and stretched by the shearing and are increasingly aligned with the x-axis, but are still non-stationary.

The change in structure that can be seen by eye is well supported by the cluster measures $c_x(\varepsilon)$ and $c_y(\varepsilon)$ (as defined in Section 3.2.3) shown in Figure 4.12, with σ given as a dotted line for reference. The gradient measure $g(\varepsilon)$ is shown in Figure 4.13, again with σ for reference. As explained in Section 3.2, the cluster measure only has clear meaning for a high value of the gradient measure g, indictating well-defined clusters separated by sharp gradients in plankton biomass values. For all values of shear considered here, Figure 4.13 shows that $g > 0.7$ for $\varepsilon < \varepsilon_{FL}$ and drops sharply to $g < 0.4$ at the transition to frequency-locking.[1] Hence we only discuss the behaviour of the cluster measures in the desynchronised region defined by $\varepsilon < \varepsilon_{FL}$, i.e. where small-scale clustering dominates. The succession of transitions in behaviour observed close to ε_{FL} will be discussed in Section 4.3.3.

For $\kappa = 0.001$ d^{-1} and $\kappa = 0.005$ d^{-1}, $c_x(\varepsilon) \approx c_y(\varepsilon)$ for all $\varepsilon < \varepsilon_{FL}$, confirming that the clusters are not skewed in a particular direction. There is a steady increase in c_x and c_y from 1 to 8 grid-cells with increasing ε, interrupted by the aforementioned "jumps" to the frequency-locked state.

For $\kappa = 0.01$ d^{-1}, $c_x(\varepsilon) > c_y(\varepsilon)\ \forall\ \varepsilon < \varepsilon_{FL}$, with c_x increasing from 1 to 10 grid-cells and c_y increasing from 1 to 8 grid-cells with increasing ε. The difference $|c_x - c_y|$ between the cluster size in each direction increases with increasing ε. The same trend is seen more markedly for increasing shear. For $\kappa = 0.05$ d^{-1}, c_x increases from 1 to 14 grid-cells, whilst c_y increases from 1 to only 5 grid-cells, and for $\kappa = 0.1$ d^{-1}, c_x increases from 1 to 15 grid-cells, whilst c_y increases from 1 to only 4 grid-cells with increasing ε. These numbers show a trend of increasing stretching of clusters in the x-direction and narrowing in the y-direction, as expected from the shearing applied to the ensemble.

From the results seen here, it is impossible to say conclusively whether the addition of shearing aids or hinders synchronisation of the ensemble as there is no clear

[1] There is some deviation from this pattern for $\kappa = 0.1$ d^{-1}, for which Figure 4.13 shows values of $g \approx 0.8$ for $\varepsilon = 0.024 > \varepsilon_{FL}$. Since the corresponding plankton biomass plot in Figure 4.10 shows almost fully homogeneous dynamics, it is not clear why the gradient measure is so high.

pattern in the value of ε_{FL} with increasing κ. We can, however, say conclusively that the inclusion of realistic levels of shear alters the spatial characteristics of the ensemble whilst allowing coherent clusters to persist.

4.3.3 Variability

The rapid transitions between the states of frequency disorder and frequency-locking as ε approaches ε_{FL} from below, as seen in Figure 4.11 and in the biomass plots in Figures 4.7 to 4.10 and described above, can be understood in the context of the findings of Chapter 3. In Section 3.3, we found that for a fixed number of populations with a particular set and spatial arrangement of phytoplankton growth rates $\{a_{i,j}\}$ and resultant natural frequencies $\{\omega_{i,j}\}$ there exists a single point of transition to frequency locking at a value of effective diffusivity ε_{FL} (see Figure 3.6). In Section 3.5, it was found that ε_{FL} varies widely depending on the particular set and arrangement of natural frequencies, even when the growth rate parameter values are selected from the same uniform distribution (see Figure 3.26).

In the experiment carried out here, we have a fixed set $\{a_{i,j}\}$ of growth rates. However, the imposed shear causes advection of the plankton populations and accompanying growth rates, leading to a rearrangement of the growth rates on the lattice, i.e. the particular spatial arrangement of the natural frequencies varies with time. For each of the n spatial arrangements possible for a lattice of $n \times n$ populations, we know from Chapter 3 that there exists a particular, most likely different, ε_{FL} in the case of no shear. It is the variation in this ε_{FL} with time, caused by the variation in spatial arrangement of natural frequencies, that causes the irregular transitions approaching ε_{FL} observed in Figure 4.11.

We illustrate this by carrying out some simple experiments. These are set up exactly as above but, for speed of performing ensemble runs, we set $n = 10$ to give a lattice of 10×10 populations. For a fixed set of phytoplankton growth rate parameters $\{a_{i,j}\}$, for shear rates of $\kappa = 0$ d^{-1}, $\kappa = 0.001$ d^{-1} and $\kappa = 0.1$ d^{-1}, calculations of the frequency spread σ as a function of effective diffusivity ε were made for each of the ten possible advection-induced initial spatial arrangements of natural frequencies.

Figure 4.14 shows the calculations of σ as a function of ε for each of the ten spatial configurations of the set $\{a_{i,j}\}$ for zero shear, so that in this case the imposed arrangement of natural frequencies is constant in time. The resultant ε_{FL} is seen to range from $\min(\varepsilon_{FL}) = 0.002$ d^{-1} to $\max(\varepsilon_{FL}) = 0.016$ d^{-1}, each spatial arrangement leading to a specific ε_{FL}.

Figures 4.15 and 4.16 shows the same calculations for $\kappa = 0.001$ d^{-1} and $\kappa = 0.1$ d^{-1}, respectively. For non-zero shear, the initially-imposed spatial arrangement of natural frequencies varies with time, at a rate dependent upon the value of κ.

For ease of comparison, Figure 4.17 shows the calculations of σ as a function of ε for each different spatial arrangement on the same plot for $\kappa = 0$ d^{-1} (*top*), $\kappa = 0.001$ d^{-1} (*middle*) and $\kappa = 0.1$ d^{-1} (*bottom*).

With a shear of rate $\kappa = 0.001$ d^{-1}, for each initial configuration of populations, there is a range of ε (roughly coincident with the range $\varepsilon_{FL} \in [0.002, 0.016]$ d^{-1} found above for $\kappa = 0$ d^{-1}), for which the ensemble dynamics move in and out of frequency locking with increasing ε before eventually permanently frequency locking. This is the same behaviour as described in Section 4.3.2 for $n = 100$; the rearrangement of populations, and corresponding natural frequencies, with time alters the value of effective diffusivity ε at which frequency-locking would occur in the absence of advection and causes a succession of transitions within this range.

However, this effect is dependent on the *rate* of shear. In this case, the time scale of advection $T_\kappa = \frac{1}{\kappa} = 1000$ days, which, within the range of effective diffusivities $\varepsilon \in [0.002, 0.016]$, gives $T_\kappa > T_\varepsilon$ and $T_\kappa > T_{NPZ}$. Hence, the dominant effect on the ensemble dynamics is the effective diffusivity, with the system being pulled towards frequency locking at a value of ε varying with the time-dependent configuration of populations.

For $\kappa = 0.1$ d^{-1}, we have $T_\kappa = 10$ days, so that $T_\kappa < T_\varepsilon$ for the full range of effective diffusivity and $T_\kappa < T_{NPZ}$. In this case, Figures 4.16 and 4.17 indicate that the ensemble is frequency locked for $\varepsilon > 0.002$ d^{-1} for all initial spatial configurations of the populations; the faster shear actually alters the ability of the ensemble to synchronise, possibly by increasing the network of influence of each population. In other words, advection at this rate allows each population to be coupled with a

greater number of populations on the relevant time-scale and therefore effectively alters the coupling geometry of the system and enhances the mixing. Hence, advection increases the ability of the lattice of populations to synchronise their dynamics.

Significantly, these results also show that advection of populations has the potential to reduce the simulation-to-simulation variability, described in Section 3.5, caused by variability in the particular values and spatial arrangements of natural frequencies for different random selections of the parameter mismatch values.

4.4 Discussion

In this chapter we have investigated the impact of advection, at scales larger than the model grid-cell, on the system of locally-coupled non-identical plankton populations studied in Chapter 3. The evolution of the populations is determined by the internal biological dynamics, the interaction caused by the nearest-neighbour coupling and advection caused by the shear.

It has been found that many of the features seen for the mixing-only system, as described in Chapter 3, are retained under the influence of shear. The properties of synchrony exhibited by the system as the effective diffusivity is increased from 0 to 0.05 d^{-1} are broadly similar, with the nonintuitive increase in the spread in population frequencies as the coupling strength is increased from zero, leading to a region of small-scale clustering and frequency disorder, followed by a shift to frequency-locking at a value of effective diffusivity ε_{FL}.

Unlike in the case of zero-shear, however, there is not one single value of ε at which the transition to frequency-locking occurs; rather, the system "jumps" rapidly between the two states before eventually frequency-locking permanently at $\varepsilon = \varepsilon_{FL}$. This "jumping" results from the rearrangement of the populations caused by the shear; since the populations are assumed to advect with the parcels of water, the spatial arrangement of natural frequencies varies with time. ε_{FL} has been shown to vary with the arrangement of natural frequencies, resulting here in a number of transitions in and out of frequency-locking before permanent frequency-locking at $\varepsilon = \varepsilon_{FL}$.

We have also seen that this "jumping" does not occur for the fastest shear considered here, $\kappa = 0.1$ d^{-1}, for which only one transition to frequency-locking occurs, as in the mixing-only case. We have shown that this is caused by the rapid rearrangement of the populations, allowing previously separated populations to interact on time-scales faster than those of either the biology (of period 120 days) or the effective diffusivity (time-scale > 50 days). The net effect of this fast shear is to alter the coupling geometry, increasing the range of influence of each population and "ironing out" the variability in ε_{FL} usually caused by altering the spatial arrangement of the natural frequencies. This effect is not seen for slower rates of shear as the time-scale of interaction of separated populations is slower than the effective diffusivity.

Here, advection of the populations is caused by a simple shear in one direction. The resulting time-varying coupling geometry allows each population to interact with the oscillators occupying rows above and below the population on a time-scale governed by the rate of shear. A more realistic representation of the stirring of the upper ocean flow would allow each population to come into contact not only with populations in rows above and below, but potentially with *all* other populations in the region, again on a time-scale governed by the rate of stirring. In the limit of fast stirring with respect to the mixing time-scale, the system could act as though globally coupled, as found by Neufeld et al. (2003). Clearly, the particular spatial arrangement of the natural frequencies would then become irrelevant, removing the variability in the behaviour of the system caused by the underlying frequency disorder seen in Section 3.5. The mitigation of this problematic aspect of the zero-shear system by the inclusion of shear is encouraging for biophysical modelling of the upper ocean. However, the abrupt transition from small-scale clustering to domain-scale synchronisation still occurs when shear is included.

For $\varepsilon > \varepsilon_{FL}$, the ensemble approaches phase-locking far more rapidly than was seen in the zero-shear case. Additionally, the maximum value of frequency spread σ attained in the frequency disorder regime for each value of the shear is smaller than that attained in the no-shear case. These two facts suggest that the shear does increase the ability of the system to synchronise but no clear relationship between

ε_{FL} and the rate of shear κ has been found because of the "jumping" phenomena discussed above.

Although the system still exhibits well-defined clustering within the region of frequency disorder defined by $\varepsilon < \varepsilon_{FL}$, the shear has the potential to alter the spatial characteristics of this clustering. For a rate of shear κ slow with respect to the timescale of effective diffusivity ε, the structure remains isotropic; sub-grid-cell level mixing is the dominant process. For κ fast with respect to ε, the shearing draws the clusters out in the direction of flow, causing stretching in the x-direction and narrowing in the y-direction, as indicated by the cluster measure results in Figure 4.12. The resulting clusters are elongated and increasingly aligned with the horizontal as the rate of shear is increased.

We conclude that shear appears to aid synchronisation by extending the network of influence of each population in the lattice, but that the strength of this effect depends crucially upon the *rate* of shear, with respect to the other processes affecting the evolution of each population.

It would be interesting to explore the impact of a more realistic representation of upper ocean physical flow. Given the range of complex phenomena possible in fully turbulent models, this is beyond the scope of this project. Nevertheless, it is in keeping with the philosophy of the whole investigation, which has attempted to build "step-by-step" from an idealistic to a more realistic biophysical representation, to begin with this simple representation of advection caused by shear; the work described here covers all the basic components of more realistic flows and therefore provides a good foundation upon which to build.

Figure 4.1: Schematic showing velocity $u(y)$. Length of arrows indicates the rate of flow relative to neighbouring rows.

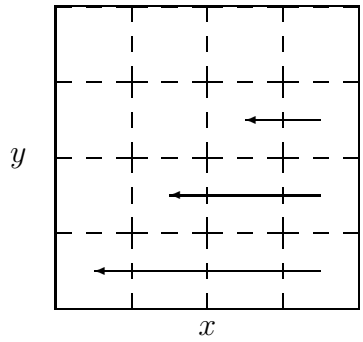

Figure 4.2: Schematic of model implementation of advection caused by shear of rate $\kappa > 0$, causing shifting of each row i with respect to row $i+1$ by a fraction $\rho \in (0,1)$ at each time-step.

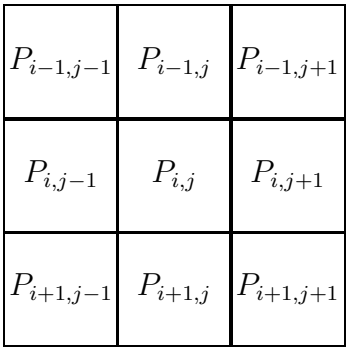

(a) Labelling of populations at a time t such that $\frac{t}{dt} \mathrm{mod} \frac{1}{\rho} = 0$.

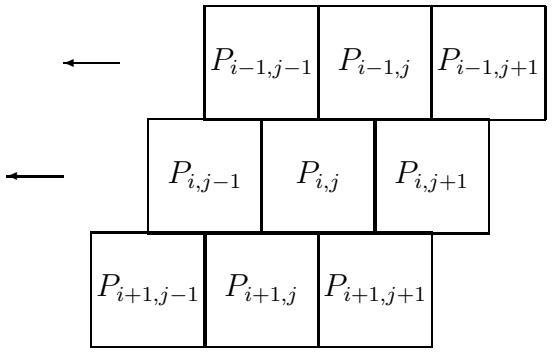

(b) Positions of populations at a time t such that $0 < \frac{t}{dt} \mathrm{mod} \frac{1}{\rho} < 1$.

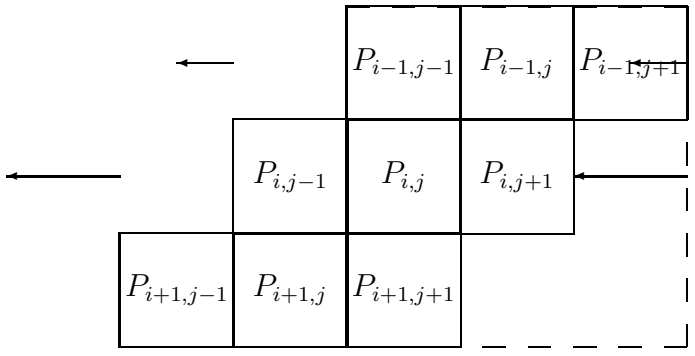

(c) Positions of populations before re-labelling at a time t such that $\frac{t}{dt} \mathrm{mod} \frac{1}{\rho} = 1$. Parcels of water leaving the region at the left hand side re-enter at the right and are re-labelled accordingly.

Figure 4.3: **Testing the model**. Eulerian (*columns 1 and 3*) and Lagrangian (*columns 2 and 4*) time-series for $n = 100$ for no mixing ($\varepsilon = 0$) and no evolution of biology ($F(N_{i,j}, P_{i,j}, Z_{i,j}) = 0\ \forall i, j$ for $i, j = 1, \ldots, 100$) for shear rate $\kappa = 0.1$ d^{-1}. Titles indicate time in days. Initial conditions of $N_{i,j}$, $P_{i,j}$ and $Z_{i,j}$ are constant in the y-direction and linearly varying in the x-direction, for ease of visualisation.

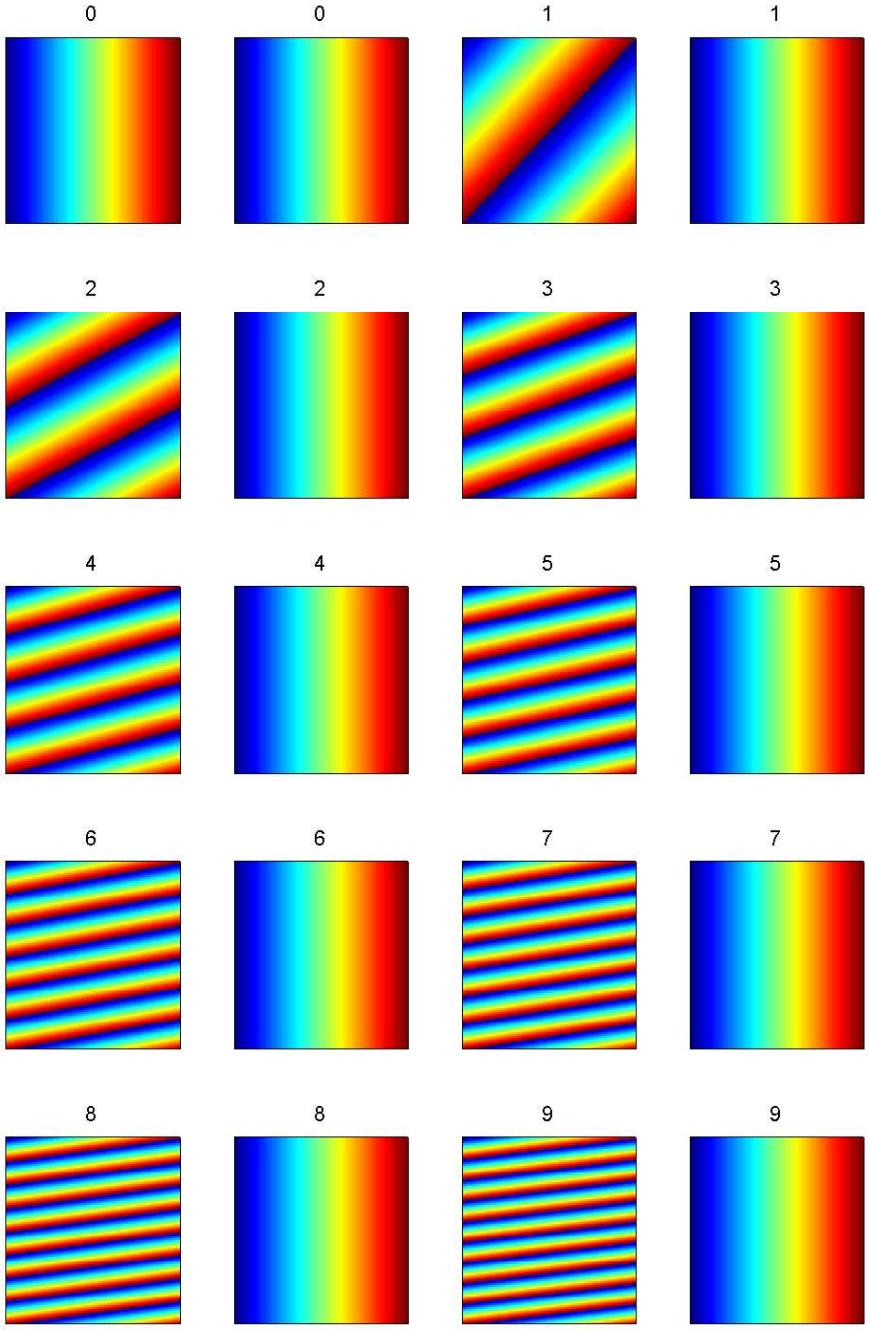

Figure 4.4: **No shear.** Phytoplankton biomass for $n = 100$ at time $t = 5000$ days after integration from homogeneous initial conditions. Boundary conditions are periodic at the left and right edges; no-flux at the top and bottom. Shear rate $\kappa = 0$ d^{-1}. Figure titles indicate value of ε in d^{-1}.

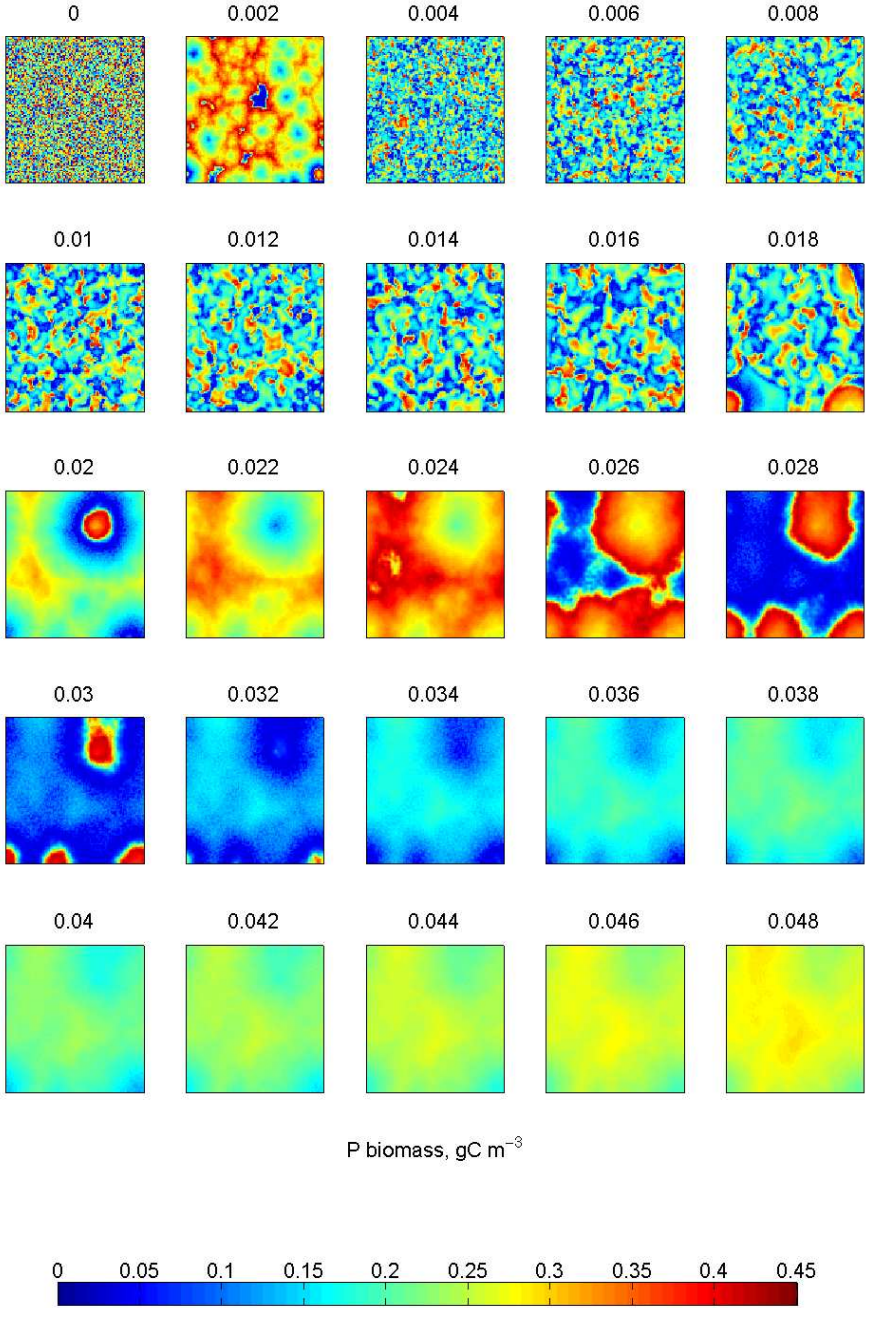

Figure 4.5: **No shear.** Frequency disorder σ as a function of effective diffusivity ε for $n = 100$ at time $t = 5000$ after integration from homogeneous initial conditions. Boundary conditions are periodic at the left and right edges; no-flux at the top and bottom. Shear rate $\kappa = 0$ d^{-1}.

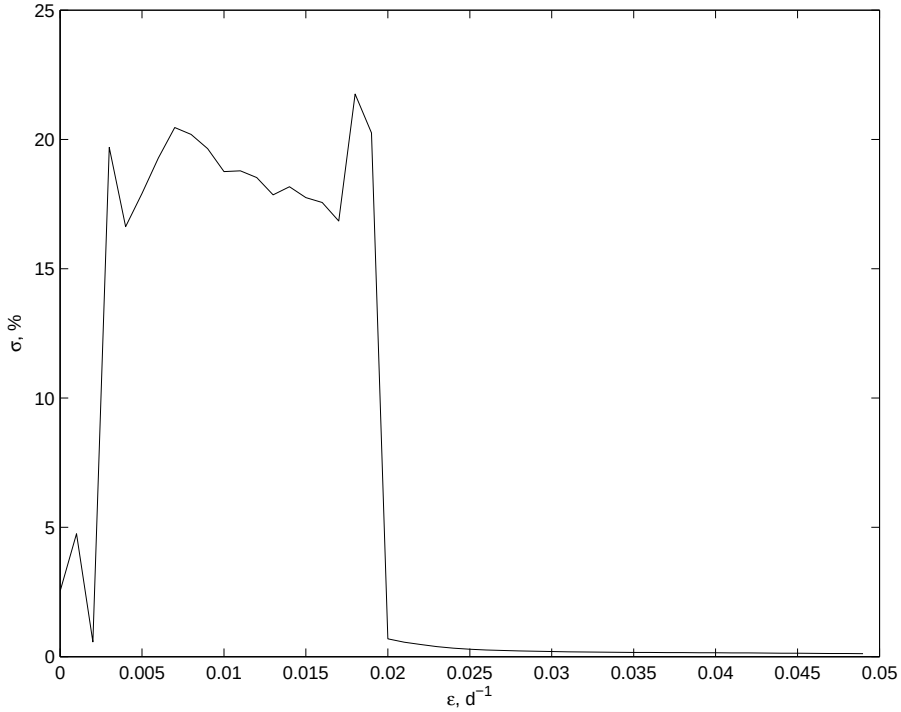

Figure 4.6: **Shear 0.001 $\mathbf{d^{-1}}$.** Phytoplankton biomass for $n = 100$ at time $t = 5000$ days after integration from homogeneous initial conditions. Boundary conditions are periodic at the left and right edges; no-flux at the top and bottom. Shear rate $\kappa = 0.001$ d^{-1}. Figure titles indicate value of ε in d^{-1}.

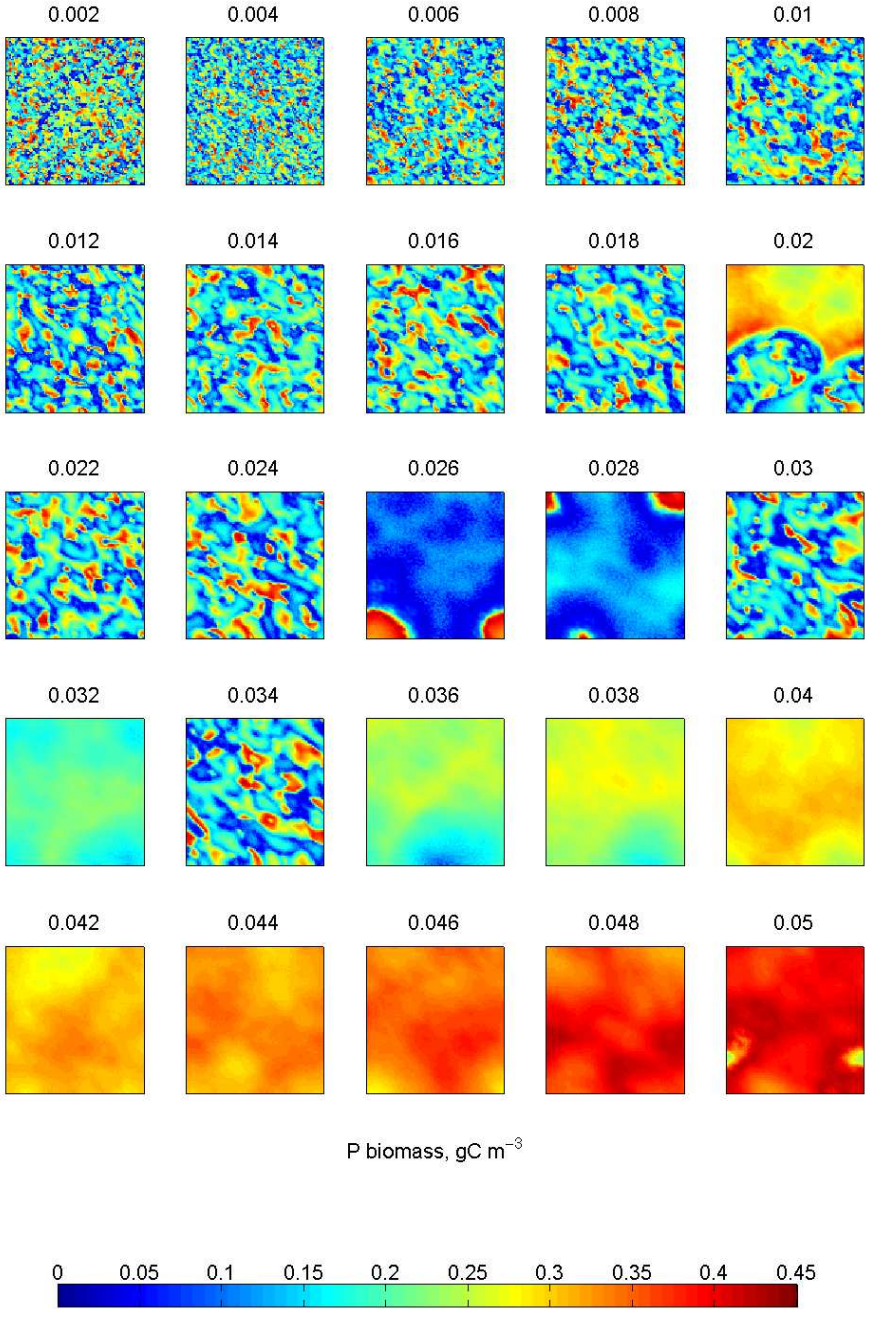

Figure 4.7: **Shear 0.005 $\mathbf{d^{-1}}$.** Phytoplankton biomass for $n = 100$ at time $t = 5000$ after integration from homogeneous initial conditions. Boundary conditions are periodic at the left and right edges; no-flux at the top and bottom. Shear rate $\kappa = 0.005$ d^{-1}. Figure titles indicate value of ε in d^{-1}.

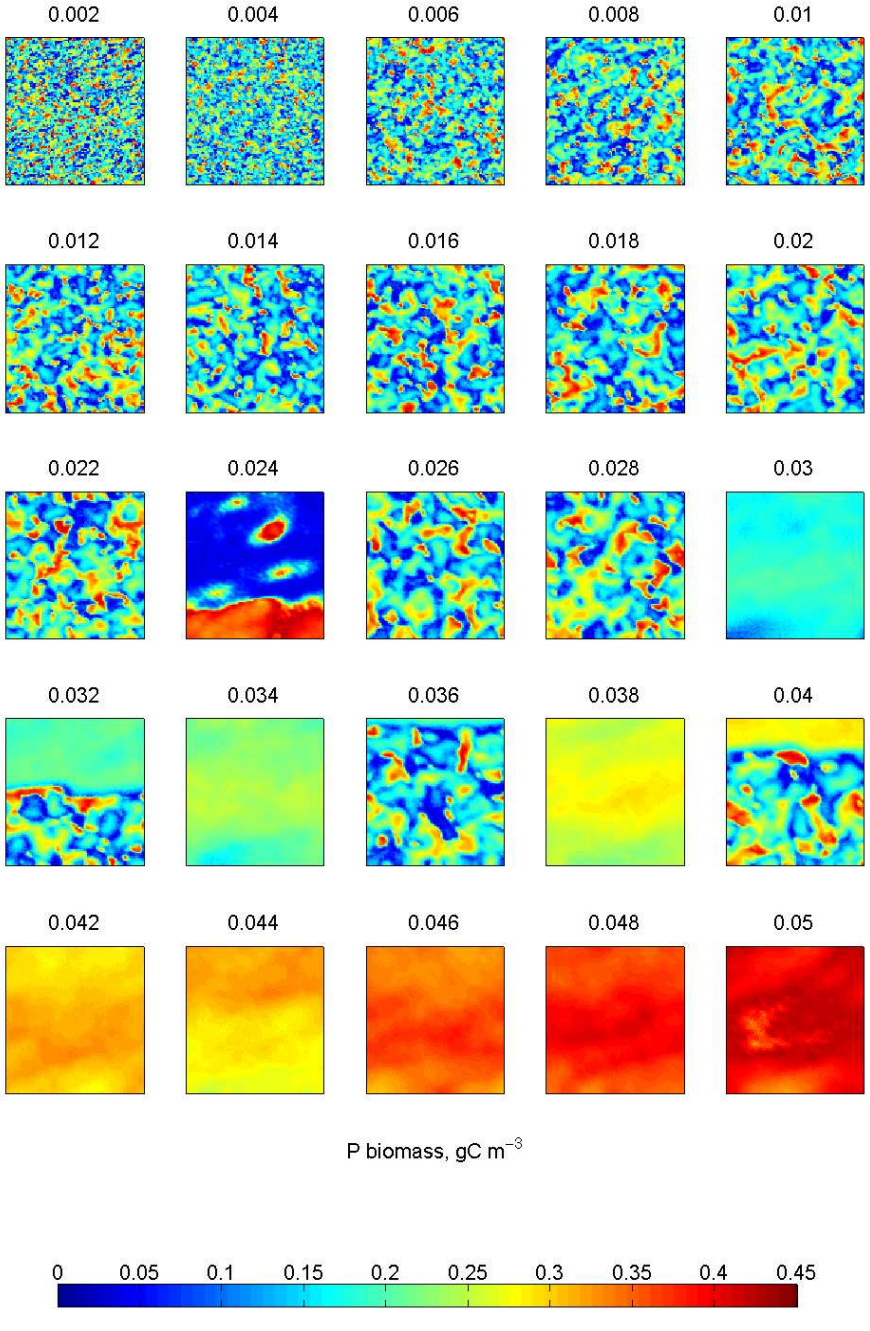

Figure 4.8: **Shear 0.01 $\mathbf{d^{-1}}$.** Phytoplankton biomass for $n = 100$ at time $t = 5000$ after integration from homogeneous initial conditions. Boundary conditions are periodic at the left and right edges; no-flux at the top and bottom. Shear rate $\kappa = 0.01$ d^{-1}. Figure titles indicate value of ε in d^{-1}.

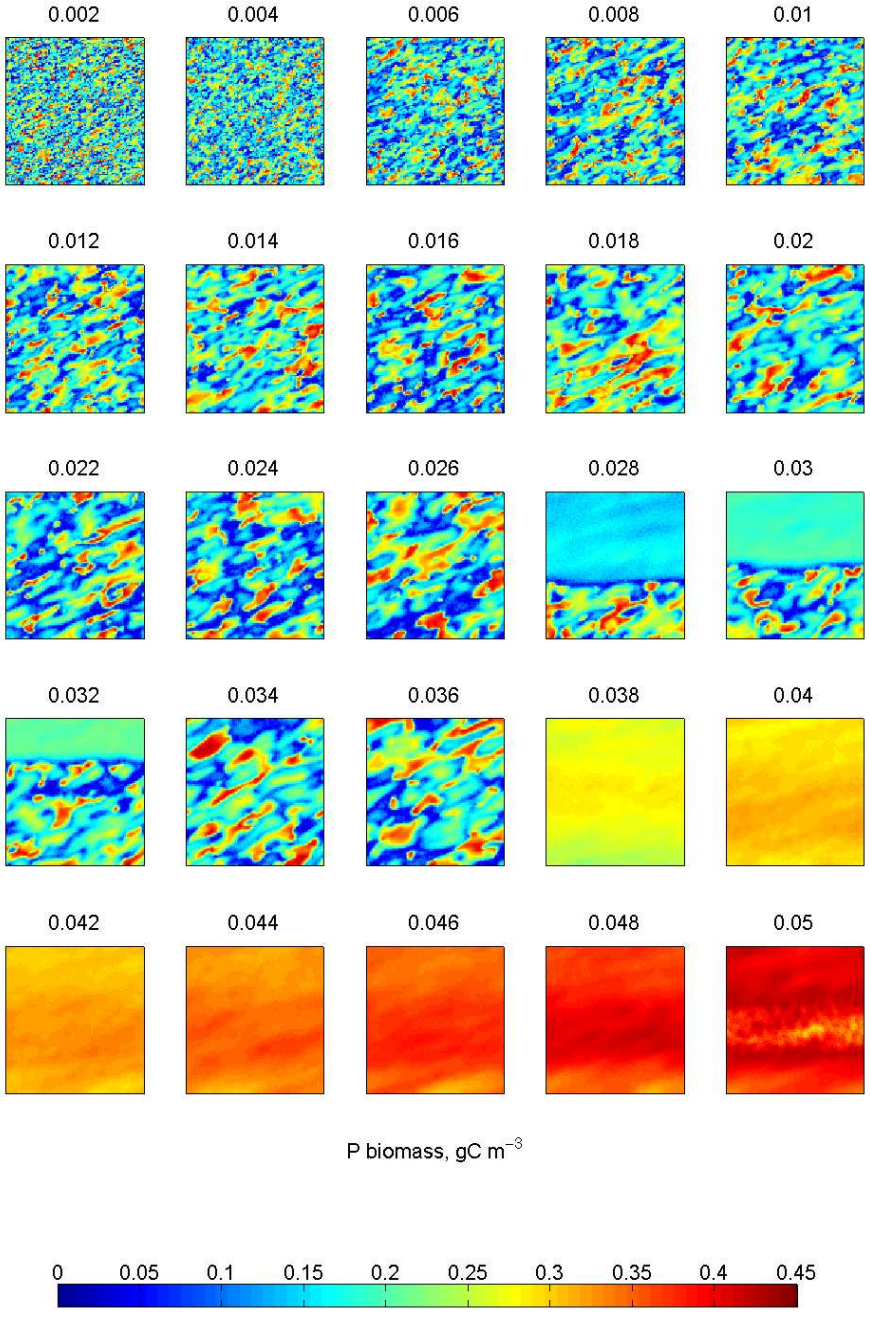

Figure 4.9: **Shear 0.05 $\mathbf{d^{-1}}$.** Phytoplankton biomass for $n = 100$ at time $t = 5000$ after integration from homogeneous initial conditions. Boundary conditions are periodic at the left and right edges; no-flux at the top and bottom. Shear rate $\kappa = 0.05$ d^{-1}. Figure titles indicate value of ε in d^{-1}.

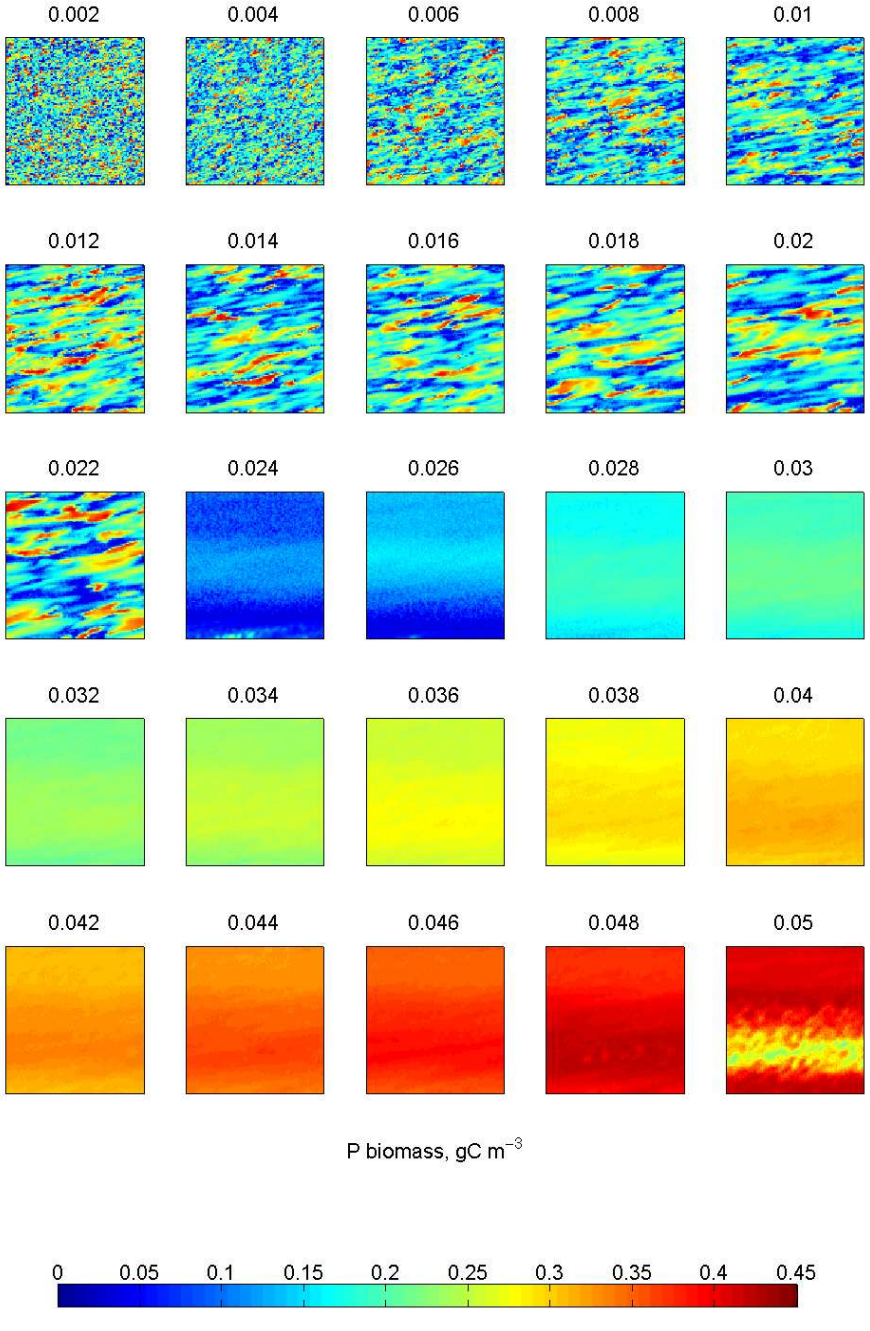

Figure 4.10: **Shear 0.1 $\mathbf{d^{-1}}$.** Phytoplankton biomass for $n = 100$ at time $t = 5000$ after integration from homogeneous initial conditions. Boundary conditions are periodic at the left and right edges; no-flux at the top and bottom. Shear rate $\kappa = 0.1$ d^{-1}. Figure titles indicate value of ε in d^{-1}.

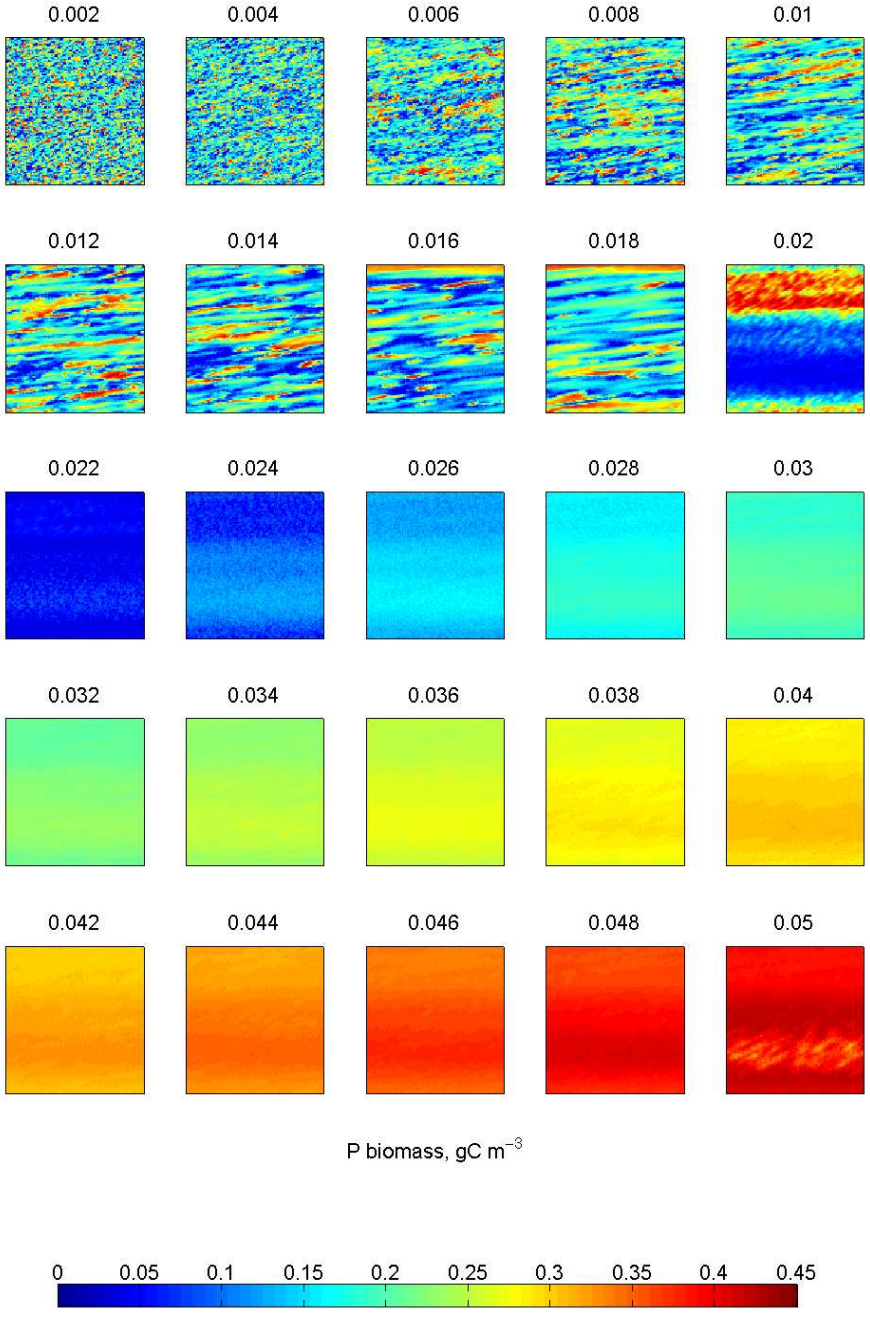

Figure 4.11: **Frequency and phase disorder.** Frequency disorder σ (*solid*) and order parameter R (*dashed*) as a function of effective diffusivity ε in d^{-1} for different rates of shear κ for $n = 100$.

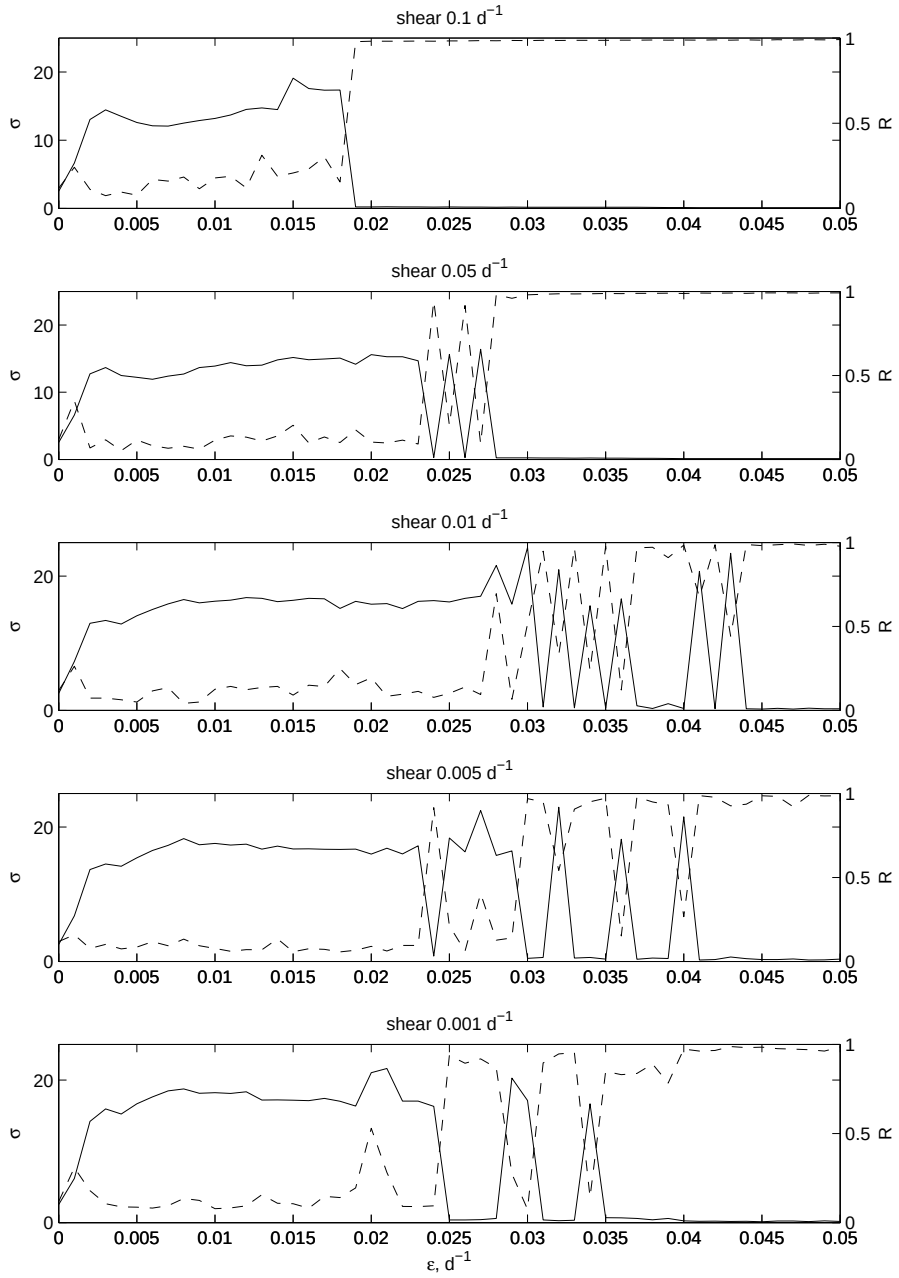

Figure 4.12: **Spatial diagnostics.** Clustering measures c_x (*black*) and c_y (*red*) in numbers of grid-cells as a function of effective diffusivity ε for different rates of shear κ. $n = 100$. $\sigma(\varepsilon)$ shown by dotted line for reference.

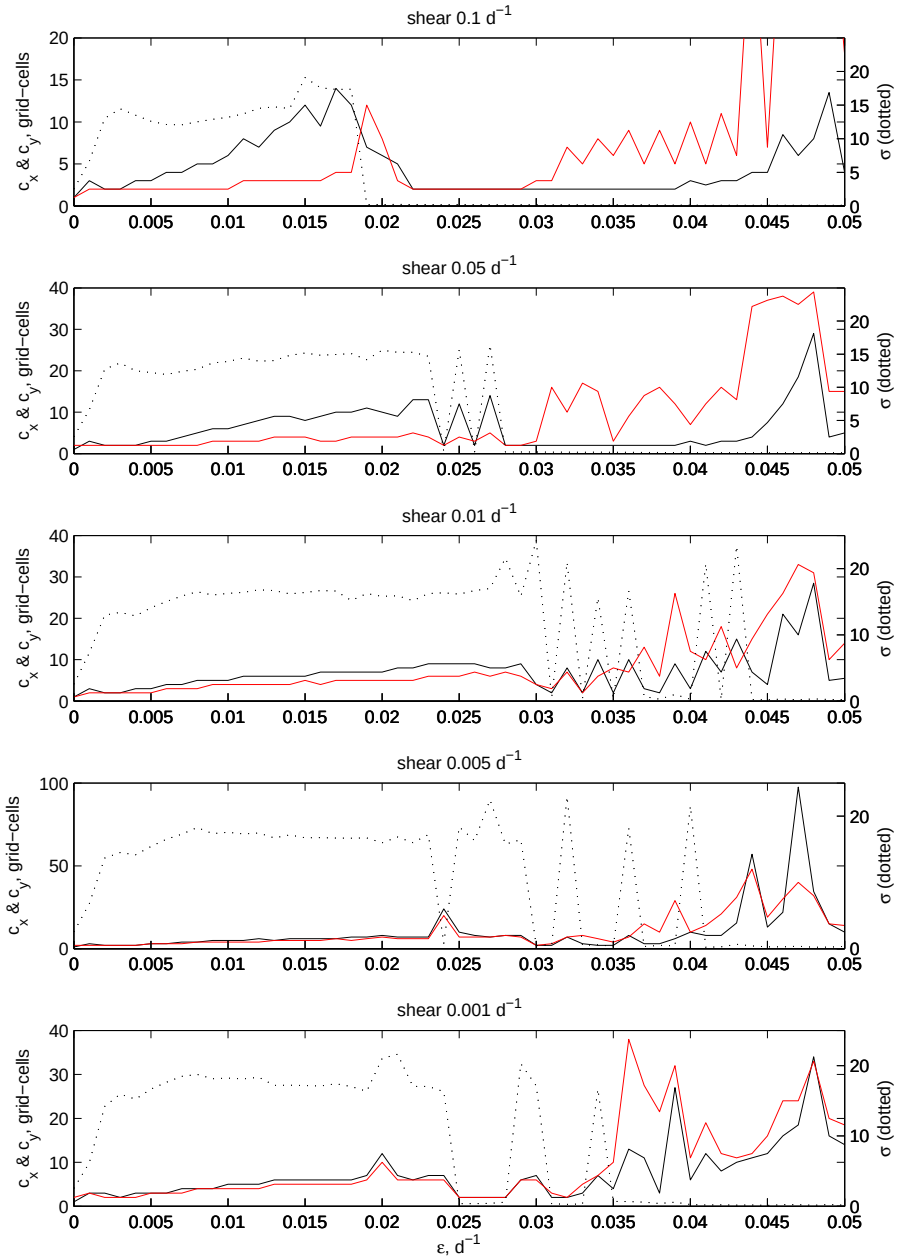

Figure 4.13: **Spatial diagnostics.** Gradient measure g as a function of effective diffusivity ε in d^{-1} for different rates of shear κ. $n = 100$. $\sigma(\varepsilon)$ shown by dotted line for reference.

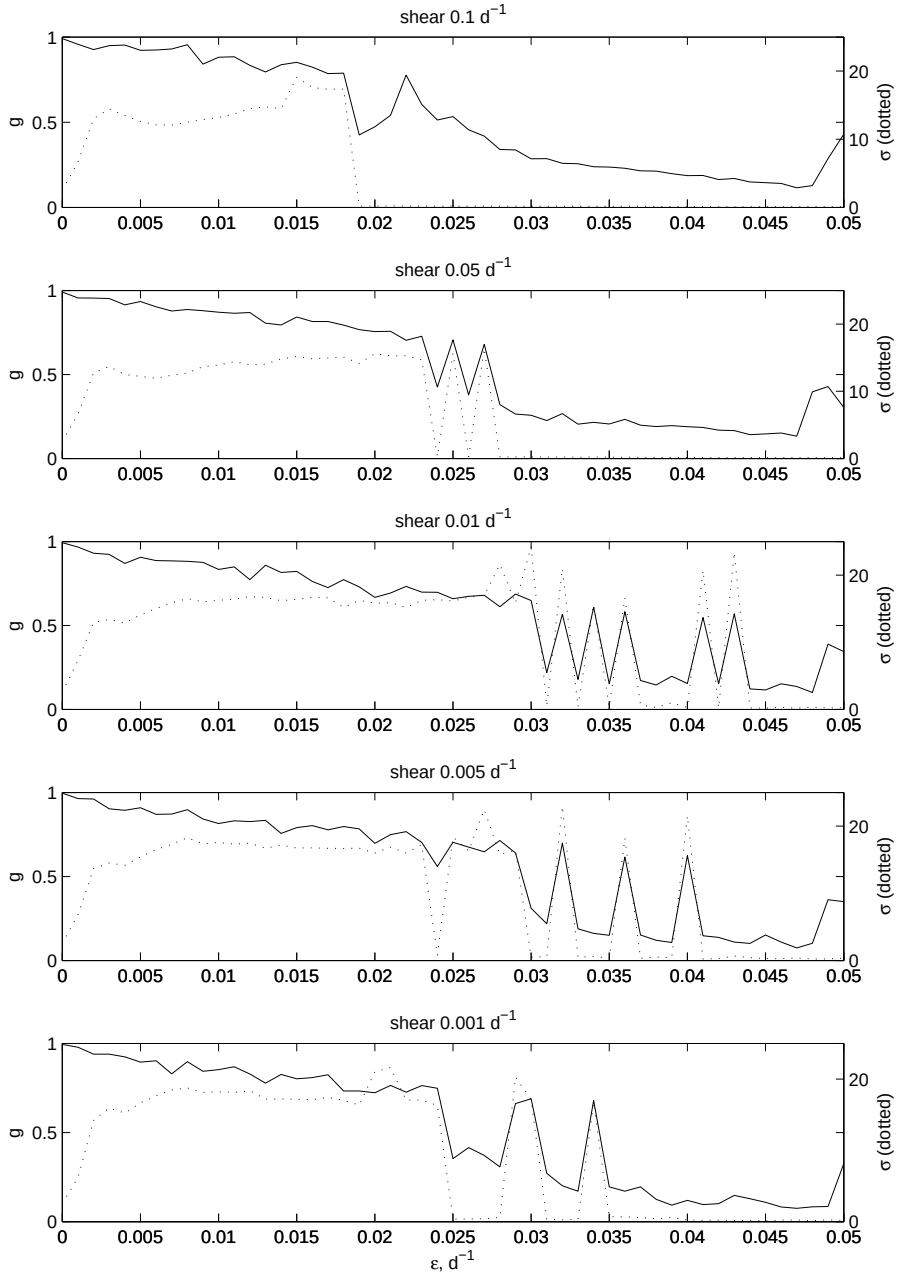

Figure 4.14: **Zero shear: $\kappa = 0$ $\mathbf{d}^{-1}$.** Frequency spread σ as a function of effective diffusivity ε in d^{-1} for a lattice of 10×10 plankton populations in each of the 10 possible initial spatial arrangements (under advection) of phytoplankton growth rates $\{a_{i,j}\}$.

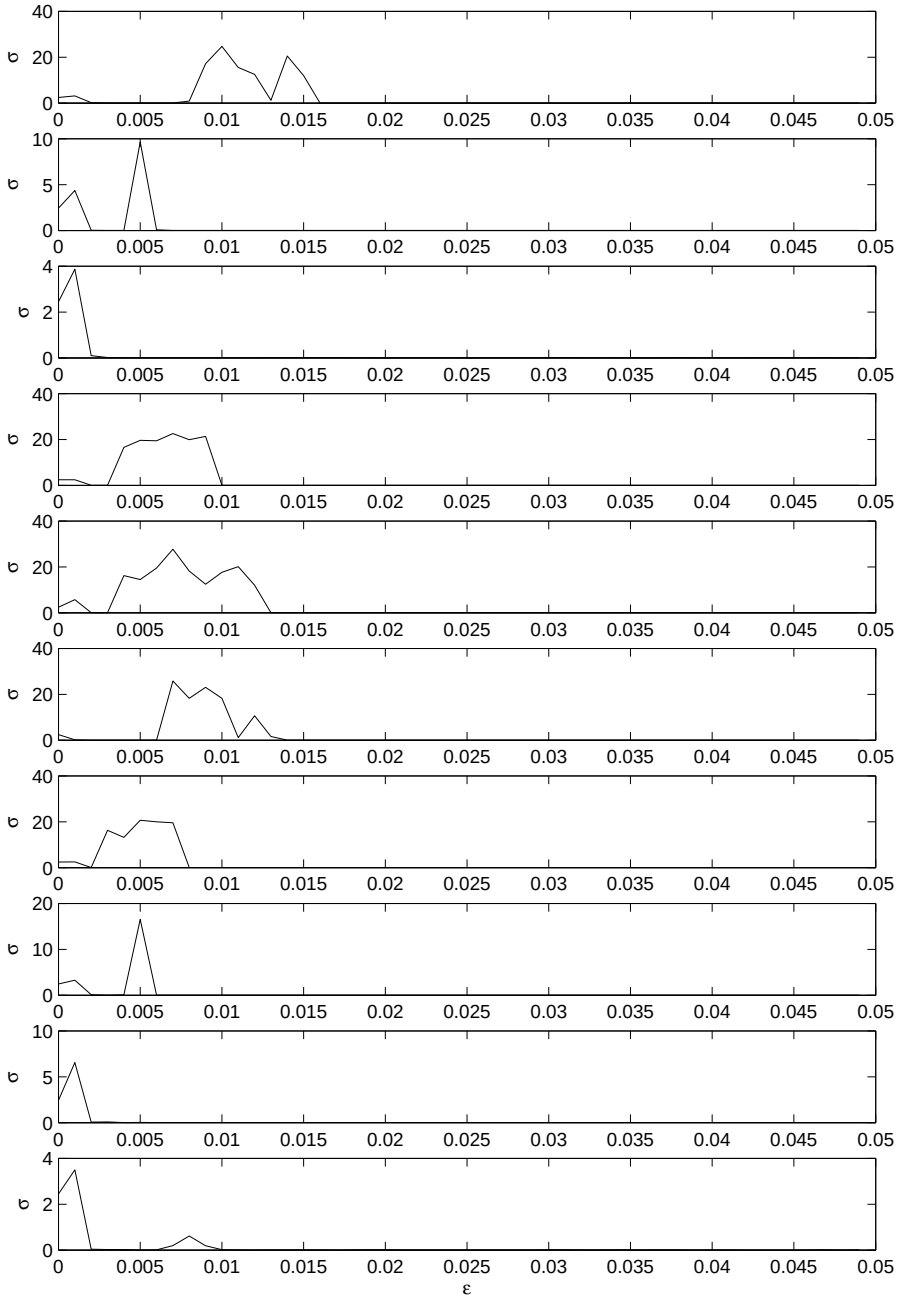

Figure 4.15: **Small shear:** $\kappa = 0.001$ $\mathbf{d}^{-1}$**.** Frequency spread σ as a function of effective diffusivity ε in d^{-1} for a lattice of 10×10 plankton populations in each of the 10 possible initial spatial arrangements (under advection) of phytoplankton growth rates $\{a_{i,j}\}$.

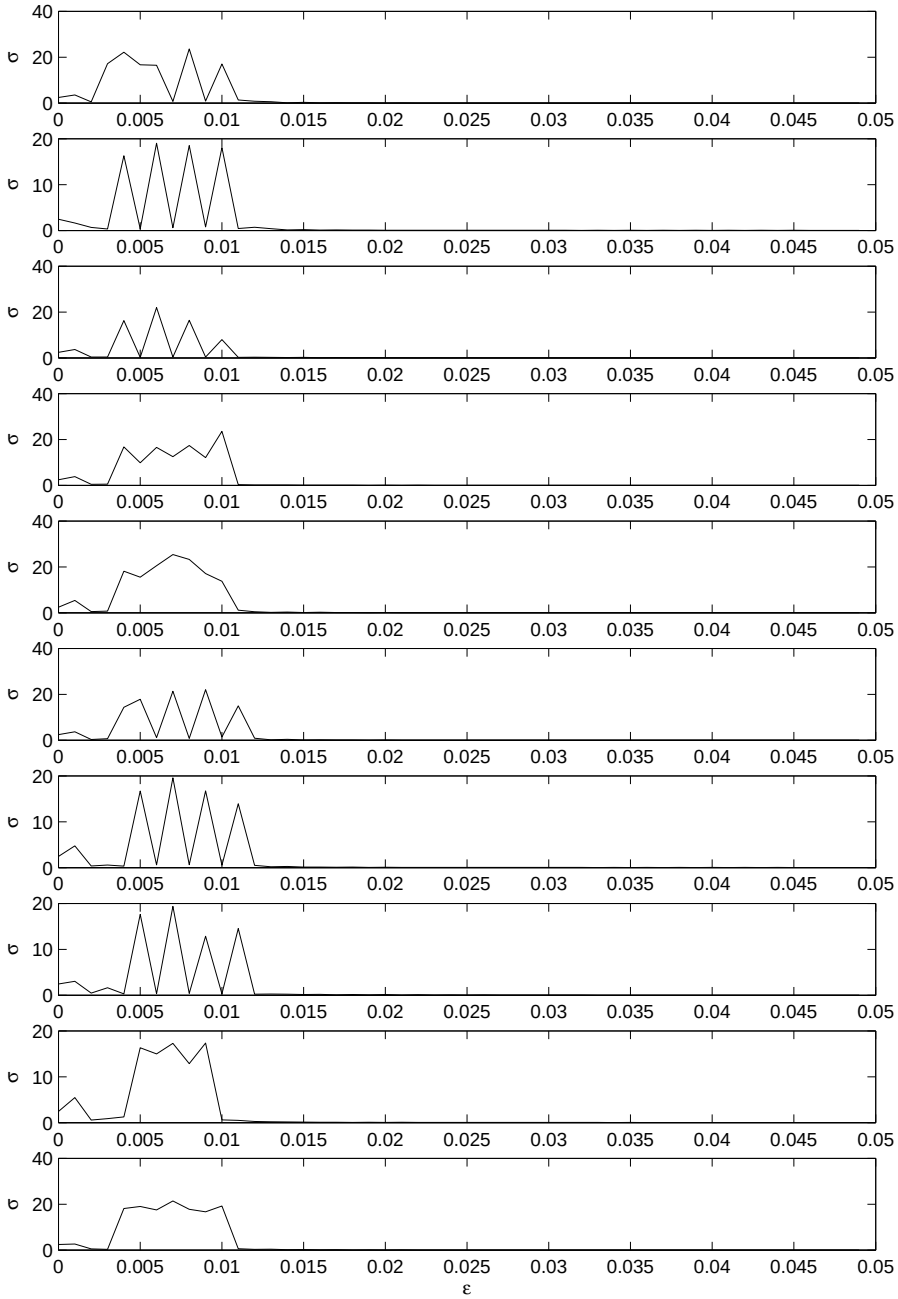

Figure 4.16: **Large shear shear: $\kappa = 0.1$ $\mathbf{d}^{-1}$.** Frequency spread σ as a function of effective diffusivity ε in d^{-1} for a lattice of 10×10 plankton populations in each of the 10 possible initial spatial arrangements (under advection) of phytoplankton growth rates $\{a_{i,j}\}$.

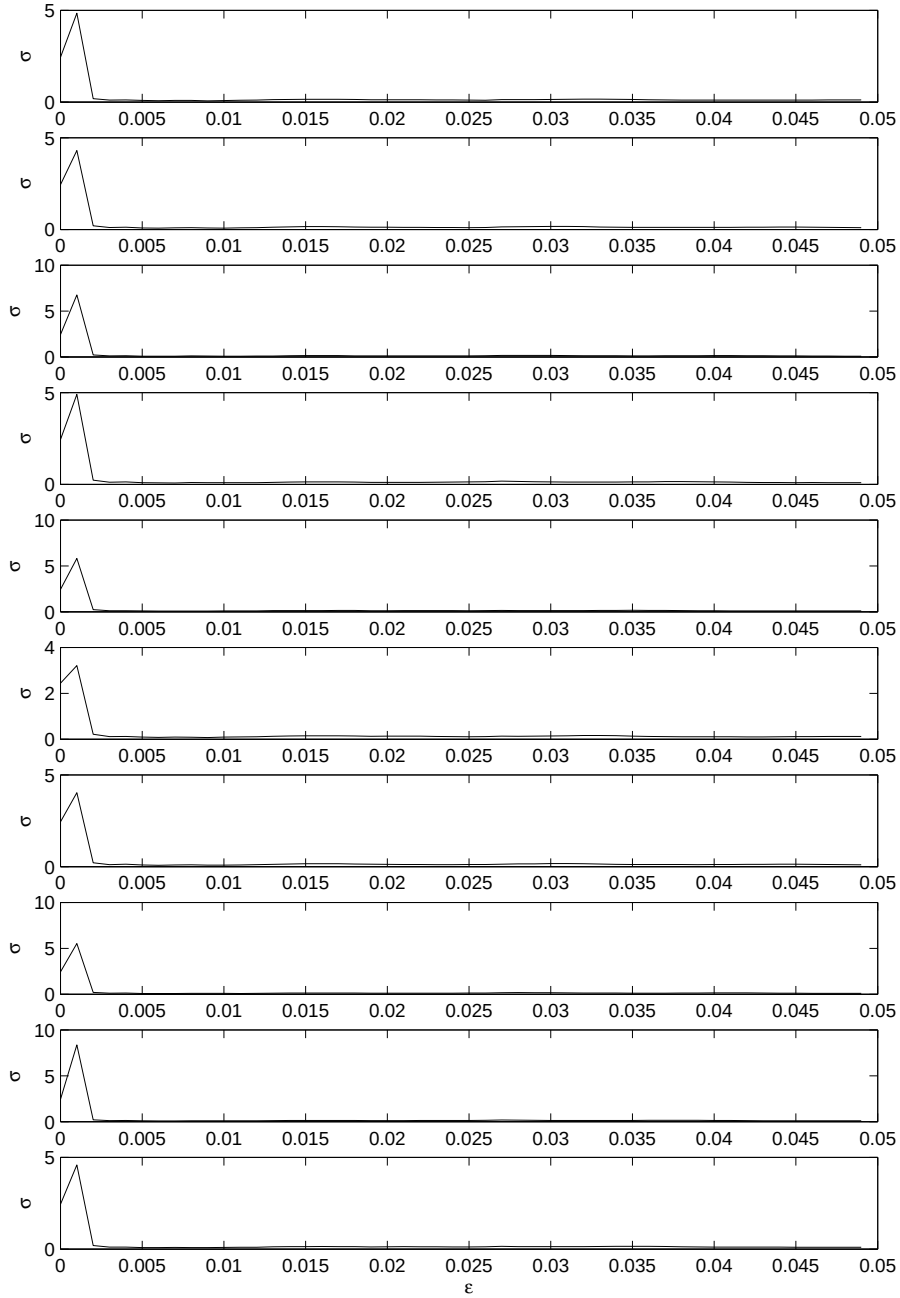

Figure 4.17: **Comparison between rates of shear.** Frequency spread σ as a function of effective diffusivity ε in d^{-1} for a lattice of 10×10 plankton populations for all of the 10 possible initial spatial arrangements (under advection) of phytoplankton growth rates $\{a_{i,j}\}$ for $\kappa = 0.0$ d^{-1} (*top)*, $\kappa = 0.001$ d^{-1} (*middle*) and $\kappa = 0.1$ d^{-1} (*bottom*).

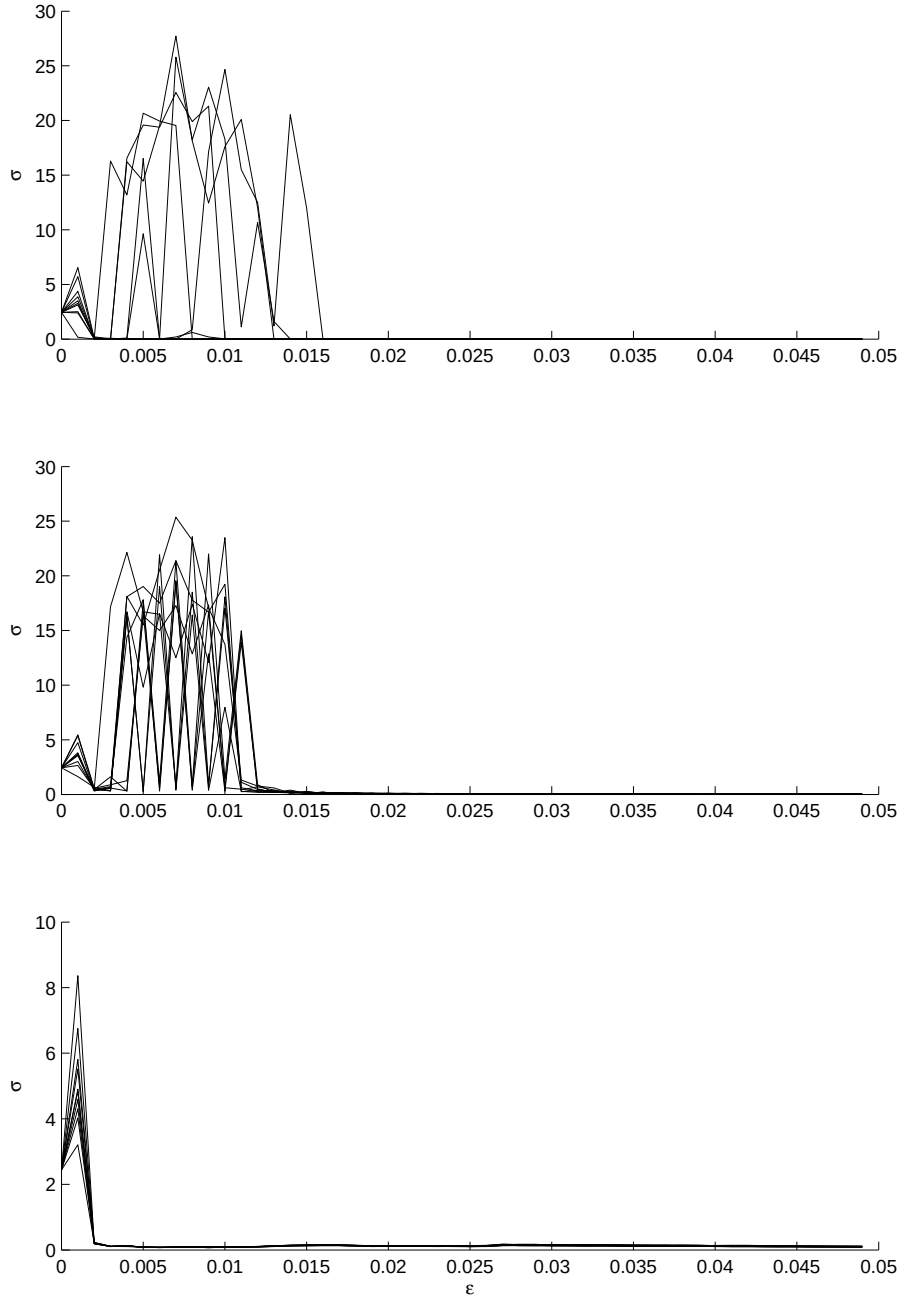

Chapter 5

Conclusions

The overall aim of the study has been to explore the factors determining the ability of a modelled distribution of plankton to exhibit synchronised dynamics, and the kind of emergent spatial structure resulting from such synchronisation. The study has used a metapopulation dynamics approach to modelling a distribution of oceanic plankton; a region of ocean has been taken to comprise a number of plankton populations, interacting through the stirring and mixing action of the flow. The methods of synchronisation theory have been applied to various configurations of this framework to gain insight into how spatial structure emerges in biophysical simulations of the surface ocean. Throughout the study, we have progressively increased the complexity and realism of the simulations, in order to isolate the effects of each factor considered.

Chapter 2 took the simplest possible case - an interacting ensemble of identically-represented plankton populations. The populations were coupled by a nearest-neighbour flux (representing stirring and mixing at scales smaller than the grid-cell) of varying strength ε. Our primary concern was to determine the influence of the specific biological representation in each grid-cell and the number of populations on the strength of coupling ε_c required for persistent synchronisation to occur. We did this by calculating the rate of expansion of perturbations away from synchrony for a number of simulations using different plankton models and varying the number of populations and the coupling strength.

It was found that two kinds of steady-state system-level dynamics are possible

as ε is varied: dynamics alter from fully asynchronous (spatially patchy) for $\varepsilon < \varepsilon_c$ to fully synchronised (spatially homogeneous) for $\varepsilon > \varepsilon_c$. It was found that ε_c can be predicted from the number of grid-cells and from knowledge of the dynamical properties of an isolated individual population, as characterised by the largest Lyapunov exponent of the isolated plankton population model. ε_c increased with the number of populations and also with the largest Lyapunov exponent of the plankton population model.

Hence, the emergent spatial dynamics of the simulation were shown to depend on the biological representation at grid-cell level, the biological model parameters (which together determine the largest Lyapunov exponent of the individual population) and the number of grid-cells comprising the ensemble. Consequently, it is possible for system-level spatial dynamics of biological-physical models to change discontinuously as one of these model parameters is altered.

We have therefore shown the sensitivity of emergent spatial dynamics to the details of the biological representation at grid-cell level in the case of identical oscillators. In reality, spatial variation is likely to occur in biological and physical properties such as mixed-layer depth, temperature and species composition of the modelled area of ocean. Therefore, in Chapter 3 we improved the realism of the simulation by incorporating spatial variation in the biological dynamics. The same underlying plankton ecosystem model was used for the representation of each population but now with spatial variation in a phytoplankton growth parameter. This spatial variation in model parameter values leads to a spread in the natural frequencies of oscillation of the populations.

We used this set-up to explore the ability of a 2D lattice of populations to exhibit sychronised dynamics as a function of the strength of mixing between populations and the number of populations (and hence spatial resolution) of the simulation. We also investigated the kind of resulting spatial struture. We related the strength of mixing ε to the grid-cell length-scale according to the empirical Okubo 1971 relationship between length-scale and diffusivity.

For a lattice of a fixed number of these non-identical populations, it was found that increasing the strength of mixing from zero (uncoupled populations) leads to

some surprising and unintuitive results. Instead of gradually drawing the whole ensemble into synchrony, a range of coupling strength was found for which the spread in population frequencies increased ten-fold in comparison with the natural spread in frequencies. Within this regime, clustering of populations into persistent pockets of local synchrony was found to occur. These clusters are not fixed in space or time, but constantly shift and merge whilst maintaining their statistical properties. With large enough mixing, the ensemble was eventually found to fully frequency-lock, but, within the obervationally-constrained range of coupling considered, never fully phase-lock.

Next a fixed size of spatial domain was divided into a variable number of grid-cells n, so that the spatial resolution and corresponding length-scale dependent mixing strength of the simulation varied accordingly. The same states of asynchrony, clustering and frequency-locking were found to emerge, dependent once more upon the number of grid-cells. With increasing number of populations, and therefore spatial resolution, the ensemble dynamics were found to first enter the region of increased frequency disorder and local clustering of populations. With increasing number of grid-cells, the ensemble dynamics were frequency-locked. Again, full phase-locking was not achieved for any value of n.

A succession of transitions between the clustering and frequency-locking states for intermediate values of n revealed a startling dependency of the ensemble dynamics on the particular values and spatial arrangement of population natural frequencies, even for a fixed range of variability. Further investigations showed that the critical coupling strength for frequency-locking of the lattice varied widely with the particular selection of parameter mismatch values, even if drawn from the same distribution, and also that the required coupling was not predictable from the spread in natural frequencies resulting from the parameter mismatch.

Up to this point, we had only considered the effects of stirring and mixing at sub-grid-cell scale. In reality, the flow is likely to affect the distribution at all scales, so in Chapter 4, the robustness of the previous results to the influence of an advecting flow was investigated by applying a linear shear to the simulation. The rate of shear was varied within an oceanographically realistic range and the mixing strength ε was

again varied to determine the coupling required for stably synchronised dynamics.

The unintuitive coupling-induced frequency disorder for intermediate values of ε was again found to occur, with system level dynamics being asynchronous, cluster synchronised or frequency-locked as a function of the level of mixing. The well-defined clusters observed for simulations without advection persisted under the influence of shear but were found to be increasingly narrowed and stretched in the direction of advection with increasing rate of shear. As described above, these clusters are not stationary in time or space, but shift and evolve under the influence of the biology and mixing, retaining their statistical characteristics.

The rearrangement of populations caused by the advection of rows of populations leads to a time-dependent arrangement of population natural frequencies. As suggested by the results on variability from Chapter 3, this leads to a time-dependency of the level of mixing required to frequency-lock the ensemble. The consequences of this were found to depend on the rate of shear. For small shear with respect to the time-scales of the evolution of the biology and the rate of mixing, the result was a succession of transitions between clustering and frequency locking within the intermediate range of mixing. For large shear with respect to the time-scales of the other governing processes, the advection enhanced the mixing between populations by increasing the network of influence of each population and effectively altering the coupling geometry of the lattice, thus enabling the ensemble to synchronise at much lower values of ε.

To summarise, we have shown that the manifestation of synchronisation effects in a simulated distribution of plankton depends upon the following.

- **The strength of coupling between populations.** In general, we have seen that there exists a critical level of coupling above which the system is stably synchronised. That many of the simulations were only able to frequency-lock and not fully phase-lock within the range of coupling considered shows that this level of synchrony may not be achievable within an oceanographically realistic range, however. Additionally, we have shown that the effect of increased coupling is by no means monotonic; intermediate strengths of coupling can *increase* the mismatch between populations.

In this study, the coupling has been taken to represent stirring and mixing between populations at spatial scales smaller than the grid-cell, but further work could explore additional or alternative coupling mechanisms such as migration between populations, for example by a more motile zooplankton species or a nomadic higher predator, taking inspiration from studies of terrestrial population dynamics. The results from the present study would be directly applicable to and would provide a firm basis for such further work.

- **The number of populations or grid-cells, or, equivalently, the spatial resolution of a modelled domain of fixed area.** A stronger degree of coupling is required to synchronise a larger ensemble of populations. Equivalently, increasing the spatial resolution of a model increases the strength of coupling at which synchronised dynamics will occur. We have shown this for both a chain and lattice of populations so it is a reasonable assumption that the results will generalise to any shape of domain being modelled, although, in a further departure from terrestrial metapopulation studies, it would be interesting to verify the occurrence of synchronisation phenomena in three-dimensional, depth-resolved simulations.

- **The grid-cell biological representation.** We have shown clearly that the emergent spatial properties of the simulation depend upon, and are in some cases predictable from, the dynamical properties of the individual plankton populations as determined by the choice of biological model and parameters.

- **Disparities between populations.** The ability to synchronise depends upon whether the interaction between populations can counteract the inherent "difference" between populations, whether provided by the internally generated desynchronising influence of chaotic dynamics or, in the case of oscillatory dynamics, by differences in their natural frequencies. We have shown that, for the case of identically-represented populations, "more chaotic" populations require stronger coupling for stable synchrony. Note, however, that there is some indication that chaos can *aid* synchronisation in an ensemble of non-identical populations (Hillary and Bees, 2004a), a case not directly investigated here.

We have also seen that the critical coupling for synchrony is particularly sensitive to how the spatial variation in frequencies is arranged in the modelled domain. Here, we have considered a fixed value for the range in natural frequencies. Further studies should look at how large an inherent spatial disparity can still be overcome by realistic levels of coupling between populations to lead to homogeneous dynamics; a comparison with the level of natural variation expected in key plankton properties in the ocean would indicate the scale at which such synchronisation effects could be expected in nature.

- **Stirring of populations.** This influences the geometry and strength of coupling between populations. The details of the flow can therefore affect the spatial disorder of populations, leading to a time-dependency in the emergence of synchronised dynamics. Potentially, the network of interaction of each population is increased by the stirring, enhancing the mixing in the system and allowing synchronisation at lower coupling strengths.

  Importantly, synchronisation phenomena such as clustering and frequency-locking have been shown to persist under the disturbing influence of advection, although their manifestation may be altered, e.g. clusters become stretched and narrowed along the direction of flow. A natural extension of this work would be to more closely approximate a time-varying surface ocean flow by examining the emergence of synchronisation in a more complex flow such a field of interacting eddies.

The results of this study have a number of consquences for the coupled biological-physical modelling of plankton dynamics, which we summarise here.

Altering model parameters, such as the strength of coupling or number of grid-cells, can discontinuously alter the spatial properties of a model. For example, increasing the spatial resolution, and therefore number of grid-cells, of a simulation can alter system level dynamics from non-synchronised to synchronised, or from clustering of populations to full synchrony. The presence of this discontinuity is of concern if such a model is to be used to study length-scales of plankton patchiness since increasing the model resolution could obliterate the patches. Researchers

should therefore check the sensitivity of their results to changes in spatial resolution and the other influences on synchronisation that have been listed above.

This may be particularly important if models are being used to estimate or make predications of biogeochemical properties such as primary production. In Chapter 2, we made some simple calculations of how total primary production differed between synchronised and non-synchronised simulations, but more work should focus on examining this impact if we are to have faith in predictions from coupled biological-physical models.

Modellers should also be aware of the dependence of model results on the specific grid-cell parameterisation of biology. In many cases, plankton ecosystem models may be selected for use in biological-physical models without a clear idea of their mathematical properties. More care should be taken since this has been shown here to determine model behaviour. From a more positive point of view, this study has confirmed the possibility of predicting system-level behaviour from the grid-cell biology and the model physics. With further work, it is possible that an understanding of the mathematical properties of the biological model dynamics, including the amount of spatial variation, taken together with the physical flow, perhaps characterised in terms of its effect on the network of interaction between populations and the strength of mixing in time and space, could be used to predict system level spatial dynamics. This knowledge of model behaviour built up from the model components may aid in understanding the behaviour of complex biological-physical models.

We showed in this study that model results can display an alarming sensitivity to apparently small changes in model parameters. This was illustrated by the large range of possible critical coupling strengths for frequency locking of a lattice of non-identical populations, even when the biological model, the number of populations, the spread in parameter mismatch, the initial conditions and the boundary conditions are all fixed and the simulations differ only in the particular selection of parameter values from a fixed distribution, or even just in the spatial arrangement of the *same set* of parameter values. These results should urge modellers to perform careful sensitivity analysis of results to the choice of parameterisation of spatial variariability in models. However, later results showed the mitigation of some of this

variability by strong stirring with respect to the time-scales of mixing and evolution of the biology.

That we have shown synchronisation effects to persist under a range of increasingly realistic simulations provides confidence that synchronisation theory can explain some of the patchiness structure seen in plankton in the ocean. One possible line of future work would be to increase the realism of the simulation by studying the synchronisation of populations under the influence of a more realistic fully turbulent flow. Alternatively, for a particular region, a map of satellite altimeter-derived horizontal current velocities could be used to characterise the region in terms of the coupling strengths between populations at different points in space and time. With a suitable representation of the biological dynamics of the region, making comparisons with satellite ocean colour chlorophyll data, such a set up could be used to further explore how emergent structure in real plankton populations can be characterised in terms of synchronisation phenomena.

Most importantly, this study has shown that persistent spatial heterogeneity, characterised by local clustering of populations and an increase in frequency disorder, results from what intuitively should be an homogenising influence; mixing of the plankton populations actually increases the difference between populations and creates statistically stable patchiness. Further work should look further at how the length-scales of these clusters relates to scales of patchiness seen in empirical data. These unexpected synchronisation effects have provided one possible answer as to how tiny planktonic organisms are able to manifest large coherent strutures under the homogenising influence of mixing and stirring by the flow.

Bibliography

E. Abraham. The generation of plankton patchiness by turbulent stirring. *Nature*, 391:577–580, 1998.

E. Abraham, C. S. Law, P. W. Boyd, S. J. Lavendar, M. T. Maldonado, and A. R. Bowie. Importance of stirring in the development of an iron-fertilsed phytoplankton bloom. *Nature*, 407:727–730, 2000.

A. E. Alpine and J. E. Cloern. Phytoplankton growth rates in a light limited environment, San Francisco Bay. *Marine Ecology Progress Series*, 44:167–173, 1988.

R. Bainbridge. The size, shape and density of marine phytoplankton concentrations. *Biological Review*, 32:91–115, 1956.

B. Barbay, G. Giacomelli, and F. Marin. Stochastic resonance in vertical cavity surface emitting lasers. *Physical Review E*, 61(1):157–166, 2000.

J. W. Baretta, W. Ebenhö, and P. Ruardij. The european regional seas ecosystem model, a complex marine ecosystem model. *Netherlands Journal of Sea Research*, 33:233–246, 1995.

R. S. K. Barnes and R. N. Hughes. *An Introduction to Marine Ecology*. Blackwell Science, 1982.

M. A. Bees, I. Mezic, and J. McGlade. Planktonic interactions and chaotic advection in Langmuir circulation. *IMACS Mathematics and Computing in Simulation*, 44 (6):527–544, 1998.

I. Belykh, V. Belykh, K. Nevidin, and M. Hasler. Persistent clusters in lattices of coupled nonidentical chaotic systems. *Chaos*, 13(1):165–178, 2003.

T. G. Benton, C. T. Lapsley, and A. P. Beckerman. Population synchrony and environmental variation: An experimental demonstration. *Ecology Letters*, 4: 236–243, 2001.

B. Blasius and E. Montbrió. Anomalous phase synchronisation in populations of nonidentical oscillators. *Physical Review E*, 67, 2003.

B. Blasius and L. Stone. Nonlinearity and the Moran effect. *Nature*, 406:846–847, 2000.

S. Boccaletti, editor. *Complex Synchronization Phenomena in Ecological Systems*, volume 6 of *Experimental Chaos*, 2002. American Institute of Physics.

H. Caswell and M. G. Neubert. Chaos and closure terms in plankton food chain models. *Journal of Plankton Research*, 20(9):1837–1845, 1998.

S. Connor. An ocean in bloom: Storms breathe life into the Atlantic. *Independent*, June 2004.

R. A. Duce and N. W. Tindale. Atmospheric transport of iron and its deposition in the ocean. *Limnology and Oceanography*, 36(8):1715–1726, 1991.

A. M. Edwards. Adding detritus to a nutrient-phytoplankton-zooplankton model: A dynamical systems approach. *Journal of Plankton Research*, 23(4):389–413, 2001.

A. M. Edwards and J. Brindley. Oscillatory behaviour in a three-component plankton population model. *Dynamics and Stability of Systems*, 11(4):347–370, 1996.

A. M. Edwards and J. Brindley. Zooplankton mortality and the dynamical behaviour of plankton population models. *Bulletin of Mathematical Biology*, 61:303–339, 1999.

C. Elton and M. Nicholson. The ten-year cycle in numbers of the lynx in Canada. *Journal of Animal Ecology*, 11(2):215–244, November 1942.

R. W. Eppley. Temperature and phytoplankton growth in the sea. *Fisheries Bulletin*, 70:1063–1085, 1972.

E. M. Fairen. *Synchronization in Ensembles of Nonisochronous Oscillators*. PhD thesis, Das Institut für Physik der Universität Potsdam, 2004.

M. J. R. Fasham, editor. *Ocean Biogeochemistry*. The IGBP Series: Global Change. Springer, 2003.

M. J. R. Fasham, H. W. Ducklow, and S. M. McKelvie. A nitrogen-based model of plankton dynamics in the oceanic mixed layer. *Journal of Marine Research*, 48: 591–639, 1990.

A. Fielding, N. Crisp, J. T. Allen, M. C. Hartman, B. Rabe, and H. S. J. Roe. Mesoscale subduction at the Almeria-Oran front 2: Biophysical interaction. *Journal of Marine Systems*, 30:287–304, 2001.

C. Folt and C Burns. Biological drivers of zooplankton patchiness. *TREE*, 14: 300–305, 1999.

H. Fujisaka and T. Yamada. Stability theory of synchronized motion in coupled-oscillator systems. *Progress in Theoretical Physics*, 69:32–48, 1983.

G. F. Fussman, S. P. Ellner, K. W. Shertzer, and N. G. Hairston Jr. Crossing the Hopf bifurcation in a live predator-prey system. *Science*, 290(5495):1358–1360, 2000.

V. C. Garçon, A. O. Oschlies, S. C. Doney, D. McGillicuddy, and J. Waniek. The role of mesoscale variability on plankton dynamics in the North Atlantic. *Deep Sea Research II*, 48:2199–2226, 2001.

B. T. Grenfall, K. Wilson, B. F. Finkenstädt, T. N. Coulson, S. Murray, S. D. Albon, J. M. Pemberton, T. H. Clutton-Brock, and M. J. Crawley. Noise and determinism in synchronised sheep dynamics. *Nature*, 394:673–677, 1998.

T. Gross, W. Ebenhoh, and U. Feudel. Long food chains are in general chaotic. *OIKOS*, 109(1):135–144, 2006.

E. J. Guirey, M. A. Bees, A. P. Martin, M. A. Srokosz, and M. J. R. Fasham. Emergent features due to grid-cell biology: Synchronisation in biophysical models. *Bulletin of Mathematical Biology*, 69(4):1401–1422, 2007.

I. Hanski. Metapopulation dynamics. *Nature*, 396:41–49, 1998.

A. Hastings and T. Powell. Chaos in a three-species food chain. *Ecology*, 72:896–903, 1991.

D. T. Haydon, N. C. Stenseth, M. S. Boyce, and P. E. Greenwood. Phase coupling and synchrony in the spatiotemporal dynamics of muskrat and mink populations across Canada. *Ecology*, 98(23):13149–13154, 2001.

R. M. Hillary and M. A. Bees. Plankton lattices and the role of chaos in plankton patchiness. *Physical Review E*, 69(031913), 2004a.

R. M. Hillary and M. A. Bees. Synchrony and chaos in patchy ecosystems. *Bulletin of Mathematical Biology*, 66:1909–1931, 2004b.

M. Holyoak and S. P. Lawler. Persistence of an extinction-prone predator prey interaction through metapopulation dynamics. *Ecology*, 77(6):1867–1879, 1996.

A. Huppert, R. Olinky, and L. Stone. Bottom-up excitable models of phytoplankton blooms. *Bulletin of Mathematical Biology*, 66:865–878, 2004.

A. E. S. Kemp, R. B. Pearce, I. Grigorov, J. Rance, C. B. Lange, P. Quilty, and I. Salter. Production of giant marine diatoms and their export at oceanic frontal zones: Implications for Si and C flux from stratified oceans. *Global Biogeochemical Cycles*, 20(4), 2006.

H. Kierstead and L. B. Slobodkin. The size of water masses containing plankton blooms. *Journal of Marine Science*, 12:141–147, 1953.

C. M. Lalli and T. R. Parsons. *Biological Oceanography: An Introduction*. The Open University, 1997.

M. Levy and P. Klein. Does the low frequency variability of mesoscale dynamics explain a part of the phytoplankton and zooplankton spectral variability? *Proceedings of the Royal Society of London A*, 460:1673–1687, 2004.

S. Lovejoy, W. J. S. Currie, Y. Tessier, M. R. Claereboudt, E. Bourget, J. C. Roff, and D. Schertzer. Universal multifractals and ocean patchiness: Phytoplankton, physical fields and coastal heterogeneity. *Journal of Plankton Research*, 23(2): 117–141, 2001.

H. Malchow, B. Radtke, M. Kallache, A. B. Medvinsky, D. A. Tickhonov, and S. V. Petrovskii. Spatio-temporal pattern formation in coupled models of plankton dynamics and fish school motion. *Nonlinear Analysis: Real World Applications*, 1:53–67, 2000.

A. P. Martin. On filament width in oceanic plankton distributions. *Journal of Plankton Research*, 22(3):597–602, 2000.

A. P. Martin. Phytoplankton patchiness: the role of lateral stirring and mixing. *Progress in Oceanography*, 57:125–174, 2003.

A. P. Martin and K. J. Richards. Patchy productivity in the open ocean. *Global Biogeochemical Cycles*, 16(2):1025–1034, 2002.

P. McLeod, A. P. Martin, and K. J. Richards. Minimum length scale for growth-limited oceanic plankton distributions. *Ecological Modelling*, 158:111–120, 2002.

P. A. P. Moran. The statistical analysis of the Canadian lynx cycle. *Australian Journal of Zoology*, 1:291–298, 1953.

J. D. Murray. *Mathematical Biology*. Springer, 1989.

Z. Néda, E. Ravasz, Y. Brechet, T. Vicsek, and A. L. Barabśsi. Tumultuous applause can transform itself into waves of sychronized clapping. *Nature*, 403:157–166, 849-850 2000.

J. Neff and T. L. Carroll. Circuits that get chaos in sync. *Scientific American*, 296: 101–103, 1993.

Z. Neufeld, P. Haynes, and T. Tel. Chaotic mixing induced transitions in reaction-diffusion systems. *Chaos*, 12(2):426–438, 2002.

Z. Neufeld, I. Z. Kiss, C. Zhou, and J. Kurths. Synchronisation and oscillator death in oscillatory media with stirring. *Physical Review Letters*, 91(8), 2003.

Z. Neufeld and C. Lopez. Smooth-filamental transition of active tracer fields stirred by chaotic advection. *Physical Review Letters*, 82(12):2606–2609, 1999.

A. Okubo. Oceanic diffusion diagrams. *Deep-Sea Research*, 18:789–802, 1971.

G. V. Osipov and M. M. Sushchik. The effect of natural frequency distribution on cluster synchronization in oscillator arrays. *IEEE Transactions on Circuits an Systems - I: Fundamental Theory and Applications*, 44(10):1006–1010, 1997.

M. Pascual, M. Roy, F. Guichard, and G. Flierl. Cluster size distributions: Signitures of self-organization in spatial ecologies. *Philosophical Transactions of the Royal Society of London B*, 357:657–666, 2002.

S. V. Petrovskii. On the plankton front waves generated by marine turbulence. *Journal of Marine Science*, 21:179–188, 1999.

A. Pikovsky, R. Michael, and J. Kurths. *Synchronisation: A Universal Concept in Nonlinear Sciences*. Cambridge, 2001.

T. Platt and K. L. Denman. Spectral analysis in ecology. *Annual Review of Ecology and Systematics*, 6:198–210, 1975.

E. E. Popova. Non-universal sensitivity of a robust ecosystem model of the ocean upper mixed layer. *Ocean Modelling*, 109:2–5, October 1995.

E. E. Popova, C. J. Lozano, M. A. Srokosz, M. J. R. Fasham, P. J. Haley, and A. R. Robinson. Coupled 3D physical and biological modelling of the mesoscale variability observed in North-East Atlantic in spring 1997: Biological processes. *Deep-Sea Research I*, 49:1741–1768, 2002.

W. H. Press, S. A. Teukolsky, W. T. Vetterling, and B. P. Flannery. *Numerical Recipes in C: The Art of Scientific Computing*. Cambridge University Press, 1992.

E. Ranta, V. Kaitala, J. Lindström, and H. Lindén. Synchrony in population dynamics. *Proceedings of the Royal Society of London B*, 262:113–118, 1995.

R. Reigada, R. M. Hillary, M. A. Bees, J. M. Sancho, and F. Sagués. Plankton blooms induced by turbulent flows. *The Royal Society*, 270:875–880, 1998.

J. Ripa. Analysing the Moran effect and dispersal: Their significance and interaction in synchronous population dynamics. *OIKOS*, 90:175–187, 2000.

A. R. Robinson. On the theory of advective effects on biological dynamics. *Proceeding of the Royal Society of London A*, 453:2295–2324, 1997.

M. G. Rosenblum, A. S. Pikovsky, and J. Kurths. From phase to lag synchronization in coupled chaotic oscillators. *Physical Review Letters*, 78:4193–4196, 1997.

V. A. Ryabchenko, M. J. R. Fasham, B. A. Kagan, and E. E. Popova. What causes short-term oscillations in ecosystem models of the ocean mixed layer? *Journal of Marine Systems*, 13:33–50, 1997.

J. L. Sarmiento and N. Gruber, editors. *Ocean Biogeochemical Dynamics*. Princeton University Press, 2006.

T. N. Sherratt, X. Lambin, S. J. Petty, J. L. Mackinnon, C. F. Coles, and C. J. Thomas. Use of coupled oscillator models to understand synchrony and travelling waves in populations of the field vole *Microtus agrestis* in northern England. *Journal of Applied Ecology*, 37:148–158, 2000.

J. G. Skellam. Random dispersal in theoretical populations. *Biometrika*, 38:196–218, 1951.

L. B. Slobodkin. Akira Okubo and the theory of blooms. *Oceanography*, 12(1):9–14, 1999.

C. L. Smith, K. J. Richards, and M. J. R. Fasham. The impact of mesocale eddies on plankton dynamics in the upper ocean. *Deep-Sea Research I*, 43:1807–1832, 1996.

M. A. Srokosz, A. P. Martin, and M. J. R. Fasham. On the role of biological dynamics in plankton patchiness at the mesoscale: An example from the eastern North Atlantic ocean. *Journal of Marine Research*, 61:517–537, 2003.

J. H. Steele. Spatial heterogeneity and population stability. *Nature*, 248:83, 1974.

J. H. Steele, editor. *Spatial Pattern in Plankton Communities*. Plenum Press, 1978.

J. H. Steele and E. W. Henderson. A simple plankton model. *The American Naturalist*, 344:734–741, 1981.

J. H. Steele and E. W. Henderson. A simple model for plankton patchiness. *Journal of Plankton Research*, 14(10):1397–1403, 1992.

S. Strogatz. *Nonlinear Dynamics and Chaos: With Applications to Physics, Biology, Chemistry and Engineering*. Perseus Books, 1994.

S. Strogatz. *Sync: Rhythms of Nature, Rhythms of Ourselves*. Penguin: Allen Lane, 2003.

S. H. Strogatz and I. Stewart. Coupled oscillators and biological synchronisation. *Scientific American*, 269:68–75, 1993.

M. A. Sundermeyer and J. F. Price. Lateral mixing and the North Atlantic tracer release experiment: Observations and numerical simulations of lagrangian particles and a passive tracer. *Journal of Geophysical Research*, 103:21481–21497, 1998.

S. Taherion and Y. C. Lai. Observability of lag synchronization of coupling chaotic oscillators. *Physical Review E*, 59(6):6247–6250, 1999.

I. J. Totterdell. An annotated bibliography of marine biological models. In G. T. Evans and M. J. R. Fasham, editors, *Towards a Model of Ocean Biogeochemical Processes*, volume 10. NATO, 1993.

A. M. Turing. The chemical basis of morphogenesis. *Philosophical Transactions of the Royal Society of London B*, 237:37–72, 1952.

R. C. Ydenberg. Nomadic predators and geographical synchrony in microtine population cycles. *OIKOS*, 50(2):270–272, 1987.

J. Ylikarjula, S. Alaja, J. Laaksos, and D. Tesar. Effects of patch number and dispersal patterns on population dynamics and synchrony. *Journal of Theoretical Biology*, 207:377–387, 2000.

W. R. Young, A. J. Roberts, and G. Stuhne. Reproductive pair correlations and the clustering of organisms. *Nature*, 412:328–331, 2001.